Failure Analysis of Brazed Joints Using the CZM Approach

by

Morvarid Karimi Ghovanlou

A thesis
presented to the University of Waterloo
in fulfillment of the
thesis requirement for the degree of
Doctor of Philosophy
in
Mechanical Engineering

Waterloo, Ontario, Canada, 2011

Author's Declaration

I hereby declare that I am the sole author of this thesis. This is a true copy of the thesis, including any required final revisions, as accepted by my examiners.

I understand that my thesis may be made electronically available to the public.

Morvarid Karimi Ghovanlou

Abstract

Brazing, as a type of joining process, is widely used in manufacturing industries to join individual components of a structure. Structural reliability of a brazed assembly is strongly dependent on the joint mechanical properties. In the present work, mechanical reliability of low carbon steel brazed joints with copper filler metal is investigated and a methodology for failure analysis of brazed joints using the cohesive zone model (CZM) is presented.

Mechanical reliability of the brazed joints is characterized by strength and toughness. Uniaxial and biaxial strengths of the joints are evaluated experimentally and estimated by finite element method using the ABAQUS software. Microstructural analysis of the joint fracture surfaces reveals different failure mechanisms of dimple rupture and dendritic failure. Resistance of the brazed joints against crack propagation, evaluated by the single-parameter fracture toughness criterion, shows dependency on the specimen geometry and loading configuration.

Fracture of the brazed joints and the subsequent ductile tearing process are investigated using a two-parameter CZM. The characterizing model parameters of the cohesive strength and cohesive energy are identified by a four-point bend fracture test accompanied with corresponding FE simulation. Using the characterized CZM, the joint fracture behavior under tensile loading is well estimated. Predictability of the developed cohesive zone FE model for fracture analysis of brazed joints independent of geometry and loading configuration is validated.

The developed cohesive zone FE model is extended to fatigue crack growth analysis in brazed joints. A cyclic damage evolution law is implemented into the cohesive zone constitutive model to irreversibly account for the joint stiffness degradation over the number of cycles. Fatigue failure behavior of the brazed joints is characterized by performing fully reversed strain controlled cyclic tests. The damage

law parameters are calibrated based on the analytical solutions and the experimental fatigue crack growth data. The characterized irreversible CZM shows applicability to fatigue crack growth life prediction of brazed joints.

Acknowledgments

I would like to express my sincere gratitude to my supervisors, Professor Hamid Jahed and Professor Amir Khajepour for their guidance, valuable support, and precious discussions during the course of this research.

Financial support from the Natural Sciences and Engineering Research Council of Canada (NSERC) is gratefully acknowledged.

I would also like to highly appreciate Professor Daniel Kujawski for serving as my external examiner.

I also would like to gratitude my Ph.D. committee members, Professor Gregory Glinka, Professor Steve Corbin, and Professor Jeffrey S. West, for their suggestions and advices. I am also thankful to Professor Mustafa Yavuz for attending my Ph.D. oral defense as a committee member's delegate.

I would also like to express my gratitude to Professor Timothy Topper and Professor Katerina D. Papoulia for their precious advices. Also, I appreciate Dr. Dennis Turriff, Dr. Sooky Winkler and Dan Cluff for their valuable assistance and helpful discussions we had.

The knowledge and efforts of my colleagues in our group was a valuable source of inspiration and success. In particular, I highly appreciate Dr. Mohammad

Noban and Dr. Amin Eshraghi for their precious assistance and advices. Moreover, Jaho Seo, Hossein Ahari, Jafar Al Bin Mousa, Behzad Behravesh, and Arash Tajik are thanked for the great discussions and collaborations we had.

I would also like to thank Dr. Yuquan Ding, Andrew Barber, Norval Wilhelm, Steve Hitchman, Martha Morales, John Potzold, and John Boldt, the UW staffs, for their valuable assistance and technical supports.

Especially, I would like to express my profound appreciations to my family. I am always indebted to my beloved parents, Amir Saeed and Mahnaz, for their unconditional love, endless support, and inspiration throughout all my years of education. I also would like to extend my gratitude wholeheartedly to my grandmother for her devotions and concerns throughout my life. Moreover, I am thankful to my sister, Marjan, and her family for their affections and encouragements. Last but not least, to my dear husband Amin, thank you for your true love, great support and patience during my studies, without which I could not make it through.

To my beloved family

Table of Contents

List of Figures

List of Tables

Nomenclature

a	Crack length
A	Damage evolution law parameter
A	Crack area
A_{Vpl}	Plastic component of the area under load-CMOD curve
b	Ligament length
B	Fracture specimen thickness
d_i	Inner diameter
d_o	Outer diameter
dt	Time increment
D_c	Cyclic damage variable
$\dot{D}_c$	Incremental cyclic damage evolution
D_N	Damage variable at cycle N
E	Young's modulus
F	Work of external load
G_o	Elastic energy at damage onset
G_c	Critical energy release rate
J	Energy release rate
J_c	Critical energy release rate

J_{el}	Elastic component of the energy release rate
J_C^{el}	Elastic component of the critical energy release rate
J_{pl}	Plastic component of the energy release rate
J_C^{pl}	Plastic component of the critical energy release rate
k	Cohesive element stiffness
k_0	Cohesive element initial stiffness
K_c	Fracture toughness
K_I	Mode I stress intensity factor
m	Damage evolution law parameter
n	Damage evolution law parameter
N	Regularizing parameter
P	Load
P_c	Critical load
P_{max}	Maximum load
r	State variable
S	Total cross sectional area
S_D	Damaged cross sectional area
S_{inner}	Inner loading span
S_{outer}	Outer loading span
S_s	Shear stress at failure

S_{su}	Single mode shear strength
S_t	Tensile stress at failure
S_{tu}	Single mode tensile strength
t	Brazed joint clearance
T	Applied torque
T	Traction
T_0	CZM fatigue endurance limit
U	Separation
$\dot{U}$	Rate of change in separation
w	Displacement
W	Fracture specimen width
Y	Strain energy density release rate (Damage driving force)
Y^*	Critical damage driving force
Y_f	Characteristic value of Y
α	State variable
δ_0	Separation at onset of damage initiation
δ_C	Separation at failure
Δ	Displacement
Δ_{el}	Elastic component of displacement
Δ_{pl}	Plastic component of displacement

ε	Total strain
ε^e	Elastic strain
ε^p	Equivalent plastic strain
γ_{CMOD}	geometry factor
γ_s	Material surface energy
γ_p	Plastic work per unit area of crack
Γ	Cohesive energy
η	Regularizing parameter
η_{CMOD}	geometry factor
Π	Potential energy
θ	Temperature
ρ	Mass density
σ	Axial stress
σ_∞	Far field axial stress
$\tilde{\sigma}$	Effective stress
σ_H	Hydrostatic part of the stress
$\sigma_{max,0}$	Cohesive strength
σ_{Mises}	Equivalent Mises stress
τ_{ave}	Average shear stress
Ψ	Helmholtz specific free energy function

Chapter 1
Introduction

Brazing, as a type of joining process, is widely used in joining industry to manufacture assembled products from two or more individual components. In the brazing process a filler metal with a melting point of above 450 °C and below the solidus temperature of the base metal is melted and diffused into the faying surfaces of the individual parts to join them following solidification [1].

Structural reliability of a brazed assembly strongly depends on the joint mechanical properties. In this study, mechanical reliability of low carbon steel brazed joints with copper filler metal is characterized by strength, fracture

toughness, and fatigue properties. Moreover, a cohesive zone model (CZM) is adapted for prediction of the joint fracture and simulation of ductile tearing process under quasi-static loading. A cyclic damage evolution law is further coupled to the CZM and calibrated to the results of the fatigue tests to predict crack growth life under cyclic loading.

1.1 Motivation

Injection molding is a manufacturing process used to produce parts by injecting pressurized molten polymer into molds or dies. Because this process enables fabricating parts of complex shapes with high precision and repeatability, it has been widely used in manufacturing related industries. In recent years, in order to achieve high efficiency in injection molding, a revolutionary mold design, i.e. laminated die, has been investigated. Producing an injection mold with laminated tooling technology enables engineers to replace conventional cooling channels with conformal ones. Using the conformal cooling channels the rate of heat dissipation noticeably increases and the temperature uniformly distributes through the whole die. Thus, the cycle time decreases and thermal distortions of the parts are minimized to enhance the productivity and quality [2]. A schematic of the laminated structure is shown in Figure 1-1.

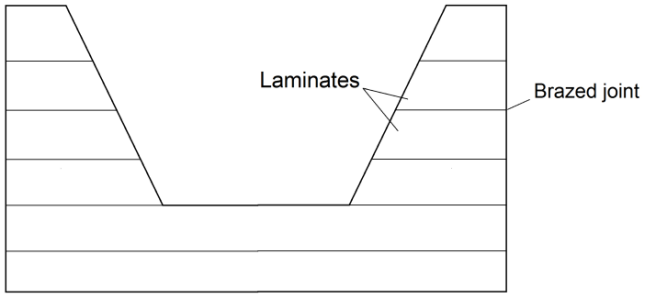

Figure 1-1- Schematic of a laminated structure

One of the feasible and effective methods in joining layers of a laminated injection mold is the brazing process. The critical aspect in designing of a laminated die is consideration of mechanical reliability of the whole structure. Since the brazed joints are the most critical locations for failure, structural reliability of a brazed assembly strongly depends on the joint mechanical properties. Mechanical reliability of brazed joints has been characterized by various criteria such as strength, toughness, and fatigue properties [3]. In the current study, the brazed joints strength and fracture toughness are evaluated experimentally. A two-parameter CZM, as a fracture analysis tool, is characterized to predict the joint fracture strength at the onset of crack initiation and simulate the subsequent ductile tearing process independent of geometry and loading. Furthermore, a damage evolution law in coupled to the cohesive zone constitutive model is calibrated to simulate fatigue crack propagation and predict the corresponding fatigue lives under strain controlled cyclic loading.

1.2 Objectives

The objectives of this study are summarized as follows:

- **Characterization of microstructural and mechanical properties of the brazed joints**

Microstructure and mechanical reliability of low carbon steel brazed joints with copper filler metal are investigated. The microstructure of the joint is studied to reveal possible sources of the joint failure. The joint tensile, shear and biaxial strengths are experimentally evaluated and numerically estimated by ABAQUS 6.7 software [4]. The resistance of the joints against crack propagation is evaluated by fracture toughness testing on single edge notched bend (SENB) and single edge notched tension (SENT) specimens. The corresponding joint failure mechanisms under different loading conditions are investigated as well.

- **Development of a methodology for fracture analysis of brazed joints using the CZM**

The CZM approach, as a fracture analysis tool, is employed to predict mode-I fracture and simulate ductile tearing process in the brazed joints. To this aim, the cohesive energy of the brazed joint is directly obtained from the results of the fracture test performed on the SENB specimens. Knowing the value of the cohesive

energy, the fracture test on the SENB specimens is modeled by ABAQUS 6.7, and a unique value for the cohesive strength is determined to best fit the experimental load versus crack mouth opening displacement (CMOD) curve. The predictability of the characterized CZM is explored by FE modeling of the tensile test performed on the SENT specimens. The good agreement between the FE simulation results and the experimental data confirms the applicability of the CZM for fracture analysis of the brazed joints.

- **Fatigue crack growth analysis of brazed joints using an irreversible CZM**

A cyclic damage evolution law is coupled to the CZM to account for the irreversible process of the joint stiffness degradation over the number of cycles. Fatigue failure behavior of the brazed joints is characterized by performing fully reversed strain controlled cyclic tests. The damage law parameters, which affect the rate of damage evolution in the cohesive zone FE model, are calibrated based on analytical solutions and the experimental fatigue crack growth (FCG) data. The characterized irreversible CZM shows applicability to FCG life prediction of brazed joints.

1.3 Thesis outline

The organization of the thesis is as follows:

In Chapter 2, failure studies of brazed and solder joints are reviewed. The CZM, as a fracture analysis tool is introduced, and its applications to failure analysis of interfaces under monotonic and cyclic loading conditions are discussed. Furthermore, a review on the CZM parameter determination approaches is presented.

In Chapter 3, the microstructural and mechanical properties of the brazed joints are characterized. The joint strength is experimentally measured and numerically estimated. The fracture toughness of the joint and the corresponding crack resistance curves for different specimen configurations are evaluated. Finally, the joint failure mechanisms under different loading conditions are investigated.

In Chapter 4, the CZM approach is used to predict the joint fracture strength and simulate the subsequent ductile tearing process. The cohesive energy is introduced based on the concept of the energy release rate and evaluated from the results of the fracture test. The cohesive strength is determined such that the numerical load-CMOD curve best fits the experimental results. The predictability of the obtained CZM is evaluated at the end.

In Chapter 5, fatigue crack growth in the brazed joints is modeled by an irreversible CZM. Strain-controlled fatigue tests performed on the brazed specimens are described, and the corresponding results in terms of fatigue crack initiation and propagation lives are presented. A cyclic damage evolution law is coupled to the CZM and calibrated to model fatigue crack growth behavior of the brazed joints.

Finally, in Chapter 6 the concluding remarks are presented and recommendations for future work are suggested.

Chapter 2

Literature Review and Background

In this chapter, theoretical background and literature review of failure studies of brazed and solder joints are presented. The cohesive zone model (CZM), as a fracture analysis tool is introduced, and its applications to failure analysis of interfaces under monotonic and cyclic loading conditions are reviewed. Finally, a review on the CZM parameter determination approaches is presented.

2.1 Introduction to brazing and soldering

Brazing and soldering are heat based joining processes in which a filler metal is melted to join base materials. In what follows, a brief description of these two processes is presented.

2.1.1 Brazing

Brazing, as a type of joining process, is widely used in manufacturing industries to join individual components of an assembly. In this process, a filler metal in the form of foil, wire, paste, plating, or powder with a melting point of above 450°C and below the solidus temperature of the base metal is melted and diffused into the faying surfaces of the individual parts to join them following solidification. Figure 2-1 shows the microstructure of the brazing process, schematically [1].

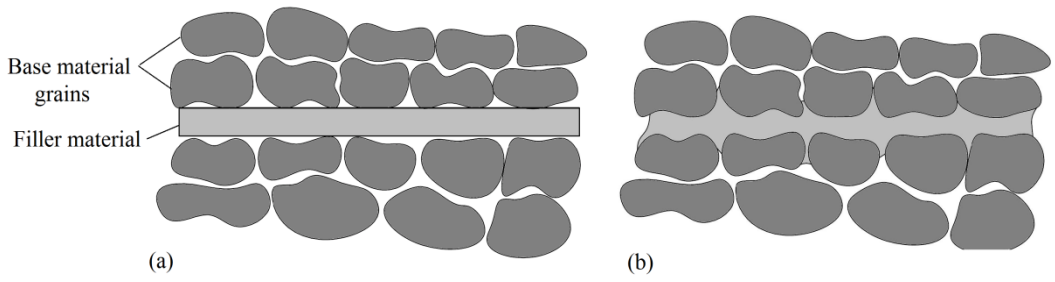

Figure 2-1- Microstructural schematic of the brazing (a) before, (b) after process

Compared with fusion welding, brazing techniques produce less thermal distortion due to uniform heating of components to the brazing temperature. Furthermore, preservation of metallurgical properties of the base metals, reduction of the induced residual stresses due to joining, more uniform distribution of applied loads over a larger joint area, excellent heat transfer properties, joining metals of a wide range of thicknesses, and producing joints with higher precision are among the advantages of brazed joints over weldments [5].

Several factors, such as filler metal flow properties, base metal characteristics, faying surface preparation, brazing hold time and temperature, joint design and clearance, and type of heating source, affect the quality of brazed joints. The type of heating source determines different types of brazing processes. These include: torch brazing, furnace brazing, induction brazing, dip brazing, resistance brazing, infrared brazing, laser brazing, exothermic brazing, weld brazing, and microwave brazing [1,5]. In this thesis, furnace brazing is used and discussed in the following.

- **Furnace brazing**

In furnace brazing, the filler metal is preplaced between the base materials faying surfaces. The components are then placed into an air-evacuated furnace which is purged with an inert gaseous atmosphere to prevent oxidation. The furnace is

heated up to the brazing temperature and, subsequently, the brazements are properly cooled down or quenched to create the desired properties in the base and filler materials. The filler metal used in the furnace brazing process can be in the form of foil, clad, powder, paste, wire, slug, shim, or tape [5].

Popularity of the furnace brazing method stems from the relatively low cost of the equipment, flux-free process of the furnace clean atmosphere, and the fact that post-braze cleaning of the brazements is not required. The other considerable feature of this technique is that the brazing assembly does not require any special kind of jigs; since, the weight of the parts or a few additional metallic blocks is sufficient as a fixture. Moreover, controlled heating cycles are another advantage of this method which makes automation of the process feasible to increase productivity [5].

2.1.2 Soldering

Soldering, as a subset of brazing is mostly used in joining electrical and electronic components. Although the bonding mechanisms of these two processes are similar, they can be distinguished from each other based on the melting point of the used filler metals. In addition, selection of the base and filler materials, heating methods, joint design, and the type of flux are among the factors which classify the

differences between these two processes. Some of the commonly used filler metals in the soldering process are alloys of Sn, Pb, Sb, Ag, Zn, or Cd, which have a liquidus temperature below 450 °C. These alloys provide good fluidity and wetting characteristics, acceptable strength, and often good electrical and thermal conductivity. Similar to brazing, type of heating source determines the type of the soldering techniques, i.e., iron soldering, torch soldering, oven soldering, dip soldering, wave soldering, induction soldering, and resistance soldering [1].

Due to popularity of the brazing and soldering processes in engineering applications, many investigations have been carried out to assess the reliability of a jointed structure. In the following section a review on the failure analyses of the brazed and solder joints is presented.

2.2 Failure studies of brazed and solder joints

Depending on the applications of the brazed and solder joints, their mechanical reliability is evaluated based on different criteria such as strength, fatigue life, and fracture toughness by the use of experimental, numerical, and analytical methods. In this section, investigations on different failure mechanisms of brazed and solder joints are reviewed.

2.2.1 Brazed joint failures

The structural reliability of a brazed assembly is strongly dependent on the joint mechanical properties. The mechanical reliability of brazed joints is characterized by various criteria such as strength, toughness, and fatigue properties [3]. Extensive experimental investigations have been carried out to characterize brazed joint mechanical properties influenced by different brazing conditions. In addition to the experimental studies, brazed joint failures have been investigated by numerical and analytical approaches.

The effects of different brazing conditions such as temperature, heating rate, holding time, and cooling process as well as the joint clearance on the joint strength and ductility have been experimentally investigated for a wide range of base and filler materials. Chen and Chin [6] investigated the influence of brazing hold time on the tensile and fatigue strength of brazed GlidCop Al-15 with copper filler metal. They observed that a shorter brazing cycle reduces the diffusion reaction and the corresponding brittleness at the joint interface which results in more ductility and strength. Nayeb-Hashemi and Lockwood [7] showed that increasing the brazing time for joining aluminum alloy 3003 plates by a layer of 4047 aluminum filler material increases the amount of shrinkage porosities in the diffusion layer which reduces the joint strength, remarkably. Nishi and Kikuchi [8] investigated the effect of filler

metal, joint clearance, and brazing time on the strength of alumina dispersion-strengthened copper/316 stainless steel brazed joints with silver-based and gold-based filler metals. They found out that the brazing filler metal has a significant effect on the joint strength as compared to that of the joint clearance and brazing hold time. They further observed that brazed joints with smaller grain size in the recrystallized diffusion layer show higher fracture strength. Nowacki and Kawiak [9] reported that increasing the joint thickness of steel/Cu/WC–Co cermet brazed joints reduces the joint rigidity, significantly. Dixon [10] investigated the effect of different filler metals and joint clearances on the joint strength in order to achieve the highest possible shear strength in metal/composite brazed joints. Environmental factors such as test temperatures and test media on the joint strength and embrittlement have been studied by Michler et al. [11].

In addition to the experimental investigations on brazed joint strength, several research studies have been conducted to estimate the joint tensile and shear strengths by numerical and analytical approaches. Assuming an ideal bonding between the base and filler materials, FE estimation of the joint interfacial stress distribution reveals possible failure locations within the joint [12-15]. Leinenbach et al. [13] used an in-situ approach for the measurement of the joint deformation during tensile testing to estimate the joint tensile strength with the help of FE modeling. Moreover, many researchers performed FE simulations to estimate brazing residual

stresses induced due to mismatch of thermal expansion coefficients of different base materials and predict their effect on the joint strength [16-19]. Using an analytical method, Saxton et al. [20] estimated the lower and upper bounds of the joint tensile strength as a function of filler metal yield and ultimate tensile strengths and the joint dimensions. Flom and Wang [21] proposed a damage zone failure criterion based on the filler metal equivalent Mises stress to predict shear strength of lap shear joints. Despite the fact that in practice brazed joints experience complicated loading conditions, prediction of the joint strength under a mixed loading condition has not been considered. Lee et al. [22] and Wung et al. [23] have proposed mixed mode failure criteria for prediction of spot weld strength for different types of applied loads. These failure criteria, in the form of power law equations, are capable of failure prediction of weldments based on the combination of single-mode strengths.

The reliability of brazed joints against propagation of pre-existing defects and cracks depends on the joint fracture properties. Based on the conventional fracture mechanics theory, the fracture toughness parameter has been used as the joint fracture criterion by many researchers [3,13,24-27]. The commonly used specimen configurations for fracture toughness testing of brazed joints are double cantilever beam (DCB), four-point bend beam, and notched tensile specimens [3,13,24,25,27]. In these specimens, electro discharge machining (EDM) technique is often used to introduce the initial crack required for performing fracture tests [3,13,25]. In some

cases, pre-cracking was done by applying static loading; however, difficulties regarding controlling the crack initiation makes this method less successful [24,27]. Moorhead et al. [24] and Gan et al. [3] investigated the variation of the joint fracture toughness with different types of filler metals and brazing temperatures. Kobayashi et al. [26] measured brazing residual stress field induced at ceramic/metal interface using the X-ray method and verified it by FE modeling. They showed that the existing residual stress field decreases the joint fracture toughness, noticeably. Moreover, using FE modeling, Fu et al. [25] and Philips et al. [27] calculated interfacial stress intensity factors for fracture specimens in order to estimate the joint toughness from a fracture test results. Although many investigations have been conducted to assess the brazed joint failure based on the fracture toughness parameter, it is widely accepted that the single-parameter fracture criterion shows dependency on the specimen geometry and loading [12,25,28]. A comprehensive fracture analysis tool capable of predicting fracture independent of geometry and loading configurations has not yet been applied to the brazed joints.

Fatigue crack initiation and propagation behavior of various brazed joints influenced by the brazing conditions, joint microstructure, and braze quality as well as environmental factors have been studied by many researchers. Yu and Lai [29] studied the effects of gap filler and brazing temperature on failure of brazed joints. They found that increasing brazing temperature as well as addition of gap filler at

elevated temperatures improves fatigue crack initiation and propagation resistance of the joint. Gao and Qiana [30] used the micro-indentation technique to investigate the micromechanical properties of different regions of heterogeneous aluminum/silicon brazed joint. Regions with higher Young's modulus and initial yield limit were identified as the weakest sites for fatigue crack initiation. Solomon [31] statistically investigated the influence of voids and lack of braze (LOB) points on the fatigue life of a brazed joint. As the LOB increases, the load bearing area decreases; therefore, the fatigue strength capacity of the joint reduces. Gan et al. [32] experimentally studied the fatigue failure mechanisms of vanadium alloy/stainless steel brazed joints. They identified two different mechanisms of cohesive and mixed mode adhesive-cohesive failures. A pure cohesive fracture mechanism was observed at the areas with stable fatigue crack growth, while the unstable fatigue crack growth caused a mixed mode failure mechanism. The effect of corrosion mechanism on fatigue life of low pressure steam turbine blades was studied by Mukhopadhyay et al. [33]. Waddell et al. [34] investigated the failure mechanism of brazed joints used in implant-supported overdentures. It was observed that corrosive environment along with masticatory cyclic loading was the primary factor in fatigue failure of the joints. A few researchers have characterized the fatigue behavior of brazed joints using empirical equations. Brossa et al. [35] studied fatigue crack growth behavior of AISI 316L brazed joints using compact tension (CT) specimens and obtained the

Paris law coefficients based on the corresponding experimental data. Furthermore, they characterized the Coffin-Manson relation based on the low cycle fatigue (LCF) tests performed on the round smooth brazed specimens. Leinenbach et al. [36] characterized the Paris law relation for martensitic stainless steel brazed joints and obtained a large value for the Paris law exponent. As a result, the rate of fatigue crack growth was found to be very sensitive to the load ranges. Although the Paris law has been used for fatigue crack growth analysis of brazed joints, it should be considered that the crack growth behavior at interfaces shows dependency on geometry and loading. Hence the characterized Paris law for a brazed joint loses its transferability to different joint configurations [37]. Therefore, a fracture analysis approach which predicts brazed joints fracture independent of the joint configurations under monotonic and cyclic loading conditions is necessary.

2.2.2 Solder joint failures

Solder joints are widely used in internal connections of electronic devices; hence many investigations have been conducted in the literature in order to identify their failure mechanisms. Thermal fluctuation in an electrical device affects the solder joint failures. This becomes a dominant failure factor at the joint regions having different thermal expansion coefficients or experiencing high temperature gradients and stress concentrations during service time. Solomon [38]

experimentally studied the fatigue behavior of 60Sn/40Pb solder joints under different working temperatures. At each isothermal cyclic shear test, he measured the joint fatigue lives for different plastic strain ranges and characterized the Coffin-Manson equation for each thermal condition. Using the energy approach, Solomon estimated the joint fatigue life and compared it with the results of the Coffin-Manson plastic strain based equation [39,40]. In another study, Solomon et al. [41] modified the laboratory LCF curves in order to predict the fatigue life of actual solder joints. Zhang et al. [42] included the effect of material degradation into the Coffin-Manson relation using a damage evolution model which was obtained experimentally based on the measured creep hysteresis loops. This way, they avoided the assumption of constant material properties in the Coffin-Manson relation which overestimates the fatigue life under thermal cycles. Zhao et al. [43] proposed the method of interfacial boundary volume based on a damage criterion combined with the modified Coffin-Manson equation for fatigue life prediction of solder joints. In this approach, the damage parameter was calculated for the thin solder interlayer to determine the empirical coefficients of the Coffin-Manson relation. In a study on solder joints reliability by Kim et al. [44] two different failure mechanisms, i.e., brittle interfacial failure and thermal fatigue cracks, were identified in thermal shock tests. Furthermore, several other experimental studies have contributed to the fatigue-fracture investigations of solder joints including [45-47].

Yang et al. [48] employed a cohesive zone approach for fatigue life prediction of solder joints. The CZM, which correlates the interfacial traction and separation, was coupled with a plastic strain based damage evolution law. Accumulating the damage variable, the joint stiffness was degraded in each loading cycle. Using this approach, they successfully included the material nonlinearity in the analysis, and predicted the fatigue life of solder joints under different loading conditions and geometries. Abdul-Baqi et al. [49] presented another damage coupled CZM law motivated by the formulation of Roe and Siegmund [37] to predict the fatigue life of the solder joints. The results were in good agreement with the life predicted by the empirical Coffin-Manson relation.

In this research, due to applicability of the CZM to nonlinear fracture analysis and its capability for joint failure prediction independent of specimen configurations [37,50], this approach has been applied for fracture analysis of brazed joints. In what follows, concept and applications of this approach are reviewed.

2.3 Cohesive Zone Model (CZM)

The CZM, as an interfacial constitutive law, is used to model crack initiation and propagation under monotonic and cyclic loading conditions. In this section, the

CZM approach is introduced first and its applications are reviewed. Development of the CZM constitutive equations in a continuum damage mechanics (CDM) framework is given in Appendix A.

2.3.1 Introduction to the CZM

The CZM approach provides an interfacial constitutive model by defining a relationship between traction and separation at the fracture process zone (FPZ). The CZM concept was initially proposed by Dugdale [51] and Barenblatt [52] in order to model crack initiation and subsequent propagation [53]. The CZM is characterized by two parameters of the cohesive strength and cohesive energy. The cohesive strength, denoted by $\sigma_{max,0}$, is the maximum attainable traction at the fracture process zone at the onset of damage initiation. The cohesive energy, Γ, quantified by the area under traction-separation curve, is the work required for complete material separation per unit area of the crack advance [48]. Figure 2-2 illustrates the fracture process zone developed from the material crack tip (point E) to a fictitious point (point A), known as the mathematical crack tip. The separation variable, U, is defined as the relative opening displacement of the top and bottom faces of the crack $U = U^{top} - U^{bottom}$. Upon increasing the separation from point A to point C, the traction, T, increases from zero up to the cohesive strength in the forward region of

the crack. Thereafter, by increasing the separation, traction gradually decreases along the crack wake region and eventually vanishes once the separation reaches its critical value, δ_c, which leads to formation of two physically separated surfaces at point E [54,55].

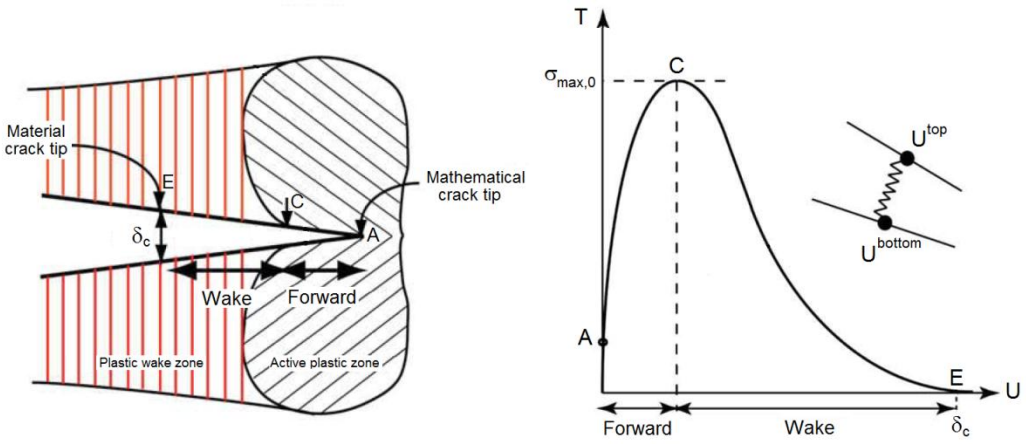

Figure 2-2- Schematic of the fracture process zone and the CZM [54]

In contrast to the conventional fracture mechanics approach, that decouples the crack initiation and propagation mechanisms, these two subsequent processes are naturally obtained from the CZM approach [48]. Furthermore, the issue of nonphysical stress singularity at the crack tip in the conventional fracture mechanics analysis is resolved when the CZM technique is used [50,56]. Another important advantage of the CZM approach is its applicability to the fracture analysis of structures exhibiting material and geometric nonlinearities [50]. Moreover, this method is particularly a powerful tool for crack growth analysis at interfaces with

complex crack tip fields. Using the CZM, the energy needed for decohesion is decoupled from the energies dissipated by other irreversible mechanisms such as large-scale plasticity around the crack tip. This implies that once the CZM is characterized for an interface, it is applicable to other geometry and load configurations for predicting interfacial crack growth behavior [37].

2.3.2 The CZM traction-separation functions

As mentioned in the previous section, the CZM is governed by a relation between traction and separation at the fracture process zone. For this purpose, several traction-separation laws (TSL) have been proposed which are illustrated in Figure 2-3. Needleman [55] assumed traction as a cubic polynomial function of separation, shown in Figure 2-3 (a), in order to describe the fracture process from void nucleation up to complete decohesion in an elastic-viscoplastic material. An exponential form of the traction-separation law, shown in Figure 2-3 (b), was suggested by Needleman [57] to model the decohesion process along the interface of a viscoplastic block and a rigid substrate. Tvergaard and Hutchinson [58] proposed a trapezoidal form, shown Figure 2-3 (c), to model crack initiation and its corresponding resistance curve in elastic-plastic materials. Schwalbe and Cornec [59] considered a constant traction when the separation increases along the process zone, as shown in Figure 2-3 (d). A bilinear model, shown in Figure 2-3 (e), can be

introduced as a special type of the trapezoidal form which has been employed by many researchers [60-63].

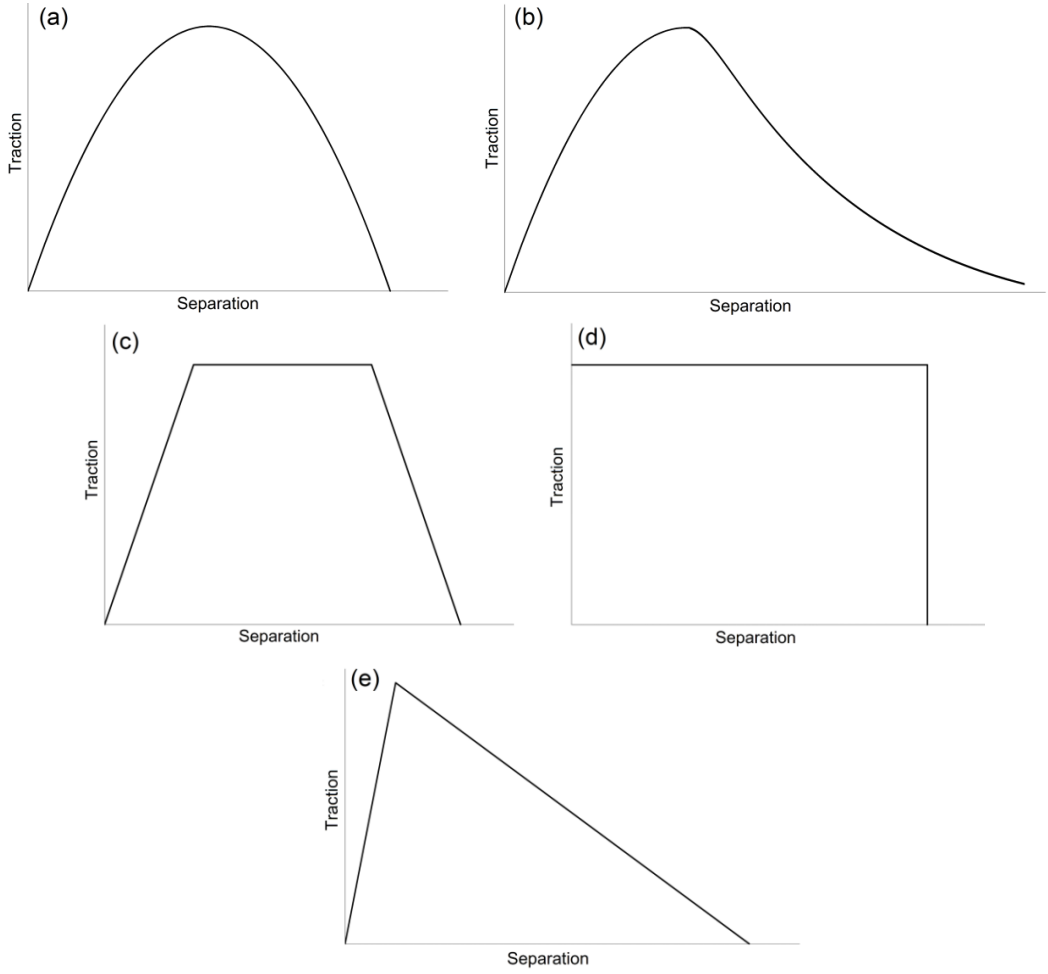

Figure 2-3- Different types of the CZM functions: (a) cubic polynomial, (b) exponential, (c) trapezoidal, (d) constant, and (e) bilinear TSL

2.3.3 Applications of the CZM to failure analysis

The CZM, which was first proposed as an alternative approach to the conventional fracture mechanics, has received lots of interest for its applicability to a wide range of failure analysis. Tvergaard and Hutchinson [58,64,65] extended the application of the CZM for fracture modeling of adhesively bonded multilayer structures under monotonic loading. Yang et al. [66] employed the CZM to model mode II fracture of an adhesive joint with considerable plastic deformation in adherents. Using the same cohesive zone properties, they successfully simulated the fracture process of adherents with different geometries and showed the predictability of the CZM for various joint configurations. The CZM has achieved popularity in simulation of the fracture process in composite materials, as well [60]. The CZM-based delamination analyses of bimaterial interfaces in laminated [67-69], fiber [60,61,70,71] and honycomb [72] composite structures have been carried out by many researchers. Bosch et al. [73] implemented large deformation theory into the classical small displacement CZM to model delamination of a polymer coating from a steel substrate. Moreover, the CZM has been successfully employed for modeling damage propagation in adhesive joints [62,74-79].

In addition to the applications of the CZM to fracture analysis under monotonic loading, numerous researches have been focused on using an irreversible

CZM for fatigue analysis of interfaces [80]. De-Andres et al. [81] were among the first to employ the damage mechanics concept into the CZM in order to study the elastic-plastic fatigue crack growth of an elliptical crack in an aluminum shaft under axial cyclic loading. Yang et al. [80] introduced a damage parameter into the constitutive model of an interface to degrade the CZM stiffness over cycles and simulate fatigue crack growth behavior. Nguyen et al. [82] proposed an exponential decay function to degrade the CZM stiffness over the loading cycles and account for hysteresis effect in unloading-reloading paths which prevents shake down in fatigue crack growth analysis. Another cyclic damage evolution model for fatigue crack growth analysis was proposed by Roe and Siegmund [37]. Based on this damage model, Wang and Siegmund [83] simulated fatigue crack growth in a ductile metallic layer which was sandwiched between two elastic substrates. Using the CZM with a unique set of the parameters, they successfully predicted the constraint effect of the elastic substrates on the fatigue crack growth rate in the ductile layer. Moreover, this cyclic damage evolution model was later extended to other applications such as fatigue crack growth analysis in single crystal super alloys [54] and solder joints [49]. Yang et al. [48] proposed a cyclic damage evolution model as a function of accumulated plastic strain to model cohesive strength degradation and predict the crack initiation life of solder joints. Recently, Khoramishad et al. [84] have proposed a cyclic damage model based on the maximum principle strain of the

interface implemented in the CZM to predict fatigue crack initiation and propagation life of adhesively bonded joints under mixed mode loading.

The predictability of the CZM in different failure situations relies on the use of proper model parameters in the analysis. This necessitates suitable methods for determination of the CZM parameters. Some of the proposed methods for the CZM parameters determination are reviewed in what follows.

2.3.4 Determination of the CZM parameters

The two characterizing parameters, i.e., the cohesive strength and the cohesive energy, can be determined by different approaches. In general, a priori shape of the CZM function is assumed in the most of parameter determination techniques. The characterizing parameters are then obtained through experimental measurements accompanied by curve fitting of the CZM simulation results to the experimental data [66,75,77,85-88]. A brief review on the proposed methods for the CZM parameter determination is presented below.

Yang et al. [66] estimated mode II cohesive strength by performing a torsion test on adhesive joints. In order to obtain mode II cohesive energy, a three-point bend test on adhesively bonded end-notched flexure (ENF) specimens was performed and modeled using the cohesive zone FE method such that the numerical

load-displacement curve matches the experimental one. Chandra [60] studied the interfacial failure in metal matrix composites using the CZM. He characterized the interfacial work of separation based on the area under load-displacement curve obtained from a push-out test. Then the cohesive strength was numerically adjusted such that it best fits the experimental results. Sorensen and Jacobsen [87] proposed an approach for the determination of the cohesive law from the measured crack resistance curve in elastic bodies. They obtained the stress-opening curve as a cohesive law by differentiating the experimental resistance curve with respect to the crack opening displacement. Chen et al. [88] estimated the separation energy by topographic measurement of the corresponding fracture surface halves of the tensile specimens. Following the determination of the separation energy, the cohesive strength was determined by fitting the simulated crack length-load line displacement curve to the experimental one. Liljedahl et al. [75] identified the crack initiation point on the experimental load-displacement curve and introduced its corresponding stress level as the cohesive strength. The cohesive energy was then determined by matching the numerical load-crack extension curve to the experimental one. Que and Tin-Loi [86] simulated mode I fracture process in quasi-brittle materials using different TSLs. They estimated the corresponding CZM parameters by an optimization technique and minimized the error between their FE and experimental load-displacement curves. Salomonsson and Andersson [77] employed the CZM to

simulate tensile and shear modes of failure at meso-scale adhesive layers. They captured the adhesive layer deformation by in-situ SEM measurement technique and calibrated the CZM parameters by an optimization method in order to best fit the simulation results to the experimental data.

Consequently, in the cases that the two model parameters have been simultaneously identified by optimization techniques to best fit the FE simulation results to the experimental data, the uniqueness of the obtained parameters is debatable [71,75]. On the other hand, characterization of one model parameter by direct measurement from experiment and the other one by fitting the simulation results to the experimental data leads to a unique set of the model parameters [85,88].

2.4 Summary

In this chapter, different joining processes of brazed and soldered joints were reviewed and the corresponding experimental, numerical, and analytical failure studies were presented. Despite the extensive investigations on different failure mechanisms of brazed joints, a comprehensive fracture analysis approach has not been employed to predict failure of brazed joints independent of geometry and

loading configurations. Among the different approaches for failure analysis of solder joints, the CZM was introduced as one of the recent approaches for interfacial failure analysis under monotonic and cyclic loading conditions. This approach, as a fracture analysis tool, and its advantages and capabilities over the conventional fracture mechanics were reviewed. Due to applicability of the CZM to nonlinear fracture analysis as well as its predictability of interfacial failure independent from geometry and loading configurations, this approach has been applied to the monotonic and cyclic crack growth analysis of brazed joints in the current research.

Chapter 3
Microstructural and Mechanical Characterization

In this chapter, microstructure and mechanical properties of low carbon steel brazed joints with copper filler metal are investigated. The microstructure of the joint is studied to reveal possible sources of failure. The joint tensile, shear, and biaxial strengths as well as the joint fracture toughness and its corresponding crack resistance curve are evaluated. Finally, the joint failure mechanisms under different loading conditions are investigated.

3.1 Microstructural characterization

Samples of steel/Cu/steel brazed joints were prepared for the microstructural analysis. To this end, blanks of low carbon steel (ASTM A36) with dimensions of 40mm×19mm×50mm were cut and the related faying surfaces were ground with 240 grit silicon carbide sand paper. The chemical composition of the low carbon steel (ASTM A36) used here is listed in Table 3-1.

Table 3-1 Chemical composition of steel (ASTM A36) as the base metal [89]

Composition	C	Mn	S	Si	P
Weight%	0.25 max	0.80-1.20	0.05 max	0.40 max	0.04 max

The steel blanks were cleaned by immersing them in an ultrasonic bath of acetone for 5 min. Copper brazing filler metal (AWS BCu-1), in the shape of 75-μm thick cold rolled foil and purity of 99.95%, was cut and placed between the faying surfaces. A steel shim with the thickness of 50 μm was placed at four corners between the faying surfaces to preserve a uniform joint clearance during the brazing process. The assembly was constrained on both sides and placed into the brazing furnace. The furnace was evacuated first by a diffusion pump and then purged by Argon inert gas with a dynamic pressure of 20 kPa. The furnace was then heated to 1110°C and held for 30 min at this temperature to let the copper melt, flow, and

diffuse into the base metals. The samples were furnace cooled at the end of the brazing process. The joint cross section was ground and polished with 1µm diamond paste and etched using a 2% Nital solution to reveal the joint microstructure.

Figure 3-1 (a) shows the SEM backscattered electron image (BEI) of the joint etched cross section taken on a magnification of 1000x. The joint has a uniform thickness of about 50µm and no noticeable defect such as porosities or cracks were observed on the joint cross section. To determine element composition of the different regions shown on Figure 3-1 (a-c), the energy dispersive X-ray spectroscopy (EDS) chemical analysis was performed, and the results are summarized in Table 3-2. Region A is the joint interface where molten copper has diffused into the base metal. Region B which is shown in Figure 3-1 (b) consists of MnS-rich dendrites which came from steel composition dissolution into the molten copper and formed during solidification. Figure 3-1 (c) shows the finer Fe-rich dendrites formed during solidification, as well. All these dendrites within the copper matrix are the possible failure locations in the mechanical testing which will be discussed in the next sections.

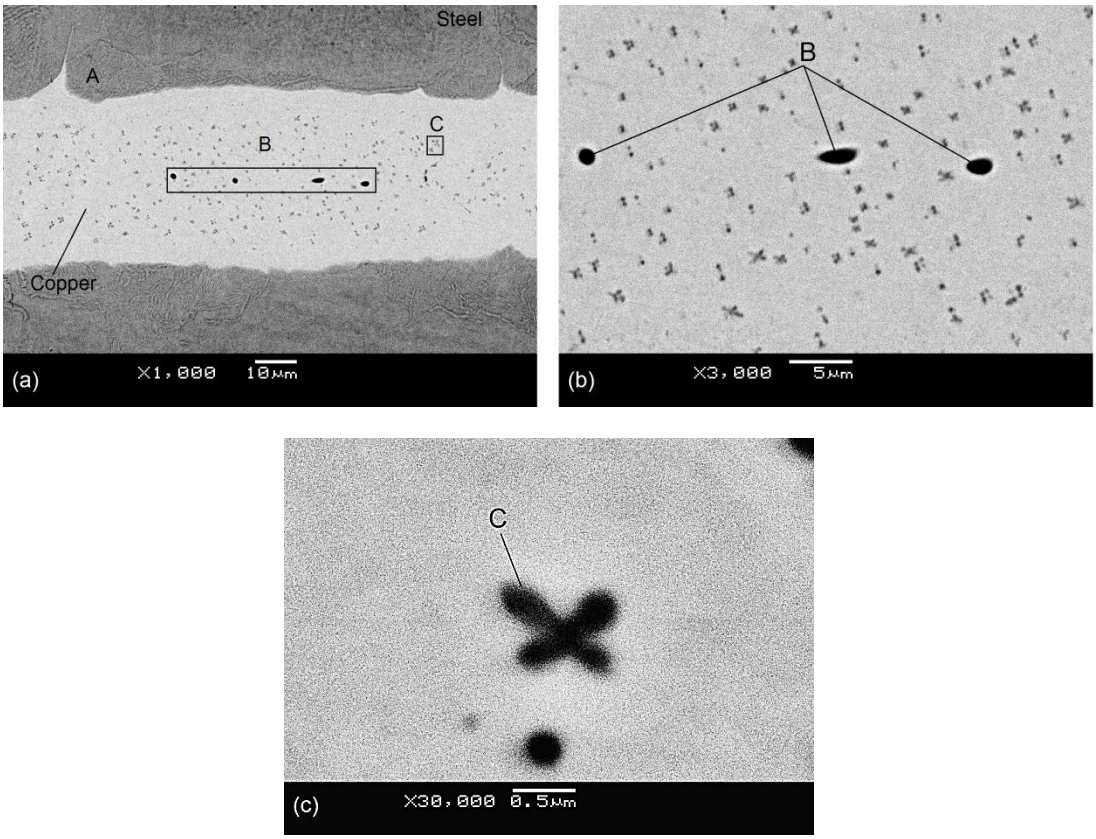

Figure 3-1-SEM-BEI images of the joint cross section (a) 1000x, (b) 3000x, (c) 30,000x

Table 3-2 Weight % of brazed joint element composition from EDS analysis

Region	A	B	C
Fe	82.6	1.5	9.9
Cu	17.4	48.2	90.1
Mn	0	30.2	0
S	0	20.1	0

3.2 Mechanical characterization

In this section, the mechanical reliability of the brazed joints is investigated. The tensile and shear strengths of the joint are evaluated by tension and torsion tests performed on butt-brazed joint specimens, respectively. The biaxial tension-torsion tests are carried out to characterize the joint behavior under a mixed mode of loading. The joint strength and deformations are numerically estimated using ABAQUS 6.7 commercial FE software [4]. Moreover, resistance of the brazed joint against crack propagation is evaluated by fracture toughness testing on SENB and SENT specimens. Finally, the joint failure mechanisms are investigated.

3.2.1 Strength evaluation

In this section, the experimental procedures for tensile, shear and biaxial strength evaluation are provided first. Then, the numerical simulations are performed to model the joint deformations and estimate the joint strengths. The experimental and numerical results are presented at the end of the section.

3.2.1.1 Experiment

The strength of the butt-brazed joint in the normal direction was measured by tensile testing. Flat dog-bone shaped tensile specimens (Figure 3-2) with a central joint were machined from a brazed block. To investigate the effect of the base metal

yield limit on the joint tensile strength, tensile specimens with a different base metal of low carbon steel, ASTM A108, were prepared as well. Uniaxial tensile tests were performed using servo hydraulic Instron tensile machine under a displacement controlled condition with a rate of 0.005 mm/s.

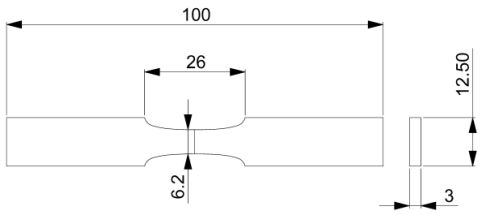

Figure 3-2- Dog-bone shape specimen with a central joint for tensile test (dimensions in mm)

The shear strength of the butt-brazed joint with the base metal of low carbon steel, ASTM A36, was evaluated by means of torsion testing under rotation controlled condition and a rate of 0.05 degree/s. Thin-walled tubular shape specimens with a central joint (Figure 3-3), recommended by ASTM E2207, were machined from a brazed block and used for the torsion test so that the assumption of uniform shear stress distribution on the joint cross sectional area is valid [90].

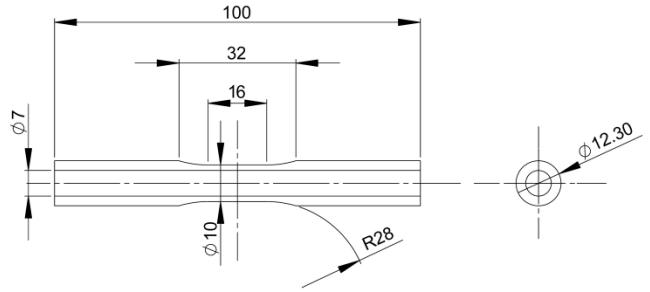

Figure 3-3- Round tubular specimen for torsion and biaxial tests (dimensions in mm)

In addition, biaxial tension-torsion tests with different extension to twist angle ratios were performed on the same tubular shaped specimens to characterize the joint strength in a general state of loading. Tensile and shear strains were measured by a 10-mm gage length biaxial extensometer.

3.2.1.2 Numerical modeling

To model the brazed joints deformation and failure, the tensile, torsion and biaxial tests are numerically simulated using the ABAQUS 6.7 software. Figure 3-4 shows a 3D model of the half 10-mm gage section of the tensile specimen. A quarter of the specimen is modeled due to the presence of two symmetric planes. Symmetric boundary condition is placed on the mid-plane of the joint and half of the experimentally measured extension within the gage section is applied at the end of the model. Quadratic hexagonal solid elements (C3D20) were used in the simulation.

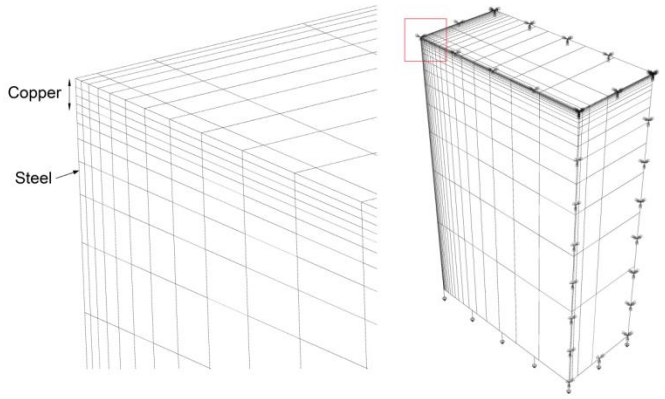

Figure 3-4- FE model and boundary conditions of the tensile specimen

The joint is modeled as a bi-material and the corresponding bulk material properties are assigned to the base and filler metal sections. Mechanical properties of the two base metals determined by tensile tests are presented in Table 3-3, and the corresponding hardening behaviors are shown in Figure 3-5.

Table 3-3 Mechanical properties of the base metals

Material	Elastic modulus [GPa]	Poison's ratio	Yield strength [MPa]
Low carbon steel (A108)	200	0.3	338
Low carbon steel (A36)	200	0.3	220

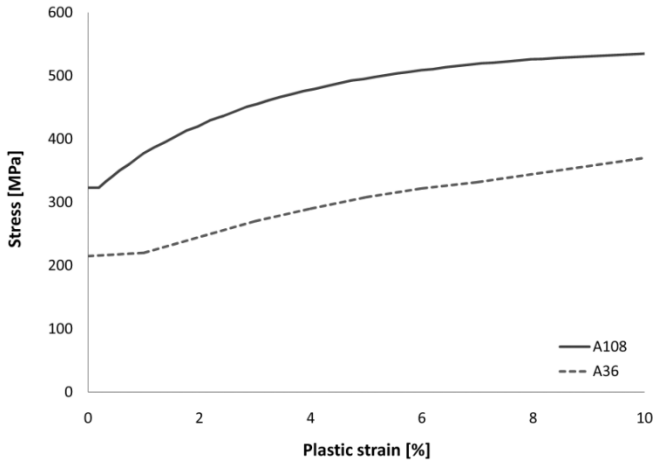

Figure 3-5- Stress-plastic strain curves of the two base metals

The mechanical properties for the filler metal are assumed to be the same as its pure bulk material properties [91]. In this simulation, an elastic modulus of 82

GPa, a Poisson's ratio of 0.34, and a yield limit of 215 MPa are used for the copper filler metal [92]. A power law hardening model is used for the copper as follows:

$$\sigma_{Mises} = 450(0.025 + \varepsilon^{p})^{0.20} \quad (3\text{-}1)$$

where σ_{Mises} and ε^{p} are the equivalent Mises stress and the corresponding equivalent plastic strain, respectively [92].

To simulate the deformation of the tubular specimens in torsion and biaxial tests, the 10-mm gage section of the tubular specimen is modeled. Axisymmetric 8-noded quadrilateral elements (CAX8) are used in the simulation. One end of the model is fixed and the experimentally measured extensions and twist angles with different ratios are applied to a reference point (RP) coupled to the other end of the model, as shown in Figure 3-6.

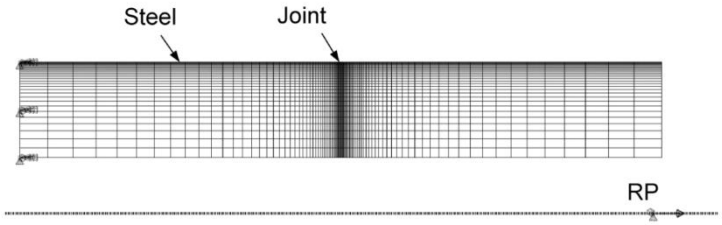

Figure 3-6- Axisymmetric FE model and boundary conditions of the tubular specimen

3.2.1.3 Experimental and numerical results

Engineering tensile stresses versus tensile strains obtained from the experiment and FE simulation of the brazed specimens with the base metals of

different yield limits are presented in Figure 3-7. For the ease of comparison, the tensile strengths of the different specimens are summarized in Table 3-4. In the numerical modeling, the base metal tensile stress corresponding to the maximum applied extension is taken as the joint tensile strength.

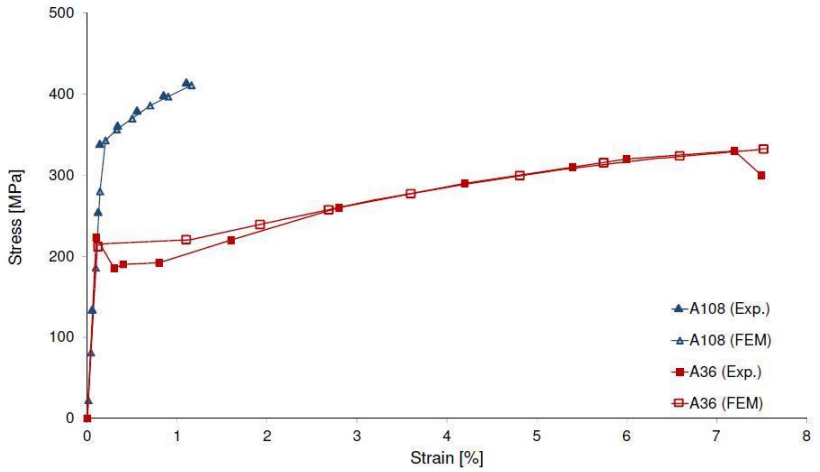

Figure 3-7- Experimental and numerical tensile stress-strain curves of the tensile specimens

Table 3-4 Brazed joint strength for base metals with different yield limits

Base metal alloy	Base metal yield limit [MPa]	Experimental tensile strength [MPa]	FEM tensile strength [MPa]
A108	338	417	418
A36	220	330	332

The equivalent Mises stress distribution obtained from FE modeling of the tensile specimens, Figure 3-8, shows that the external corner of the joint is the

critical location for failure. Applying the experimentally measured extension to the FE model, the predicted strengths from the FE simulation agree well the experimental results.

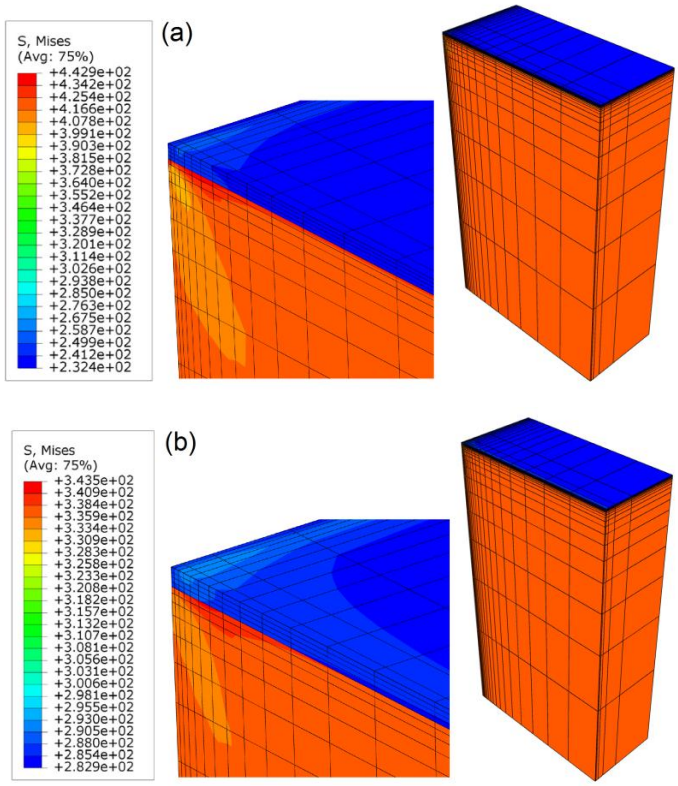

Figure 3-8- Equivalent Mises stress distribution in the tensile specimens with the base metal of (a) A108, and (b) A36

The results show that brazed joint tensile strength improves by increasing the base metal yield limit. The effect of the base metal yield limit on the joint tensile strength is related to the constraints imposed by the base metal on the joint region [20]. In the case that the filler metal yield limit is less than that of the base metal, the

joint tends to deform plastically under the lateral constraint imposed by the base metal elastic deformation. This constraint induces a high triaxial state of stress in the joint region. As shown in Figure 3-9, this constraint vanishes upon reaching the base metal yield limit and allows the filler metal to deform plastically. Therefore, a base metal with a higher yield limit promotes the joint tensile strength by delaying the filler metal extensive plastic deformation to a higher applied load level.

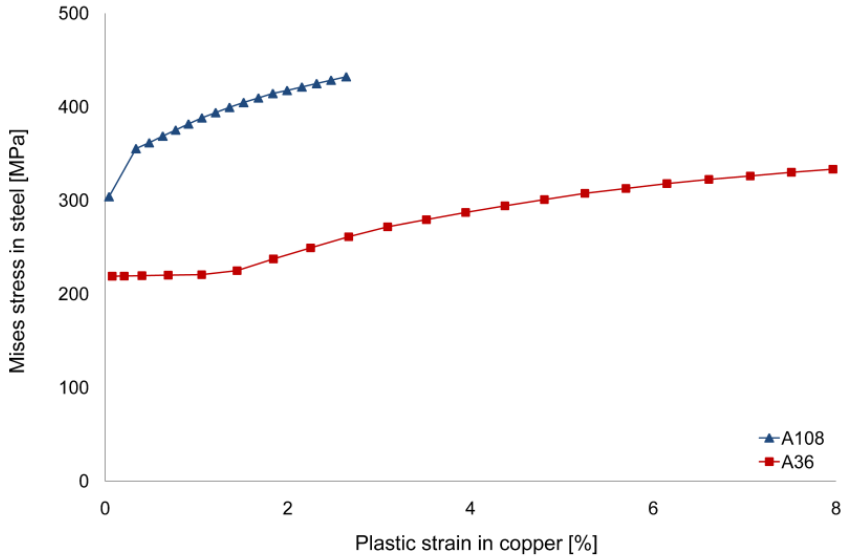

Figure 3-9- Mises stress in steel versus copper plastic strain for the two base metals

Torque versus cross-head rotation obtained from the torsion test is plotted in Figure 3-10. The maximum recorded torque at the onset of failure was 42 N.m.

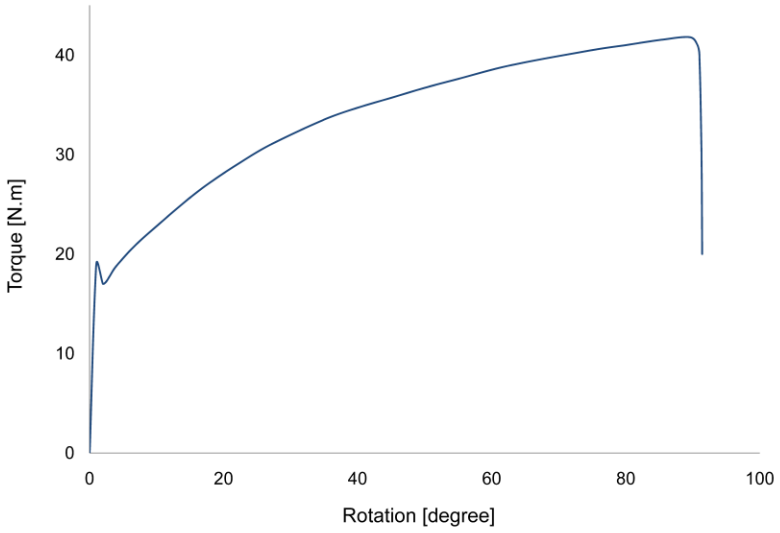

Figure 3-10- Torque versus cross-head rotation obtained from the torsion test

The average shear stress, τ_{ave}, for thin-walled tubular specimens under applied torque,T, is calculated from equation (3-2).

$$\tau_{ave} = \frac{16T}{\pi\left(d_o^2 - d_i^2\right)(d_o + d_i)} \tag{3-2}$$

where d_i and $d_o$are inner and outer diameters of the specimen, respectively [90]. Using equation (3-2), average ultimate shear strength of 246 MPa for the joint is estimated.

Figure 3-11 shows the experimental and numerical shear stress versus the shear strain at the outer diameter of the torsion specimen. The results obtained from the FE simulation are in good agreement with the experiment.

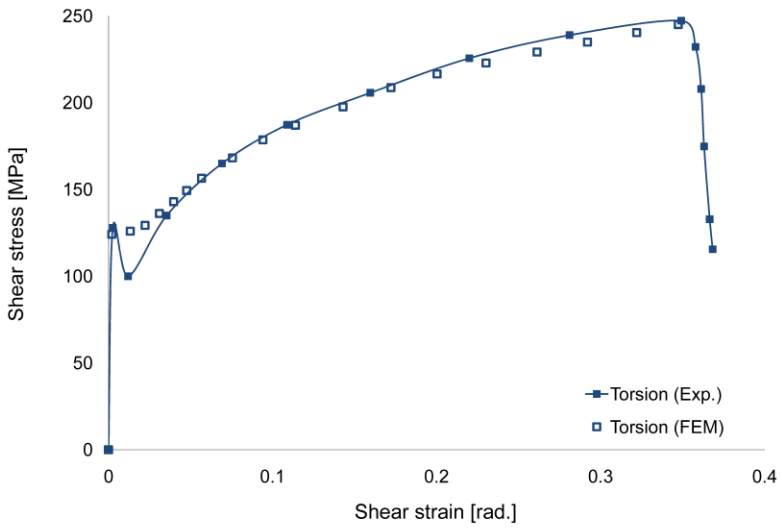

Figure 3-11- Experimental and numerical shear stress-strain curves of the torsion test

The shear and equivalent Mises stress distributions obtained from FE simulation of the torsion test are shown in Figure 3-12. The 2D axisymmetric model is swept 90 degree about its axis for a 3D visualization. The shear and equivalent Mises stresses have uniform distributions in the base and filler metal regions and other stress components are zero in the whole model. Consequently, unlike the tensile specimens no base metal constraint effect is imposed on the filler metal region.

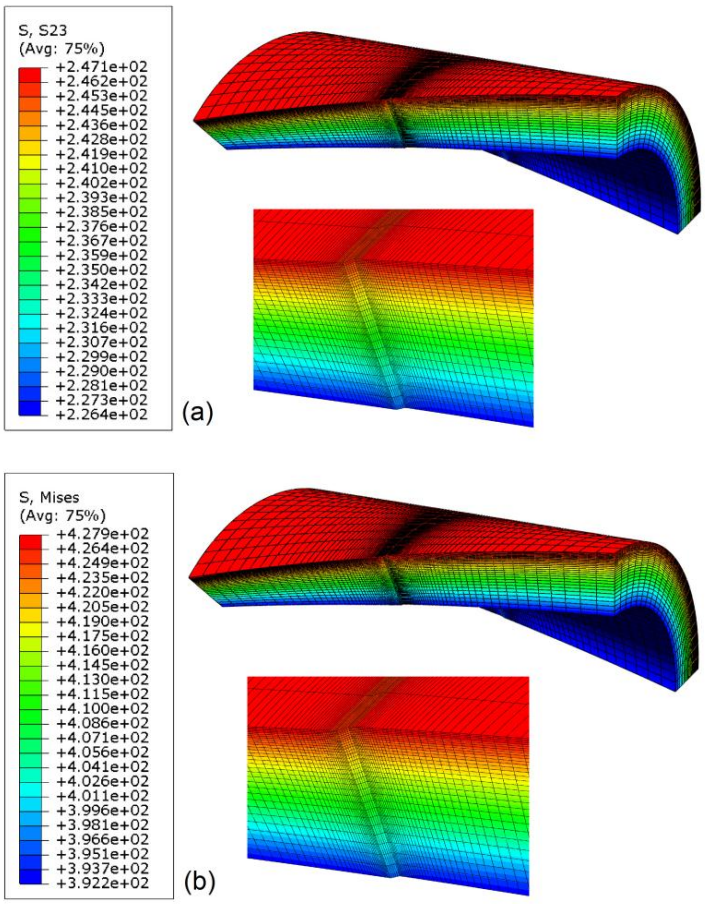

Figure 3-12- (a) Shear (S23), (b) equivalent Mises stress distributions due to torsion (in MPa)

Experimental results of the biaxial tension-torsion tests with different applied extension to twist angle ratios are summarized in Table 3-5. Results obtained show that upon increasing the ratio of extension to twist angle, the contribution of the tensile to shear stresses at failure increases.

Table 3-5 Results of the tension-torsion tests with different deformation ratios

Specimen ID.	Base metal ASTM specification	Extension/ Twist angle (R) [mm/ degree]	Tensile strength [MPa]	Shear strength [MPa]
1-A	A36	0	0	246
2-B	A36	0.013	106	225
2-A	A36	0.035	251	166
3-B	A36	0.040	246	148
3-A	A36	0.045	257	150
C	A36	∞	330	0

Figure 3-13 compares the experimental tensile and shear stress-strain curves with the results obtained from the FE simulation of the biaxial tests. The numerical results are in good agreement with that of the experiment.

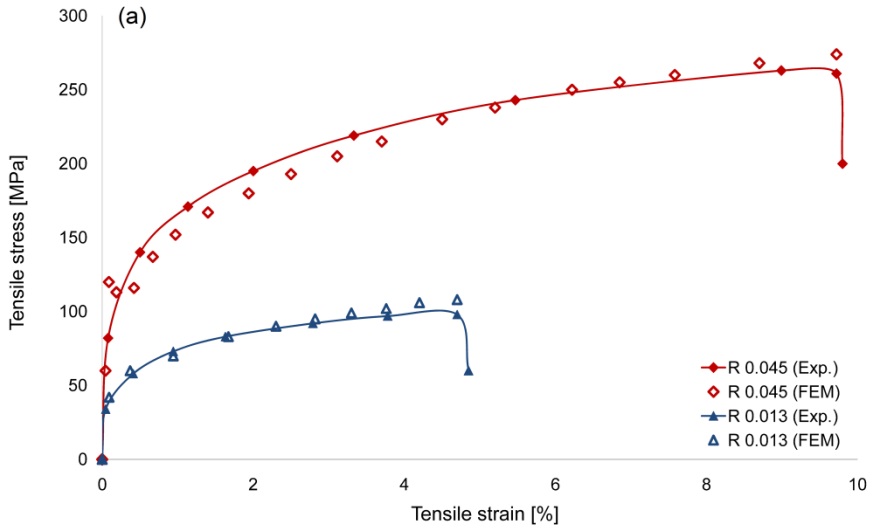

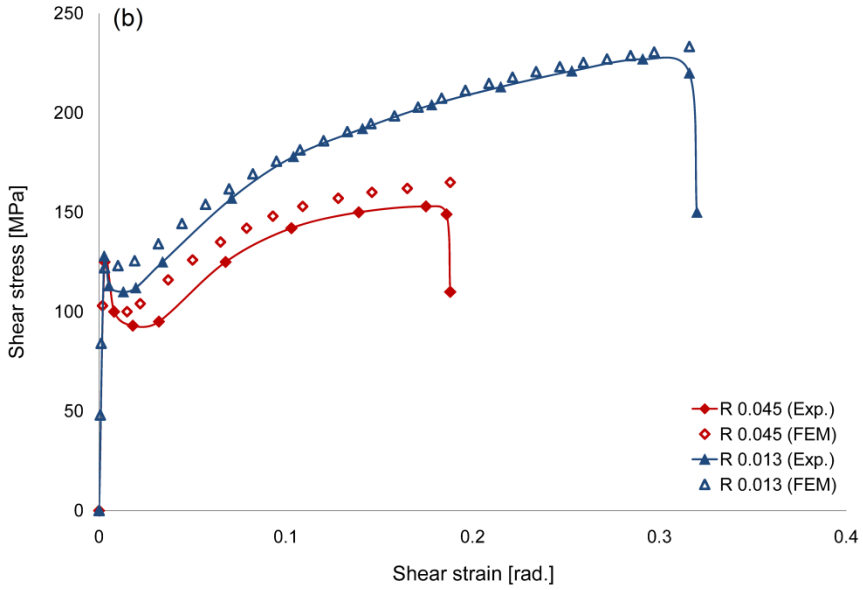

Figure 3-13- Experimental and numerical stress-strain curves of the biaxial tests in (a) tensile and (b) shear directions

To predict biaxial strength of the joint, a stress based power law failure criterion proposed for spot welds is used in this study. This failure criterion, expressed in terms of the previously obtained single mode tensile, S_{tu} , and shear, S_{su}, strengths, is as follows [22]:

$$\left(\frac{S_t}{S_{tu}}\right)^{\alpha} + \left(\frac{S_s}{S_{su}}\right)^{\alpha} = 1 \qquad (3\text{-}3)$$

where S_t and $S_{s,}$ are tensile and shear stresses at failure, respectively.

According to the test data, the best fit is obtained when the value of α equals to 1.85 as shown in Figure 3-14. The numerically predicted biaxial strengths are in

agreement with the failure criterion. The results show that in addition to the single mode strengths in tensile and shear directions, the biaxial strengths of the joint are numerically well estimated. Furthermore, the power law failure criterion in terms of single mode strengths is well suited to the nature of biaxial failure in brazed joints.

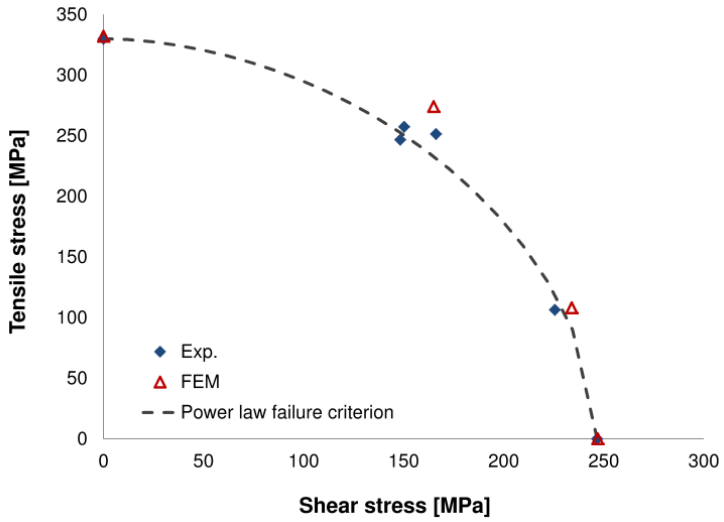

Figure 3-14- Power law failure criterion curve fit to the biaxial test results

3.2.2 Fracture toughness evaluation

In this section, the fracture toughness of the brazed specimens is evaluated. For this purpose, a starter crack is produced inside the single edge notched brazed specimens. Using load, crack mouth opening displacement (CMOD), and crack extension recorded during the tests, the joint fracture toughness values for the SENB

and SENT specimens are calculated, and the corresponding crack resistance curves are plotted and compared for the two types of the specimens.

3.2.2.1 Experiment

Pre-cracked brazed specimens were used to obtain the joint fracture toughness and crack resistance curve by a fracture test. The ASTM E1820 standard recommended crack depth to the specimen width ratio of 0.5 was selected for all of the specimens [93]. To create the starter crack inside the joint, half portion of the faying surfaces were coated by means of NICROBRAZ Green Stop-off Pen containing ceramic powder to prevent this portion from brazing. Since the stop-off material solvent has a boiling temperature of 82°C, it easily evaporates during brazing and produces gas bubbles which are trapped inside the joint. In order to avoid gas porosities in the joint, the coated faying surfaces were preheated inside a furnace up to 100°C for 20 min before assembling. The copper foil with the thickness of 75 µm was cut and placed on the other half portion of the specimen. As previously mentioned, steel shims were used as spacers during the brazing process. The brazing assembly and detail of the joint faying surface are shown in Figure 3-15. The assembly was furnace brazed in the same condition described before.

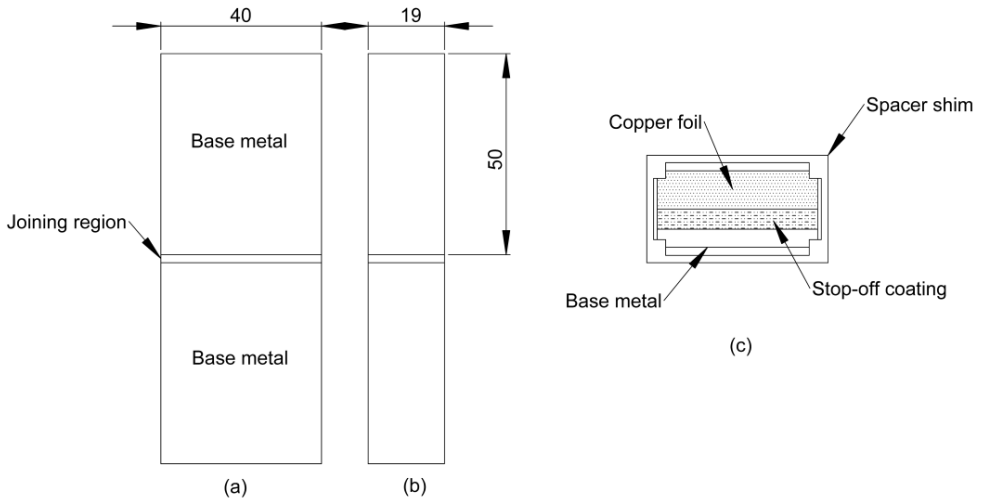

Figure 3-15- Brazing assembly (a) front view, (b) side view, (c) joining region top view (dimensions in mm)

The brazed block was cut and machined into the fracture specimens shown in Figure 3-16. The specimen dimensions were selected according to the ASTM E1820 recommendation and the ratio of the initial crack length to the specimen width (a/W) is set equal to 0.5 [93].

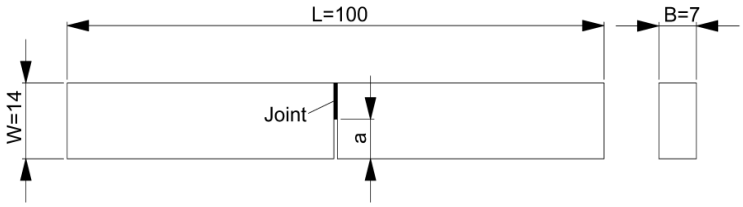

Figure 3-16- Fracture specimen geometry with the crack length *a* (dimensions in mm)

Four-point bending and tensile quasi-static fracture tests were performed on the SENB and SENT brazed specimens, respectively. The tests were conducted

under a displacement controlled condition with a rate of 0.03mm/s. Geometries and loading configurations of these two sets of specimens are shown in Figure 3-17 and Figure 3-18. In the four-point bend test, inner and outer loading spans were gripped into the jigs of a servo-hydraulic Instron tensile machine. The SENT specimens were tested with the clamping distance of 60 mm. Load and cross-head positions were recorded during the test. The CMOD was measured by the use of a clip-gage attached to the knife edges which were screwed to the specimens within a gage length of 8 mm.

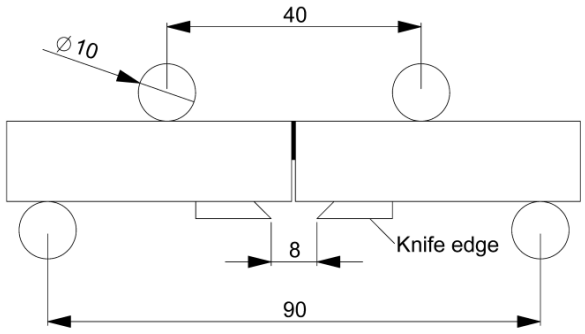

Figure 3-17- SENB specimen under four-point bend loading (dimensions in mm)

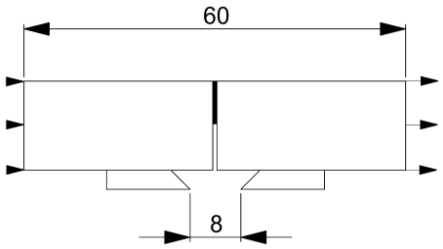

Figure 3-18- SENT specimen under tensile loading (dimensions in mm)

The crack length was monitored by a CCD video-microscope camera during the fracture test. Lab View software was programmed to capture images of the crack tip at every 0.01 s time interval. The load output signal was also recorded simultaneously to identify the corresponding applied load for which the crack tip image was captured. Figure 3-19 shows the schematic of the fracture test and image capturing set-up.

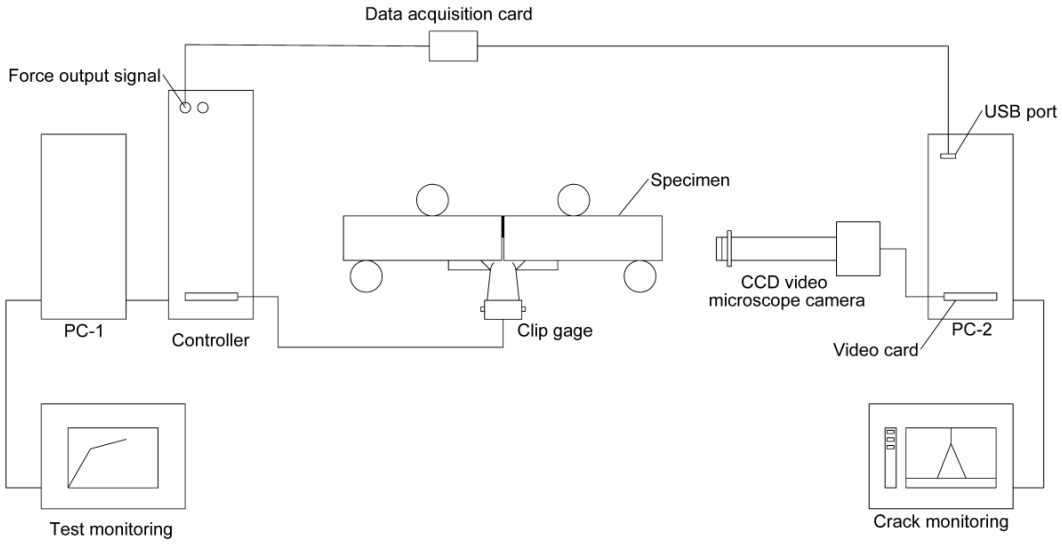

Figure 3-19- Schematic of the fracture test and image capturing set-up

3.2.2.2 Results and discussion

Figure 3-20 shows the optical micrograph of the fracture specimen at the produced starter crack. The crack root radius, which was measured less than 1 μm

for all the specimens, is sharp enough in order to not affect the fracture test results [94].

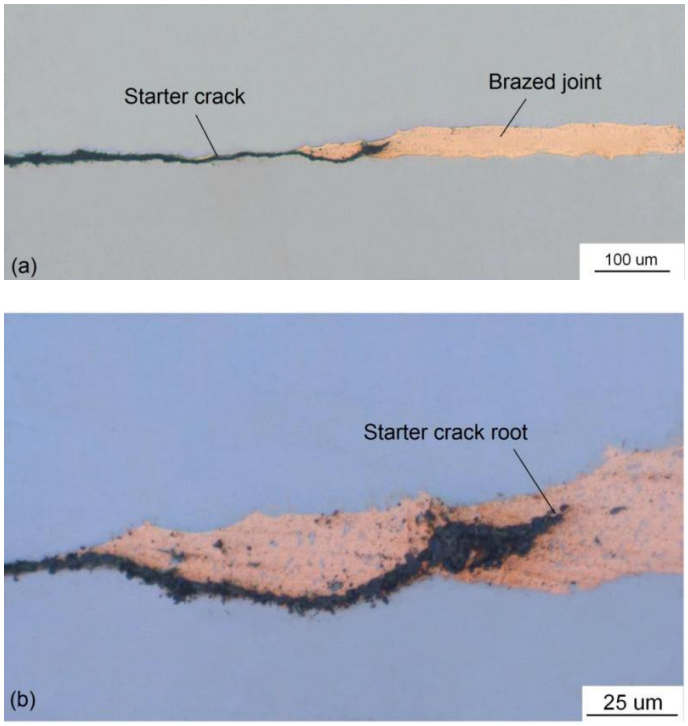

Figure 3-20- Micrograph of the starter crack taken by an optical microscope (a) 100x, (b) 500x

From the quasi-static fracture toughness tests performed on the two types of SENB and SENT specimens, load versus CMOD curves were plotted in Figure 3-21. Behavior of all of the tested specimens in each test group is in good agreement which validates the test repeatability and accuracy.

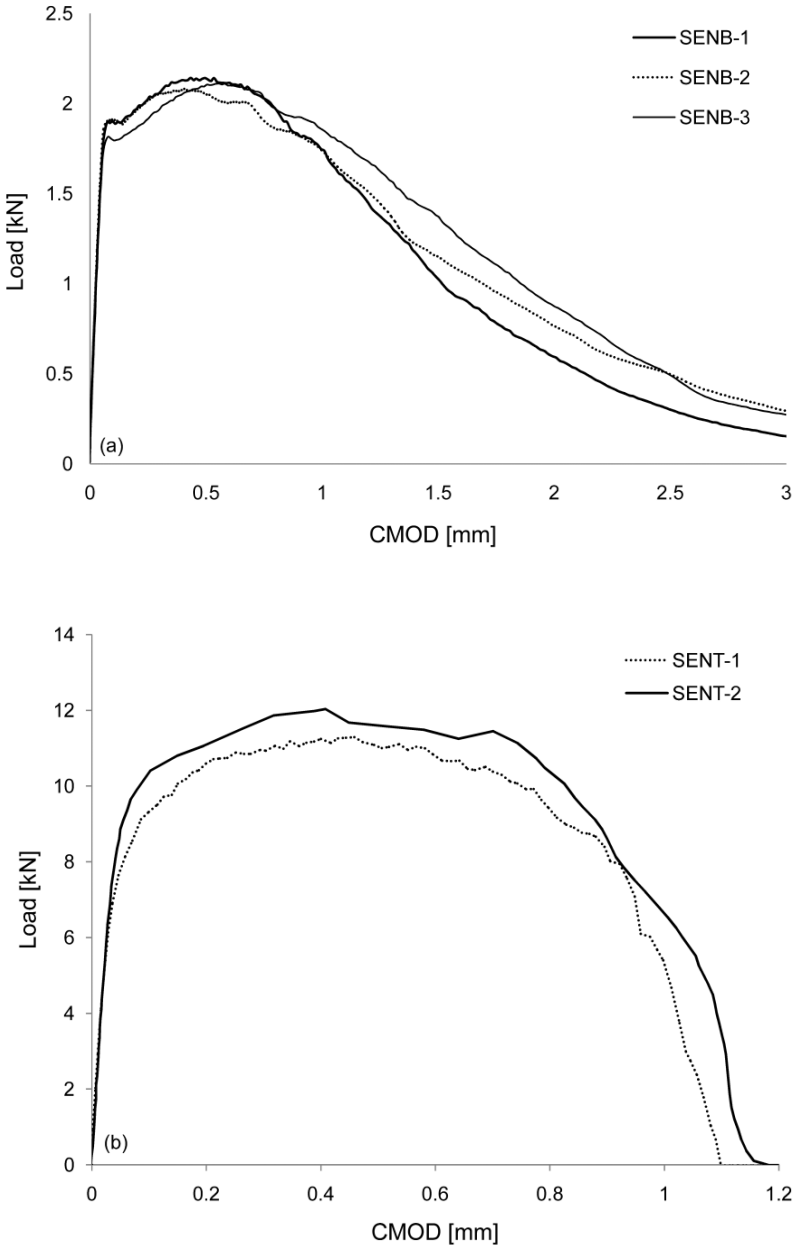

Figure 3-21- Load-CMOD curves recorded for (a) SENB and (b) SENT specimens

The optical micrograph of the fracture specimen at the crack tip region is shown in Figure 3-22. The crack has propagated through the copper interlayer and a large scale plastic deformation is observed in the base metal region.

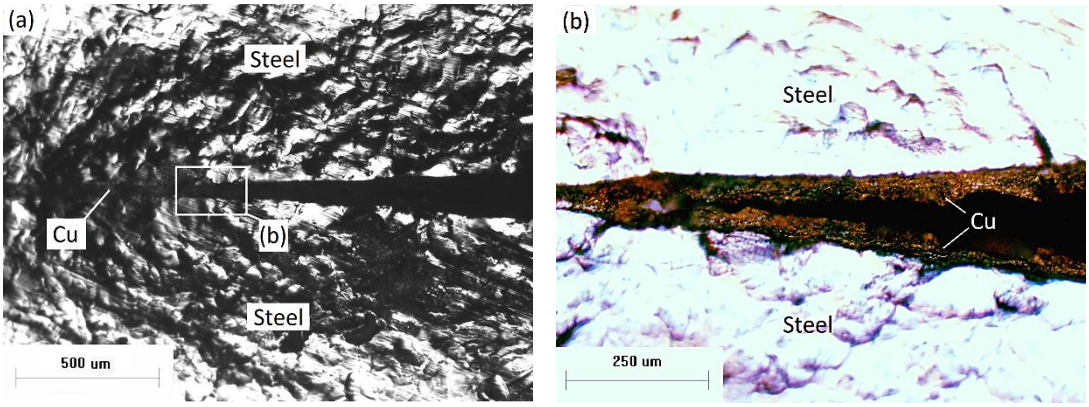

Figure 3-22- Optical micrograph of the fracture specimen at crack tip region (a) 50x, (b) 100x

The images taken from the crack during the fracture tests determine the corresponding critical load levels, P_c, at which the crack extension has initiated for each tested specimen. The critical loads and maximum attainable loads, P_{max}, are listed in Table 3-6.

The energy needed for crack propagation per unit area of the crack advance is called the energy release rate, J. The critical amount of the energy release rate at initiation of crack extension is the fracture toughness of a material, J_c . ASTM E1820 standard for the fracture toughness testing of metallic materials provides equations needed for calculation of the energy release rate from a fracture test results

[93]. The values of the load and CMOD which are experimentally measured for each increment of the crack advance (i) are used for the calculations. The elastic and plastic components of the energy release rate are calculated from [93]:

$$J_{el(i+1)} = \frac{K_{(i+1)}^2}{E} \tag{3-4}$$

$$J_{pl(i+1)} = \left(J_{pl(i)} + \frac{\eta_{CMOD}^i}{b_i B} A_{Vpl}^{i+1,i}\right)\left(1 - \frac{\gamma_{CMOD}^i}{b_i}(a_{i+1} - a_i)\right) \tag{3-5}$$

In equation (3-4) the stress intensity factor, $K_{(i+1)}$, is defined as:

$$K_c = \frac{P_c}{BW^{\frac{1}{2}}} f(\frac{a}{W}) \tag{3-6}$$

where W and B are the specimen width and thickness, respectively. Furthermore, a is the crack length and $f\left(\frac{a}{W}\right)$ is a dimensionless weight function for the SENB and SENT specimens defined by equations (3-7) and (3-8), respectively [95].

$$f\left(\frac{a}{W}\right) = \frac{3\frac{(S_{outer} - S_{inner})}{W}(\frac{a}{W})^{1/2}\left[1.99 - \left(\frac{a}{W}\right)\left(1 - \frac{a}{W}\right)\left(2.15 - 3.93\left(\frac{a}{W}\right) + 2.7\left(\frac{a}{W}\right)^2\right)\right]}{2\left(1 + 2\frac{a}{W}\right)\left(1 - \frac{a}{W}\right)^{3/2}} \tag{3-7}$$

$$f\left(\frac{a}{w}\right) = \frac{\sqrt{2tan\frac{\pi a}{2W}}}{cos\frac{\pi a}{2W}}\left[0.752 + 2.02\left(\frac{a}{W}\right) + 0.37\left(1 - sin\frac{\pi a}{2W}\right)^3\right] \tag{3-8}$$

where S_{outer} and S_{inner} are the outer and inner loading spans for the four-point bend test, respectively.

In equation (3-5), b is the ligament length, and $A_{Vpl}^{i+1,i}$ represents the increment of the plastic component of the area under load-CMOD curve, Figure 3-23. Furthermore, η_{CMOD} and γ_{CMOD} are the geometry factors defined according to the type of the specimens [93].

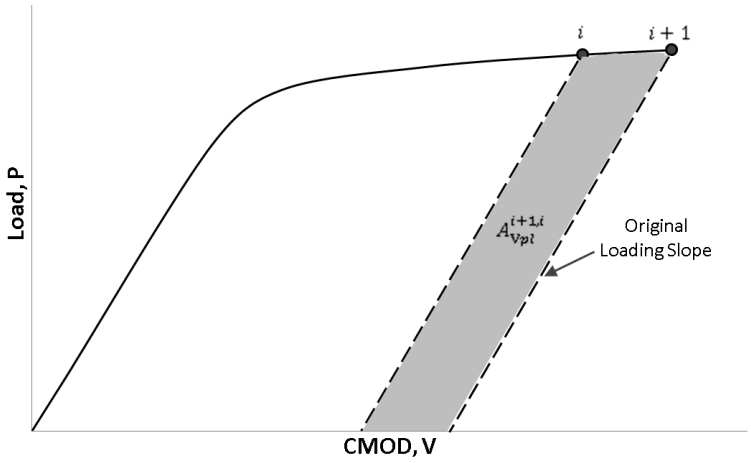

Figure 3-23- Calculation of $A_{Vpl}^{i+1,i}$ from load-displacement curve

Table 3-6 Critical load, maximum load and fracture toughness of SENB and SENT specimens

Specimen type	Test	P_c [kN]	P_{max} [kN]	J_c [kJ/m^2]
SENB	4-point bend	1.89	2.14	10.63
SENT	Tension	10.87	11.48	133.45

Crack resistance curves (J-R) for the SENB and SENT specimens are plotted in Figure 3-24. In both types of specimens, crack extension was initiated shortly before the applied load had reached its maximum value. For the SENB specimens the crack resistance is initially increasing and then reaches a flat plateau; however, for the SENT specimens a rising resistance curve is observed as the crack propagates.

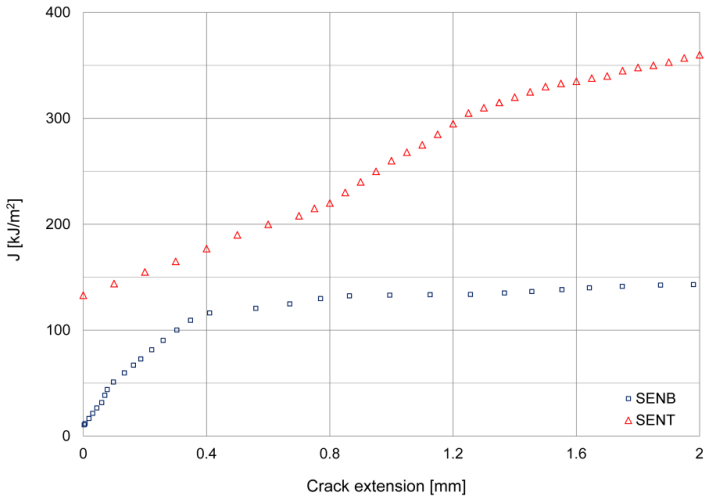

Figure 3-24- Crack resistance curves for the SENB and SENT specimens

The difference observed in crack resistance behavior of the two specimens is related to the crack tip plastic zone size which strongly depends on the geometrical constraint at the crack tip region [96]. The SENB specimens have a high crack tip geometrical constraint which causes a triaxial state of stress resulting in less plasticity induced at the crack tip region. Whereas, the SENT specimens with a

lower level of stress triaxiality have a large developing crack tip plastic zone and show a noticeable toughening during tearing process [28]. As a result, using the joint fracture toughness obtained from a SENB specimen leads to an excessive conservatism in engineering designs.

3.2.3 Failure mechanisms

The fracture surfaces of the tested specimens that failed under tensile and shear stresses were examined by SEM in secondary electron image (SEI) mode. The SEM images reveal that failure has occurred at the joint filler metal region, and no delamination is observed along the filler and base metal interface. For all of the brazed specimens failed under tensile stresses, a mixed fracture mechanism is identified on the images. For instance, the fracture surface image of one of the tensile specimens is shown in Figure 3-25 (a). Dimples on the fracture surface indicate ductile micromechanism of void nucleation, growth and coalescence [97] and are magnified in Figure 3-25 (b). Dendritic failure is the second failure mechanism observed on the SEM images of the specimens under tensile stresses. Figure 3-25 (c) shows dendrites on high magnification, and the dendrite arms are magnified in Figure 3-25 (d).

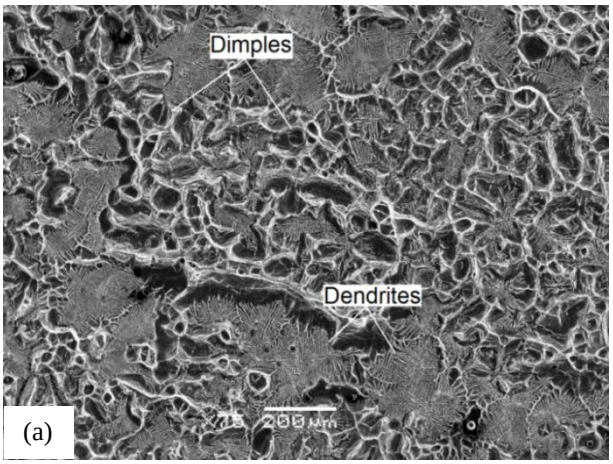

(a)

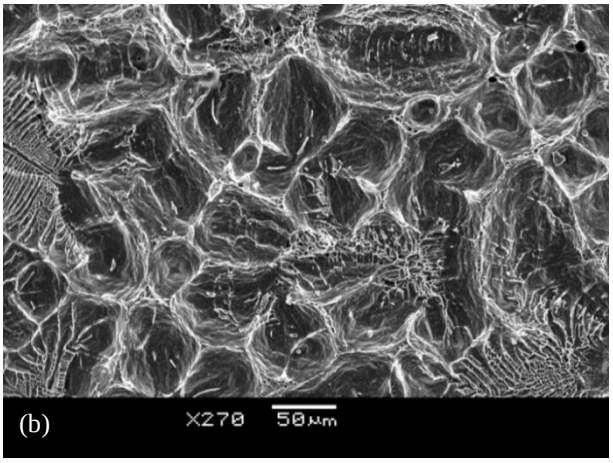

(b)

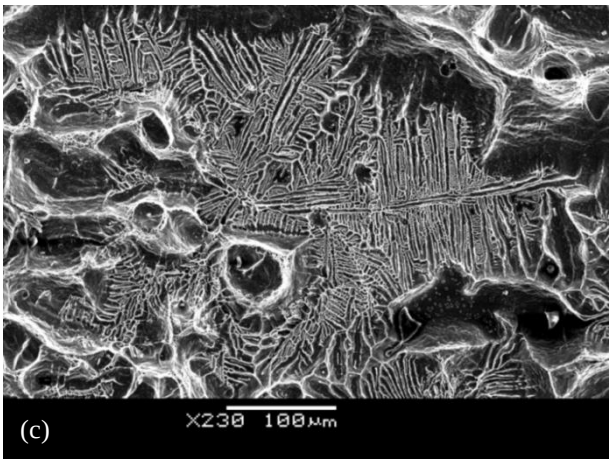

(c)

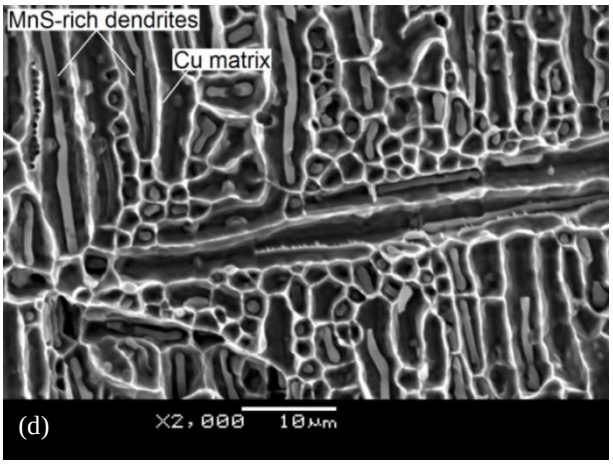

Figure 3-25- SEM-SEI images of the tensile specimen: (a) mixed mode fracture mechanism, (b) spherical dimples, (c) dendrites (X230), (d) dendrites in the copper matrix (X2,000)

The EDS chemical analysis was performed to verify the element composition of the fracture surface corresponding to the different failure mechanisms. The failed regions with the dimple rupture mechanism consist of Fe and Cu elements. The previously identified Fe-rich dendrites in the Cu matrix serve as the void nucleation sites which lead to the dimple rupture. Microvoids formed during solidification grow, coalesce and cause the dimple rupture as well. The failed regions with the dendritic failure mechanism contain Mn and S elements. This indicates that the MnS-rich dendrites which were observed earlier on the joint cross section cause dendritic failure mechanism for the specimens failed under tensile stresses. This brittle dendritic phase, as the joint weakest region, is the site of damage initiation and significantly decreases the joint strength and ductility.

Figure 3-26 shows a SEM image of the torsion specimen. A ductile failure mechanism is identified by the dimples elongated in the shear direction. The MnS-rich dendrites, identified on the fracture surface, serve as the source of void nucleation which leads to the dimple rupture under shear stresses. Moreover, the Fe-rich dendrites in the copper matrix and microvoids are the other sources of the dimple rupture in the torsion specimen.

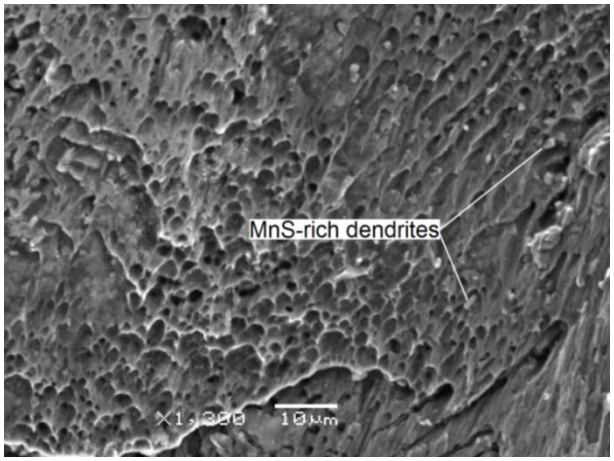

Figure 3-26- Elongated dimples on SEM-SEI image of the torsion specimen (X1300)

3.3 Summary

In this chapter the tensile, shear and biaxial strengths of low carbon steel brazed joints with copper filler metal are experimentally evaluated and numerically simulated by ABAQUS 6.7 software. The resistance of the joint against crack

propagation is evaluated by fracture toughness testing on SENB and SENT specimens. SEM images of the joint fracture surfaces revealed the corresponding failure mechanisms under tensile and shear stresses. The following conclusions are drawn from this study:

1. Images of the brazed joint etched cross section taken by SEM-BEI technique and the corresponding chemical EDS analysis revealed the joint microstructure and element composition on different joint regions. The MnS and Fe-rich dendrites identified in the brazed filler metal region serve as the damage initiation locations in the mechanical testing.

2. The tensile strengths of the two brazed joints with different base metals of A36 and A108 low carbon steels were measured equal to 330 MPa and 417 MPa, respectively. It was found that a higher yield limit of the base metal enhances the joint tensile strength by delaying the extensive plastic deformation of the filler metal to a higher load level. The shear strength of the brazed joint with A36 steel base metal was measured equal to 246 MPa from the torsion test performed on thin-walled tubular specimens. Biaxial strength and deformation behavior of the brazed joints were also evaluated by tension-torsion tests for different extension to twist angle ratios. A mixed

mode power law failure criterion with the exponent equal to 1.85 was best fitted to the experimental results.

3. Applying the experimentally measured deformations of the tensile and torsion specimens into the FE model, the joint strengths were well estimated. Furthermore, the numerical results obtained from the FE simulation of the biaxial tension-torsion tests were in good agreement with the power law failure criterion fitted to the experimental data.

4. Fracture toughness tests were performed on the SENB and SENT specimens. The load-CMOD curves coincided well for each type of the tested specimens. The average fracture toughness was calculated to be 10.63 kJ/m^2 and 133.45 kJ/m^2 for the SENB and SENT specimens, respectively. Crack resistance curves for the two different tested specimens showed dependency on the loading configuration. Higher geometrical crack tip constraint effect of the SENB specimens decreases the joint toughness, significantly. However, the growing crack tip plastic zone of the SENT specimens leads to a more ductile behavior which was observed from its corresponding resistance curve. Consequently, using the fracture toughness obtained from a SENB specimen leads to an excessive conservatism in engineering designs.

5. SEM-SEI images showed that failure happened at the joint filler metal region. Two different failure mechanisms of dimple rupture and dendritic failure were observed on the fracture surfaces of the specimens failed under tensile stresses. The EDS analysis revealed that the MnS-rich dendrites are the sites of dendritic failure, while the finer Fe-rich dendrites and microvoids cause the dimple rupture in the tensile specimens. The SEM image of the torsion specimen showed the ductile dimple rupture mechanism which was initiated at the dendrites and microvoids.

Chapter 4

Cohesive Zone Modeling of Ductile Tearing Process in Brazed Joints

The ductile tearing process in low carbon steel brazed joints with copper filler metal is studied using the CZM. The cohesive energy of the brazed joints is obtained from the four-point bend fracture test results provided in Chapter 3. Based on the obtained cohesive energy parameter, the fracture test is simulated using ABAQUS 6.7. A unique value for the joint cohesive strength is determined by best fitting the FE results to the experimental load-CMOD curve. The predictability of

the characterized CZM is explored by FE modeling of the tensile test performed on the SENT specimens. The load-CMOD curve obtained from the FE modeling conforms to the corresponding experimental results. The good agreement between the FE simulation results and the experimental data confirms the applicability of the CZM for fracture analysis of the brazed joints.

4.1 Evaluation of the cohesive energy

The cohesive energy is the work required for complete material separation per unit area of the crack advance [48]. This quantity can be expressed in terms of the critical value of the energy release rate in a pre-cracked body. In this section the concept of the energy release rate is introduced first and the value of the brazed joint cohesive energy is obtained based the fracture test results presented in Chapter 3.

4.1.1 Energy release rate

The energy release rate is defined as the energy dissipated for an increment of crack extension as follows:

$$J = -\frac{d\Pi}{dA} \tag{4-1}$$

where Π and A are the potential energy and the crack area, respectively. The potential energy is defined by the strain energy, U, stored in the body and the work, F, done by an external load, P , as follows [95]:

$$\Pi = U - F \tag{4-2}$$

Substituting equation (4-2) into equation (4-1), the energy release rate can be described in terms of load, P, and displacement, Δ, applied to a plate with a unit thickness, as illustrated in Figure 4-1 [95]:

$$J = \int_0^P \left(\frac{\partial \Delta}{\partial a}\right)_P dP \tag{4-3}$$

or

$$J = -\int_0^\Delta \left(\frac{\partial P}{\partial a}\right)_\Delta d\Delta \tag{4-4}$$

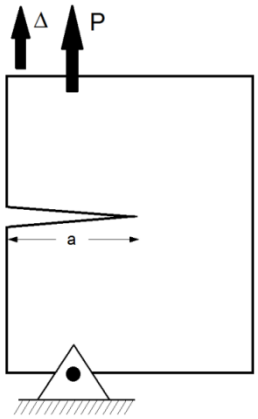

Figure 4-1- A plate with a crack length *a* under the applied load *P*

The crack starts propagation when the energy release rate reaches its critical value, J_c, known as the fracture energy of a material. In the case of brittle fracture, the critical energy release rate, denoted by G_c, consists of the material surface energy, γ_s, and its accompanying plastic work at small-scale vicinity of the crack tip for the unit area of the surface created, γ_p, as follows [95]:

$$G_c = 2(\gamma_s + \gamma_p) \tag{4-5}$$

However, in ductile fracture the critical energy release rate also includes large-scale plastic dissipations around the crack tip region. In this case the energy release rate is decomposed into two parts: the elastic component, J_{el}, which is the energy needed for material separation per unit area of the crack advance and the plastic component, J_{pl}, which is the energy dissipated per unit area of the crack advance due to large-scale plasticity around the crack tip region [85,95,98-100]. In order to obtain the components of the energy release rate, the applied displacement, Δ, is decomposed into its elastic and plastic parts as follows:

$$\Delta = \Delta_{el} + \Delta_{pl} \tag{4-6}$$

Substituting equation (4-6) into equation (4-3), the elastic and plastic components of the energy release rate are obtained as below:

$$J_{el} = \frac{K_I^2}{\acute{E}} \tag{4-7}$$

$$J_{pl} = \int_0^P \left(\frac{\partial \Delta_{pl}}{\partial a}\right)_P dP \tag{4-8}$$

where $\acute{E} = E$ for plane stress and $\acute{E} = E/(1-\nu^2)$ for plane strain conditions [95].

ASTM E1820 standard [93] provides the incremental forms of the equations (4-7) and (4-8) for calculation of the energy release rate from a fracture test results. Based on the incremental relations, the brazed joints critical energy release rate and the corresponding crack resistance curve were obtained in Chapter 3.

4.1.2 Cohesive energy of the brazed joints

The cohesive energy is the work required for complete material separation per unit area of the crack advance [48]. In other words, the energy dissipated for material debonding within the immediate vicinity of the crack tip is defined as the cohesive energy of a material. In brittle fracture, the critical energy release rate is considered as the cohesive energy [53,85,95]. As discussed in the previous section, in ductile fracture the energy release rate includes large-scale plastic dissipations around the crack tip region, as well. Decomposition of the energy release rate into the elastic, J^{el}, and plastic, J^{pl}, components decouples the work required for material

separation from the energy dissipation due to large-scale plasticity around the crack tip region [53,60,95,98-100]. Hence, the elastic component of the critical energy release rate, J_C^{el}, which is the energy needed for material debonding per unit area of the crack advance, is considered as the cohesive energy of a ductile material [53,95].

The value of the brazed joint cohesive energy is obtained from the results of the quasi-static fracture test performed on the SENB specimens, which were presented in Chapter 3. The values of J_C and its corresponding elastic and plastic components in the plane stress and plane strain conditions are listed in Table 4-1. As discussed above, the plastic component of the energy release rate corresponds to the base metal plastic dissipation around the crack tip, while the elastic part of the critical energy release rate represents the brazed joint cohesive energy.

Table 4-1 Components of critical energy release rate for the SENB

Stress state	$\boldsymbol{J_C^{el}}$ $[\frac{\boldsymbol{kJ}}{\boldsymbol{m^2}}]$	$\boldsymbol{J_C^{pl}}$ $[\frac{\boldsymbol{kJ}}{\boldsymbol{m^2}}]$	$\boldsymbol{J_C}$ $[\frac{\boldsymbol{kJ}}{\boldsymbol{m^2}}]$
Plane stress	4.76	5.87	10.63
Plane strain	4.33	5.87	10.20

The obtained values of the brazed joint cohesive energy will be used in the cohesive zone modeling of the fracture test to characterize the cohesive strength in the following section.

4.2 FE modeling of ductile tearing process in the SENB specimens and evaluation of the cohesive strength

Ductile tearing process in the SENB brazed specimens under the four-point bend quasi-static fracture test is modeled using ABAQUS 6.7 [4]. The built-in cohesive elements (COH2D4) with 4 nodes and 2 integration points are used in the simulation. The schematic of the two dimensional cohesive element is illustrated in Figure 4-2. The element has two degrees of freedom of displacement in normal and shear directions per each node. The thickness orientation of the element is defined such that it is perpendicular to the top and bottom faces. These two opposite faces are separated by a defined initial constitutive thickness. The separation in the cohesive element is simply measured by relative displacement of these two opposite faces [4].

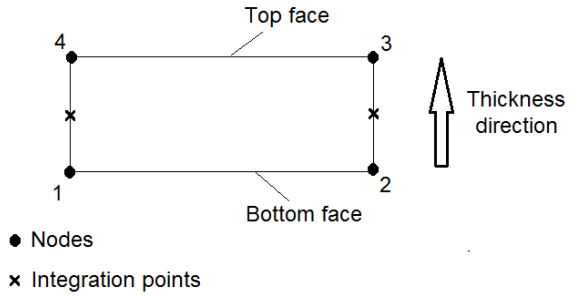

Figure 4-2- Schematic of a 2D cohesive element (COH2D4)

The brazed joint interlayer was meshed by a single row of the two dimensional cohesive elements oriented in the joint thickness direction. The initial constitutive thickness of the cohesive elements is set equal to the joint clearance of 0.05 mm. A bilinear traction-separation law, shown in Figure 4-3, is used as the constitutive model of the cohesive elements. The relation between the CZM parameters of the cohesive energy, Γ, and the cohesive strength, $\sigma_{max,0}$, is given by equation (4-9), as below:

$$\Gamma = \frac{1}{2}\sigma_{max,0}\delta_C \tag{4-9}$$

where δ_C represents the separation at failure [85].

The stiffness of the cohesive elements, which is equal to the slope of the linear part of the traction-separation law, is defined by [4]:

$$k = \frac{E}{t} \tag{4-10}$$

where E and t represent Young's modulus of the joint copper filler metal, i.e., 82 GPa, and the joint clearance, i.e., 0.05 mm, respectively.

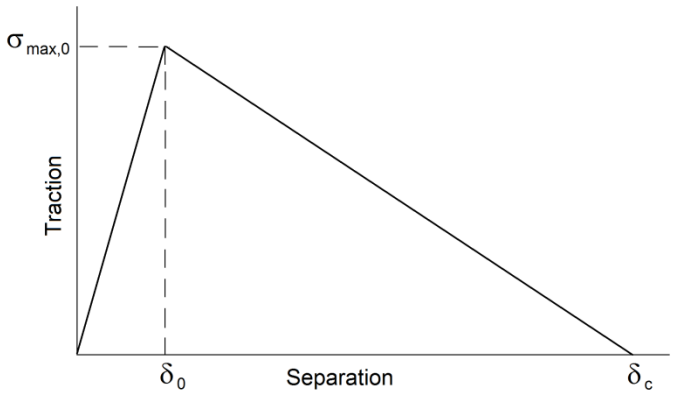

Figure 4-3- The bilinear traction-separation law used for the simulation

The surrounding base metal regions are meshed by 4-node quadrilateral bilinear elements (CPS4R) [4]. The same material properties are defined for the low carbon steel (ASTM-A36) base metal as presented in Chapter 3.

The FE model of the SENB specimen and its applied boundary conditions are shown in Figure 4-4 (a). Fixed displacement boundary conditions are applied to the top rigid rollers and the bottom rigid rollers are displaced upward. Surface to surface contact is used between the rollers and specimen with a refined mesh at the contact regions. The CMOD is obtained from the x-displacement of the knife edges included in the FE model. The mesh patterns around the crack path and at the tip of the crack are illustrated in Figure 4-4 (b) and (c), respectively.

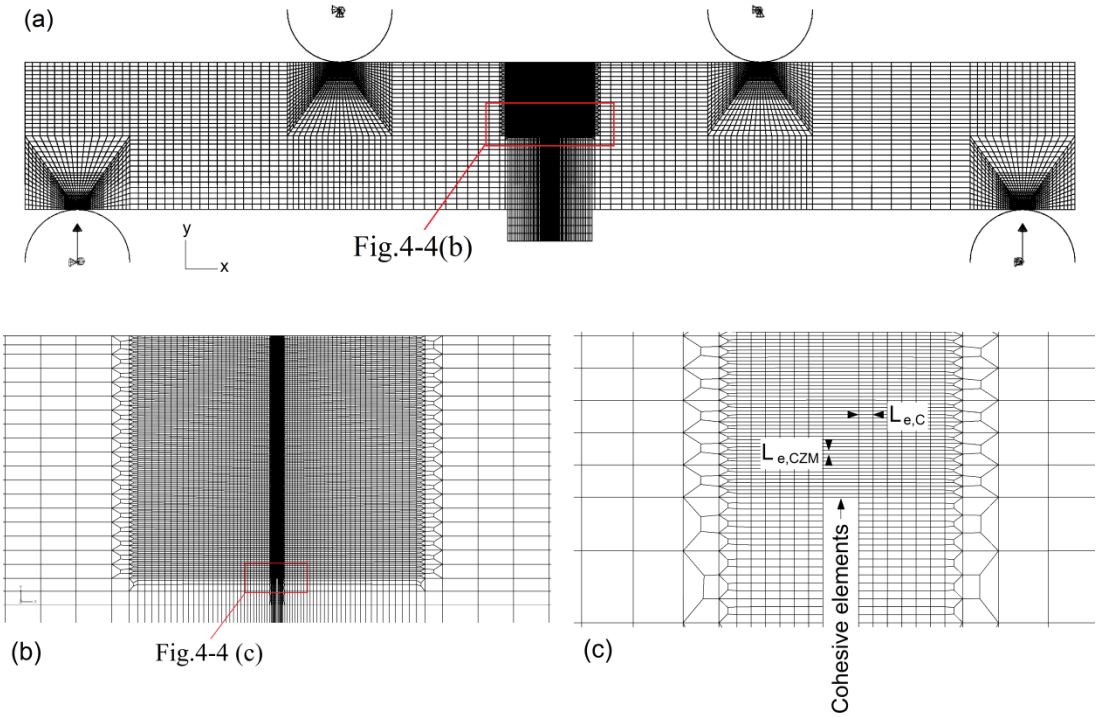

Figure 4-4- (a) FE model of the SENB specimens and boundary conditions, (b) mesh pattern around the crack path, (c) mesh pattern at the crack tip

A mesh convergence study is carried out to obtain a proper cohesive element length, $L_{e,CZM}$. The initial cohesive element length of 0.02 mm is selected first and the number of elements is doubled in the subsequent mesh convergence analyses. The obtained numerical CMOD-crack extension curves for different cohesive element lengths are plotted in Figure 4-5. The numerical results are converged for the cohesive element length of 0.005 mm which is used in the FE simulations.

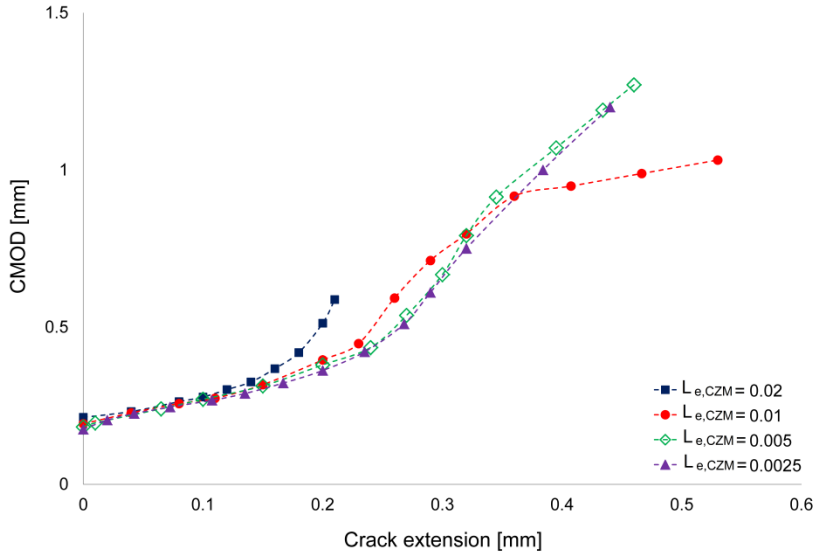

Figure 4-5- CMOD-crack extension curves for different cohesive element mesh sizes (in mm)

In order to capture the plastic deformation around the crack tip, the surrounding continuum elements should be sufficiently fine. An initial element length of 0.12 mm is selected for the continuum elements, $L_{e,C}$, and the number of elements is doubled in the subsequent FE analyses. The load-CMOD curves for different mesh sizes are presented and compared with the experimental one in Figure 4-6. The FE results are converged for the continuum element size of 0.02 mm which will be used in the FE simulations.

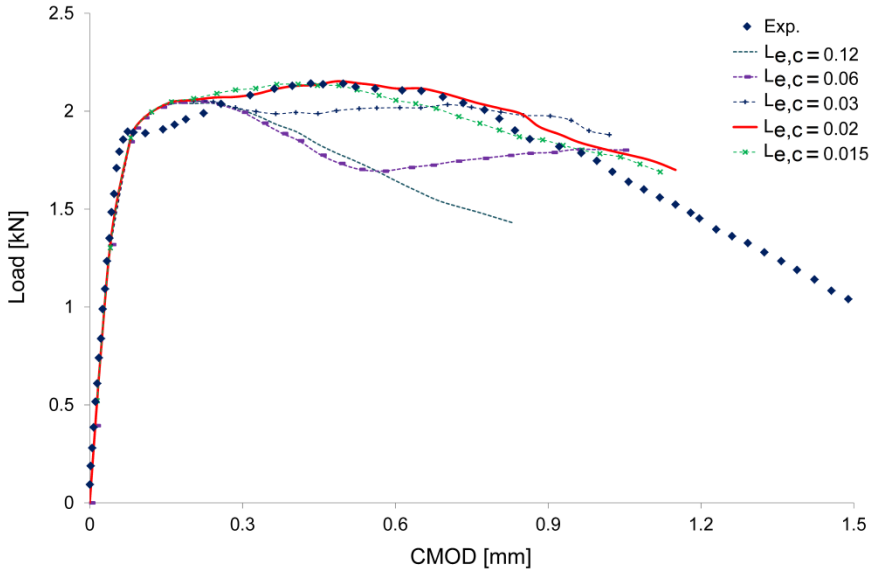

Figure 4-6- Load-CMOD curves for different continuum element mesh sizes (in mm)

The cohesive energy obtained in the previous section is assigned to the cohesive elements. Figure 4-7 shows the numerical load-CMOD curves which are plotted for different values of the cohesive strength in plane stress condition and compared with the experimental one. It is shown that the cohesive strength of 400 MPa best fits the corresponding experimental curve. Variations of the predicted loads with respect to different cohesive strength values are listed in Table 4-2. Results obtained indicate that the maximum attainable load shows more sensitivity than the critical load with respect to the variations of the cohesive strength parameter.

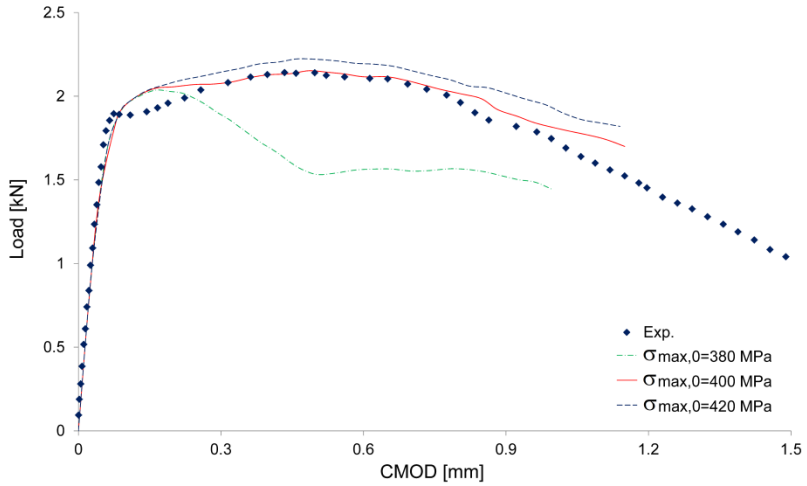

Figure 4-7- Experimental and numerical load-CMOD curves for different values of $\sigma_{max,0}$

Table 4-2 Variations of the critical and maximum loads respect to the cohesive strength

$\sigma_{max,0}$ [MPa]	Γ [$\frac{kJ}{m^2}$]	δ_f [mm]	P_C [kN]	P_{max} [kN]
380	4.76	0.0250	2.03	2.04
400	4.76	0.0238	2.05	2.15
420	4.76	0.0226	2.07	2.22

Figure 4-8 shows the contours of traction and stress field perpendicular to the crack faces at different stages of the crack propagation. The traction continuously increases over increasing the separation along the interlayer until the damage initiates (Figure 4-8 (b,c)). Further increase in the separation results in the traction decrease in the damaged cohesive elements and the crack initiates when the first

cohesive element is fully damaged (Figure 4-8 (d)). The elements which are fully damaged are removed subsequently to simulate crack propagation (Figure 4-8 (e)).

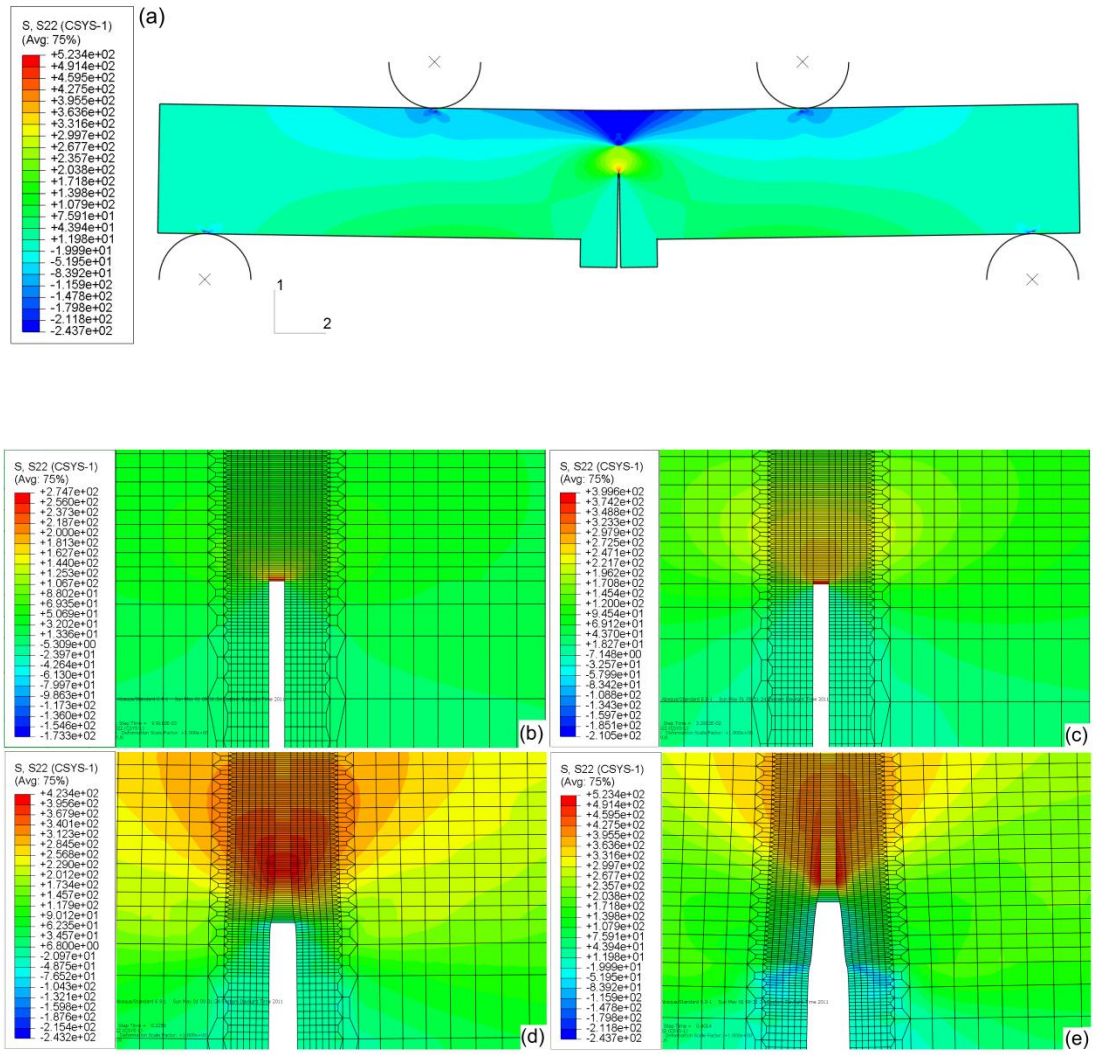

Figure 4-8- Stress field, S22, perpendicular to crack faces (a) in the whole model at crack initiation, (b) before damage initiation, (c) at the onset of damage initiation, (d) at the onset of crack initiation, (e) during crack propagation

To better illustrate the crack growth process in the joint using the CZM, distributions of the traction along the interlayer at different damage levels are plotted in Figure 4-9. This figure shows the gradual decrease in the traction for the damaged elements which indicates the loss of element load carrying capacity. The traction reduces to zero for fully damaged cohesive elements to model crack propagation.

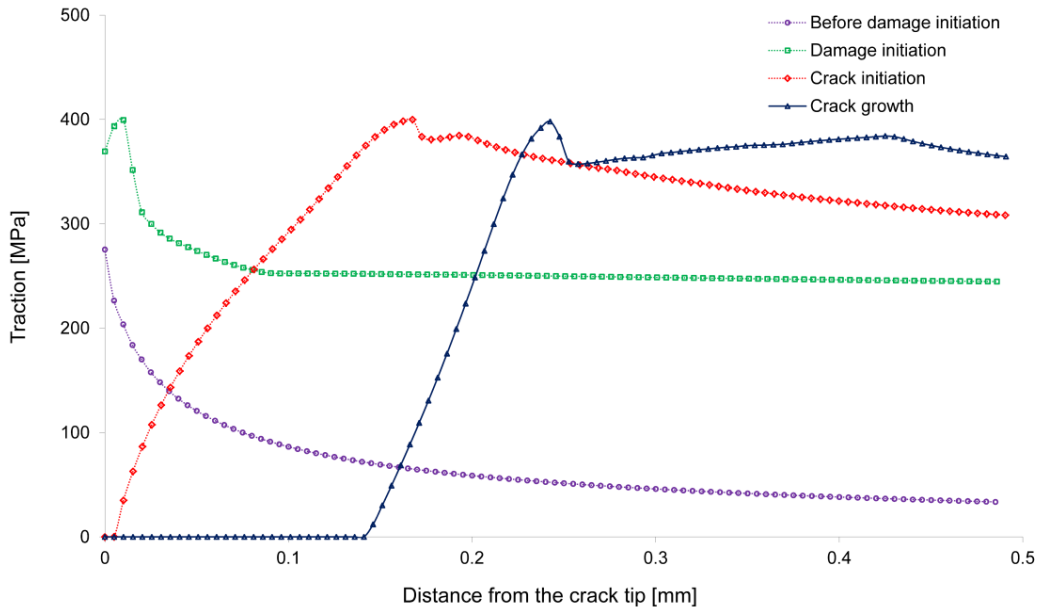

Figure 4-9- Traction distributions from the initial crack tip along interlayer at different damage levels

The load-CMOD curve obtained for the cohesive strength of 400 MPa in the plane strain condition is plotted and compared with the results in the plane stress condition, Figure 4-10. The results show that if a plane strain condition is assumed, the plastic deformation around the crack tip region is noticeably underestimated, and

is not consistent with the nature of this problem. Hence, the plane stress condition is suitable for two-dimensional crack growth modeling of the fracture specimens used in this study.

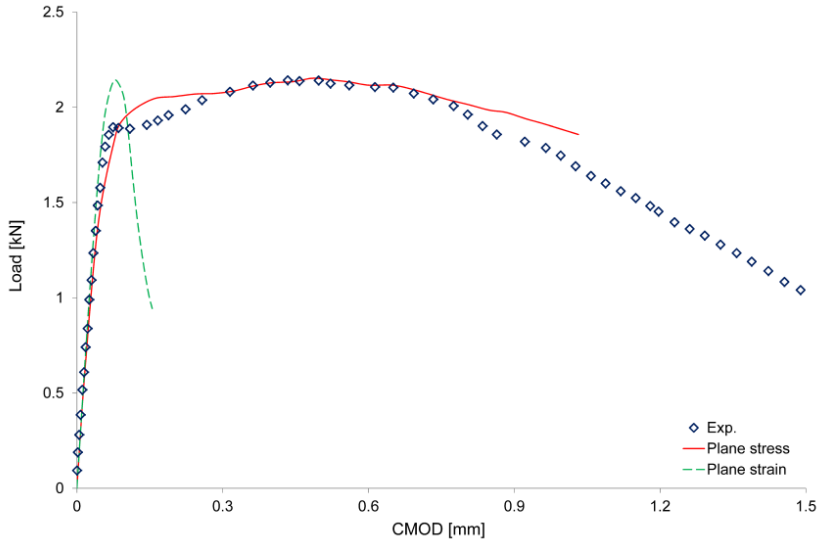

Figure 4-10- Experimental and numerical load-CMOD curves in plane stress and plane strain

4.3 Validation of the CZM

In order to explore the predictability of the CZM approach and validate the obtained cohesive zone parameters, the tension test performed on the SENT specimens is simulated. Figure 4-11 shows the FE model and the applied boundary conditions of the tension test. One end of the model is fixed and displacement in

extension direction is applied to the other end of the model. The same element sizes obtained for the modeling of the SENB specimen are used in this simulation.

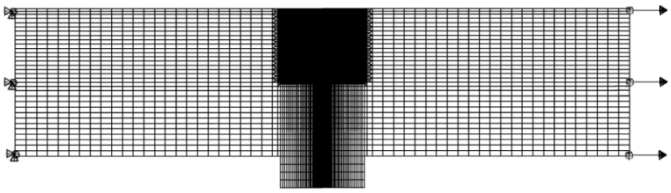

Figure 4-11- FE model of the SENT specimen and the applied boundary conditions

The load-CMOD curve obtained from the FE simulation is plotted over the experimental curve, as shown in Figure 4-12. It is observed that in the plane strain condition the maximum attainable load level is considerably underestimated. However, in the case of plane stress the maximum load and its corresponding CMOD are well predicted by the model.

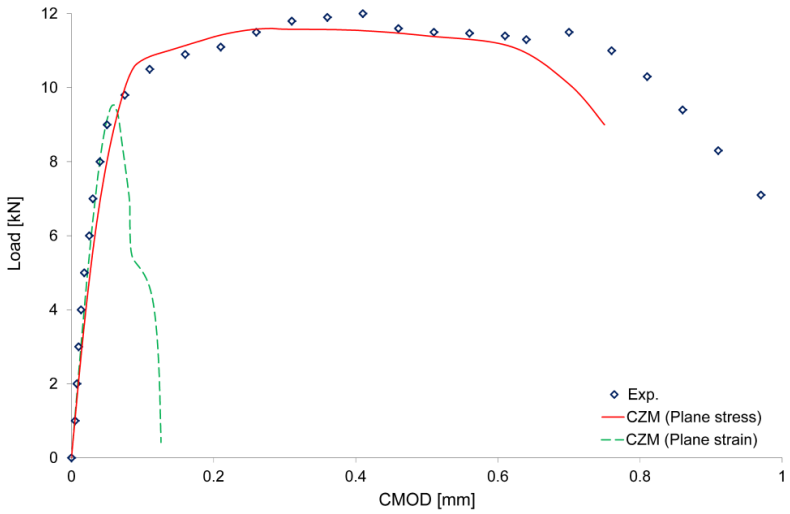

Figure 4-12- Experimental and numerical load-CMOD curves of the SENT specimen

The critical load at crack initiation and the maximum attainable load obtained from the simulations and the experiments for the SENB and SENT specimens are presented and compared in Table 4-3. The results show that the load levels for both types of the specimens are well estimated by the CZM.

Table 4-3 The critical and maximum loads obtained from the experiment and CZM

Specimen type	CZM		Experiment	
	P_C [kN]	P_{max} [kN]	P_C [kN]	P_{max} [kN]
SENB	2.05	2.15	1.89	2.14
SENT	10.74	11.60	11.01	11.81

Contours of the crack tip plastic strain in the SENB and SENT specimens at the onset of crack initiation, during crack propagation, and at the onset of failure are plotted in Figure 4-13. Under the tensile loading, two slip shear bands are formed and developed at a ±55° angle with respect to the loading axis. In bending, the slip bands form a fan-shaped curvature known as Prandtl slip fields [100].

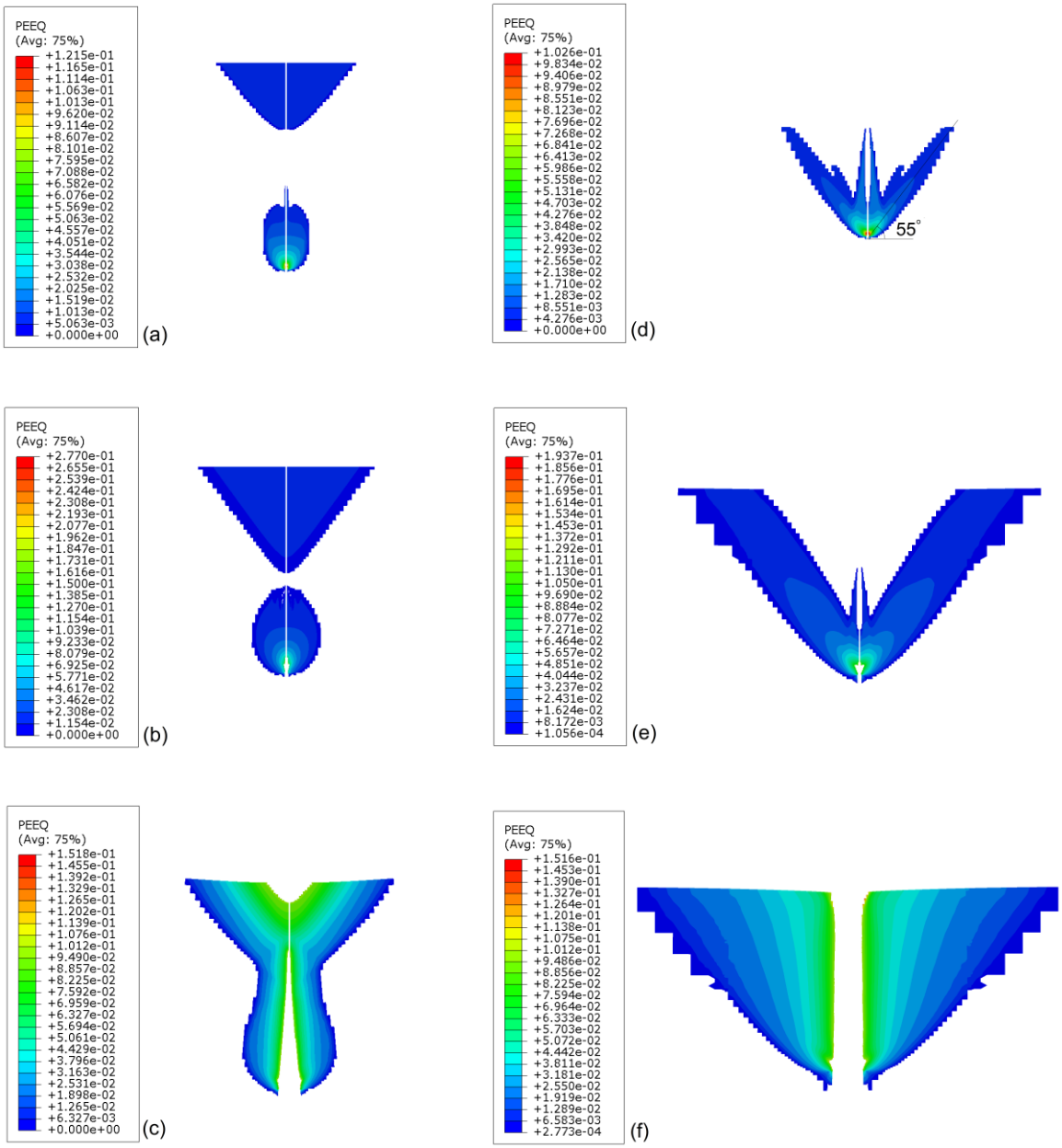

Figure 4-13- Crack tip plastic strain in the SENB at (a) crack initiation, (b) *a*=0.2 mm, (c) at failure, and in the SENT specimen at (d) crack initiation, (e) *a*=0.2 mm, (f) at failure

The width of the plastic zone with respect to the crack extension for the two types of fracture specimens is plotted in Figure 4-14. In the SENB specimen the size of the plastic zone gradually increases after crack initiation until a constant size is reached. However, in the SENT specimen the plastic zone size is larger than that of the SENB specimen and develops faster with respect to the crack extension. As shown in this figure, for both types of the specimens the load increases during the development of the plastic zone and reaches its maximum value once the plastic zone size stabilizes. Thereafter, the total energy required for crack propagation, i.e., the summation of the plastic dissipation energy and the cohesive energy, remains constant. As a result the external work of the applied displacement remains constant and the load drops to satisfy the energy balance.

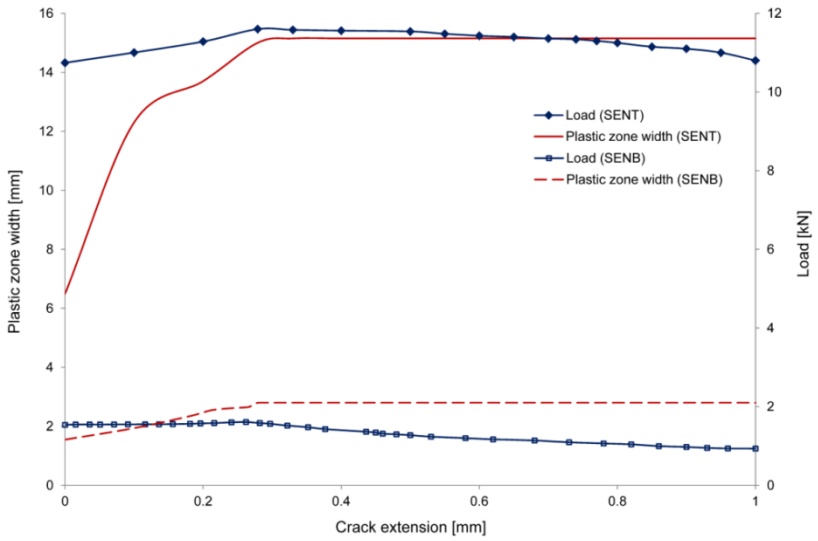

Figure 4-14- Load and crack tip plastic zone width with respect to the crack extension

The crack tip plastic zone size depends on the stress state which is indicated by the stress triaxiality factor (TF). A high level of stress triaxiality constrains the plastic flow at the crack tip region. The triaxiality factor is defined as the ratio of the hydrostatic part of the stress, σ_H, to the equivalent Mises stress [101]:

$$TF = \frac{\sigma_H}{\sigma_{Mises}} \tag{4-11}$$

Figure 4-15 shows the variations of the triaxiality factor plotted on a path from the initial crack tip location along the interface. The tensile part of crack tip stress triaxiality level in the SENB specimen is higher than that of the SENT specimen. Hence the plastic flow at the crack tip of the SENB specimen is more constrained and the corresponding plastic zone develops less than that of the SENT specimen [102].

The good agreement observed between the results of the tension test simulation and the experiment verifies the uniqueness of the obtained values for the CZM parameters. Moreover, the results show that using the CZM the crack tip stress triaxiality, which affects the shape and size of the plastic zone, is well captured. It is concluded that once the CZM is characterized for a brazed joint, the model is capable of the joint fracture analysis independent of geometry and loading configurations.

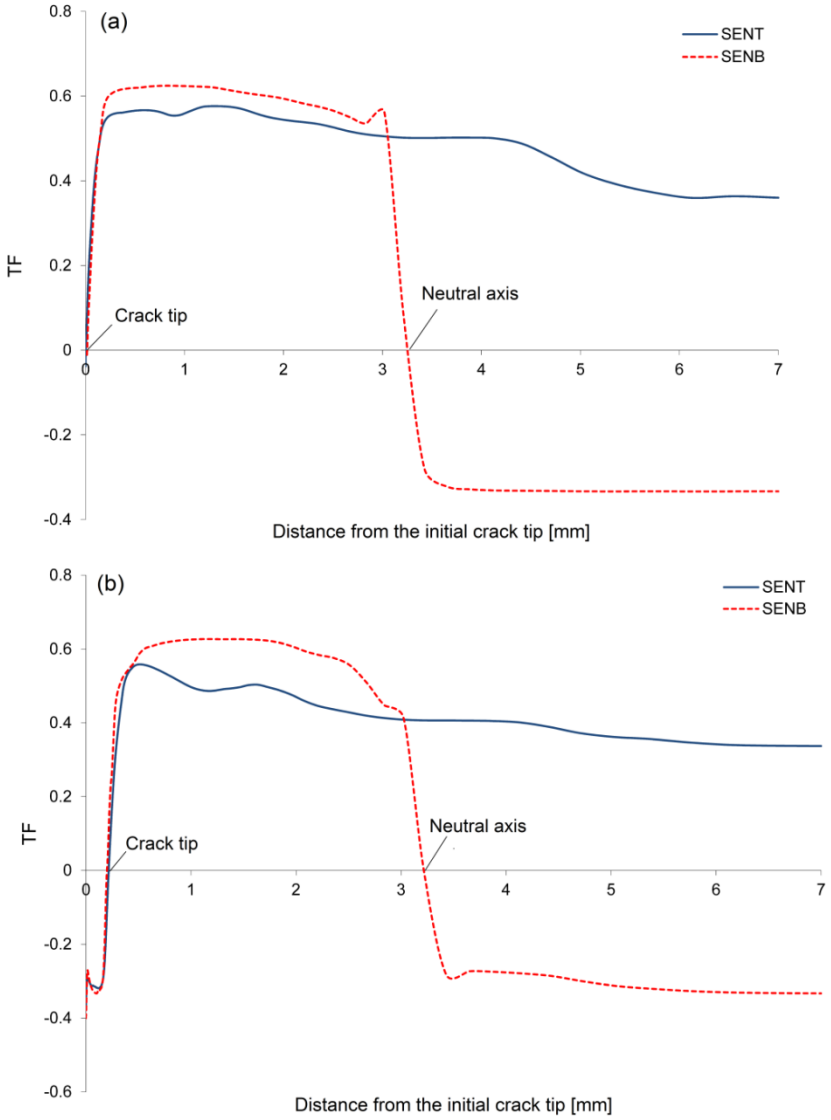

Figure 4-15- Triaxiality factor along the interface at (a) crack initiation, (b) a=0.2 mm

4.4 Summary

In this chapter, the bilinear CZM was successfully employed as a two-parameter fracture analysis tool to predict mode-I fracture and simulate the ductile tearing process in the brazed joints. Using the CZM, the energy needed for material debonding is decoupled from the large scale plastic work dissipated around the crack tip. Hence, the characterized CZM is capable of nonlinear fracture analysis of the steel/Cu/steel brazed joints independent of geometry and loading configurations.

The CZM parameters of the cohesive strength and the cohesive energy were characterized from the four-point bend fracture test results associated with the corresponding FE simulation. The predictability of the obtained CZM was investigated by the FE modeling of the tensile test performed on the SENT specimens. Following conclusions are drawn from this chapter:

1. The cohesive energy, as one of the CZM parameter, can directly be obtained from the fracture test results on the pre-cracked SENB specimens. Excluding the base metal plastic work dissipated around the crack tip, the elastic component of the critical energy release rate, i.e., the energy needed for material separation per unit area of the crack advance, is the joint cohesive energy in the ductile tearing process. The cohesive energy for the steel/Cu/steel

brazed joints is found to be equal to 4.76 kJ/m^2 and 4.33 kJ/m^2 in the plane stress and plane strain conditions, respectively.

2. The cohesive strength, as the second CZM parameter, was determined through relating the finite element modeling results to the experimental load-CMOD curve of the fracture test performed on the SENB specimens. Assuming the plane strain condition in the FE simulation, the plastic deformation around the crack tip region was noticeably underestimated which was not consistent with the nature of this problem. Hence the brazed joint cohesive strength was obtained equal to 400 MPa in the plane stress condition.

3. To validate the characterized CZM for the steel/Cu/steel brazed joints, the tensile test performed on the SENT specimens was modeled. The load-CMOD curve obtained from the FE model was in good agreement with the corresponding experimental results. The agreement between the FE simulation results and the experimental data showed the uniqueness of the obtained CZM parameters. This indicates that once the CZM parameters are determined for a brazed joint, the CZM is capable of predicting the joint fracture independent of geometry and loading configurations.

4. The effect of crack tip stress triaxiality on the plastic zone shape and size was well captured by the model. The low crack tip triaxiality factor in the SENT

specimens results in a more developed plastic zone than that of the SENB specimens. Furthermore, the simulation results showed that for both types of the specimens the load increases during the development of the plastic zone and reaches its maximum value once the plastic zone size stabilizes. Afterwards, the total energy required for the crack propagation remains constant and the load drops to satisfy the energy balance.

Chapter 5
Modeling Fatigue Crack Growth Using an Irreversible CZM

In this chapter, fatigue crack growth (FCG) in the brazed joints is modeled by an irreversible CZM. Strain-controlled fatigue tests are performed on the brazed specimens, and the corresponding results in terms of fatigue crack initiation and propagation lives are presented. A cyclic damage evolution law is coupled to the CZM to irreversibly account for the joint stiffness degradation over the number of cycles. The damage law parameters are calibrated based on analytical solutions and

the experimental fatigue crack growth data. The characterized irreversible CZM shows applicability to FCG life prediction of brazed joints.

5.1 Experiment

Uniaxial cyclic fatigue tests were performed on the flat dog-bone shaped brazed specimens shown in Figure 5-1. The tests were performed using servo hydraulic Instron tensile machine under fully reversed strain controlled condition. The wave form generator of the machine was set to produce sinusoidal wave with a frequency of 1 Hz.

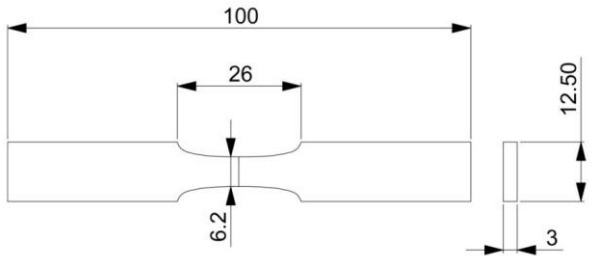

Figure 5-1- Dog-bone shaped specimen with a central joint for fatigue tests (dimensions in mm)

The specimens were cyclically tested under different strain amplitudes of 0.08%, 0.10%, 0.12%, 0.15%, and 0.20%, which were measured using a 10-mm gage length axial extensometer. A fatigue crack is initiated when the softening rate

of the load-cycle curve accelerates, as shown in Figure 5-2 [103]. The number of cycles at 50% load drop is taken as the total fatigue life [103].

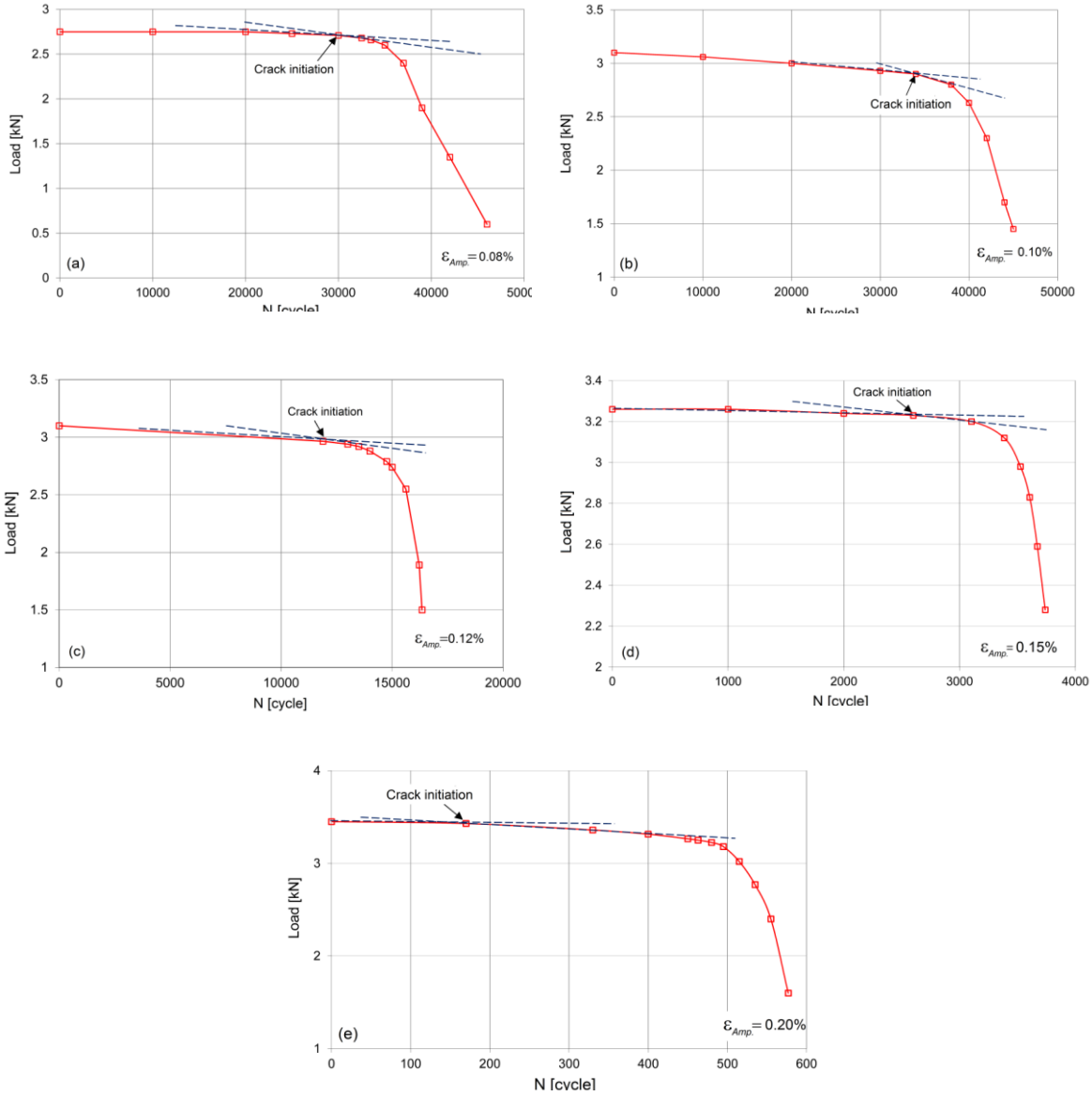

Figure 5-2- Load versus the number of cycles for strain amplitudes of (a) 0.08%, (b) 0.10%, (c) 0.12%, (d) 0.15%, and (e) 0.20%

The fatigue crack growth (FCG) life and total fatigue life for different strain amplitudes are presented in Figure 5-3 (a) and (b), respectively. Furthermore, the test results are summarized in Table 5-1. Fatigue cracks can easily initiate from brazing defects inside the joints. Since the brazed specimens are not ideally from the same quality, the crack initiation lives are more scattered than the crack propagation lives.

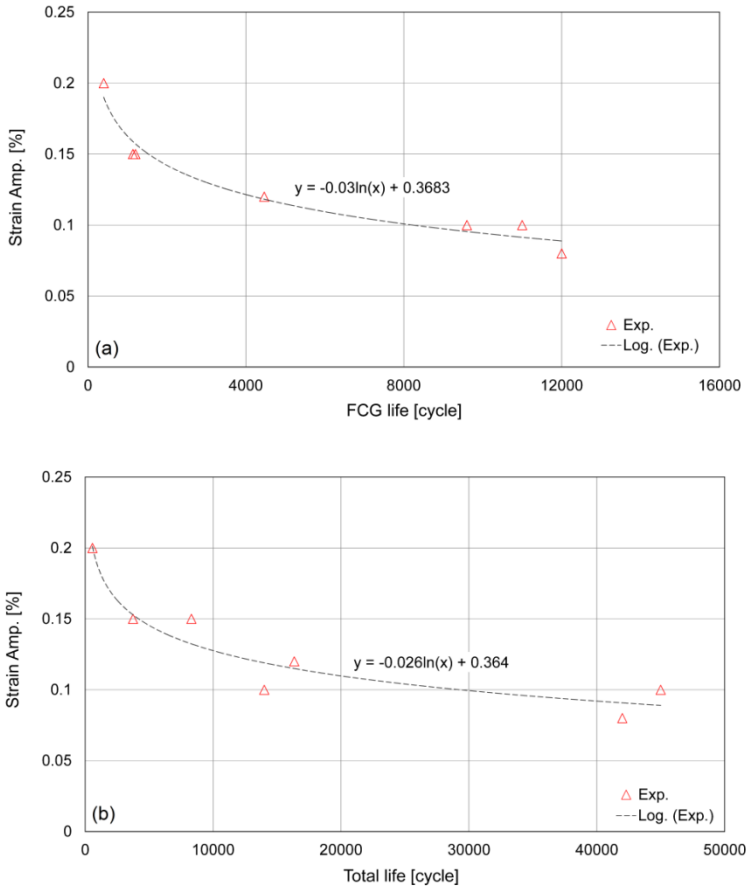

Figure 5-3- The experimental strain amplitudes versus (a) FCG life, (b) total fatigue life

Table 5-1 Crack initiation, propagation and total lives for different strain amplitudes

Specimen ID.	Strain Amp. [%]	Initiation life [cycle]	FCG life [cycle]	Total life [cycle]	Final load drop [%]
3	0.20	170	400	570	50
4	0.15	2600	1140	3740	50
5	0.15	7100	1203	8303	50
6	0.12	11884	4466	16350	50
1	0.10	34000	11000	45000	50
2	0.10	4400	9600	14000	50
10	0.08	30000	12000	42000	50

5.2 Cohesive zone modeling of fatigue crack growth

In this section, fatigue crack growth is modeled using an irreversible CZM. Developing a Python script for ABAQUS 6.7, a damage evolution law is implemented into the constitutive equation of the cohesive elements to irreversibly degrade the cohesive zone stiffness over the number of cycles. The damage law parameters, which affect the rate of damage evolution, are calibrated based on analytical solutions and the experimental FCG data.

5.2.1 Cyclic damage evolution law

A cyclic damage evolution law, proposed by Bouvard et al. [54], is used in this study. This damage law which was motivated based on Roe and Siegmund's model is as below:

$$\dot{D_c} = A(1 - D_c)^m \langle \frac{T}{1 - D_c} - T_0 \rangle^n \left\| \dot{U} \right\| \tag{5-1}$$

where A, m and n are the parameters which control the rate of damage evolution, and T_0 is a traction threshold or the CZM fatigue endurance limit under which the damage variable does not evolve [54]. Moreover, $\dot{U}$ indicates the rate of change in separation within the cohesive zone.

The traction-separation stiffness, k, degrades due to damage accumulation in each cycle, as follows:

$$k = k_0(1 - D_c) \tag{5-2}$$

where k_0 is the initial stiffness of the CZM.

Figure 5-4 shows the fully reversed sinusoidal displacement wave, $w(t)$, applied to the specimens and the corresponding loading, unloading and reloading paths on the traction-separation model. In the first loading cycle the damage develops on the monotonic softening path. It is assumed that unloading paths on the

traction-separation model are always toward the origin [54]. The cyclic damage evolves during loading when the tractions are positive, and remains constant during unloading [49].

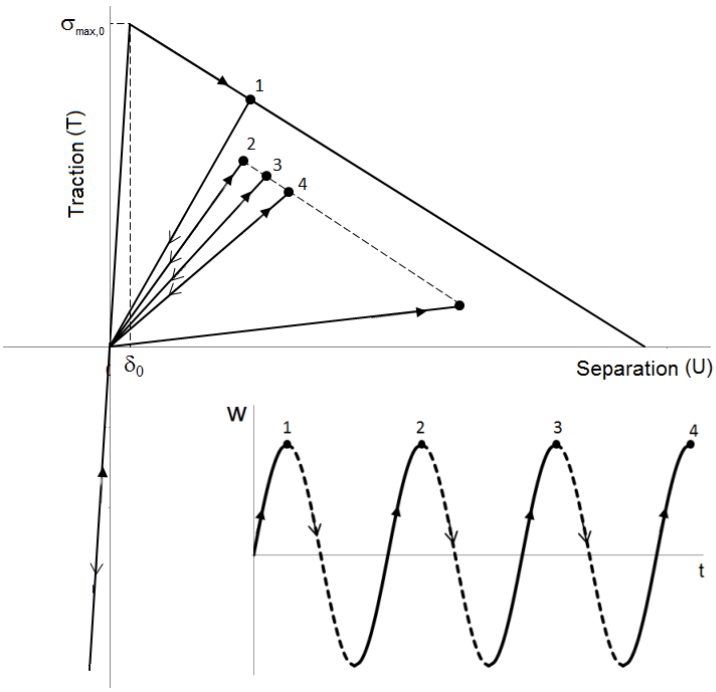

Figure 5-4- Applied displacement wave, w(t), and the corresponding loading-unloading paths on the traction-separation model

Since the damage evolution needs to be calculated for each cycle, the fatigue analysis would be a time consuming procedure. Therefore, the FE analysis is only performed for a selected cycles and the damage variable is extrapolated for the next ΔN cycles, as follows:

$$D_{N+\Delta N} \approx D_N + \frac{dD_N}{dN}\Delta N \tag{5-3}$$

where ΔN is selected such that the damage evolution ($D_{N+\Delta N} - D_N$) is sufficiently small [54]. Implementation of the cyclic damage evolution law into the CZM is provided in the following section.

5.2.2 Numerical implementation of cyclic damage evolution law into the CZM

The cyclic damage evolution law is implemented into the cohesive zone constitutive model. To this aim, a script was developed for ABAQUS 6.7 in Python programming language to account for cohesive element stiffness degradation due to damage accumulation in each cycle. The script is first validated by comparing FE results with the analytical solution available for a simple uniaxial problem. In this case a rod with a central joint under a fully reversed uniaxial cyclic loading is considered, as shown in Figure 5-5. The rod has a length and radius of 0.02 mm and 0.01 mm, respectively. The material properties and cyclic damage law parameters used in the analysis are given in Table 5-2.

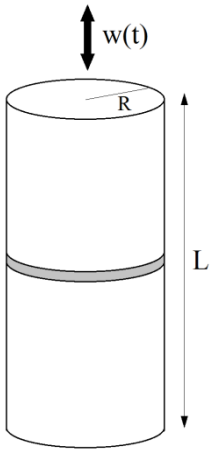

Figure 5-5- A rod with a central butt joint under cyclic loading

Table 5-2 Material properties and damage law parameters used in the analysis

Parameter	Value
Young's modulus [GPa]	30
Poisson's ratio	0.25
k_0 $[\frac{\mathrm{GPa}}{\mathrm{mm}}]$	1e9
A $[\mathrm{MPa}^{-1}.\mathrm{mm}^{-1}]$	3000
m	3
n	1
T_0 [MPa]	100

The uniaxial cyclic displacement, applied to the one end of the rod, is given as below:

$$w(t) = A_0 \, Sin\left(\frac{\pi t}{2}\right) \tag{5-4}$$

where the value of A_0 is assumed to be 0.0002 mm.

A linear traction-separation law, Eq. (5-5), is considered as the joint constitutive model, and it is assumed that the maximum traction never reaches the cohesive strength.

$$T = k_0(1 - D_c)U \tag{5-5}$$

In the analytical solution the axial stress in the rod, σ, is expressed in terms of the joint separation, U, as follows:

$$\sigma = \frac{(w - U)}{L} E \tag{5-6}$$

where E is Young's modulus of the rod.

From the continuity requirement, the traction induced in the joint is equal to the axial stress in the rod ($T = \sigma$). Substituting Eq. (5-5) into Eq. (5-6), the separation at the joint is obtained as follows [49]:

$$U = w / \left[1 + \frac{kL}{E}(1 - D)\right] \tag{5-7}$$

Using the above analytical solution, a MATLAB code is developed for cycle by cycle analysis of this problem.

Figure 5-6 shows the axisymmetric FE model of the rod under uniaxial loading. One end of the rod is fixed and the axial displacement is applied to the other end of the model. The base metal and joint regions are meshed by 4-node bilinear axisymmetric quadrilateral continuum elements (CAX4R) and 4-node axisymmetric cohesive elements (COHAX4), respectively.

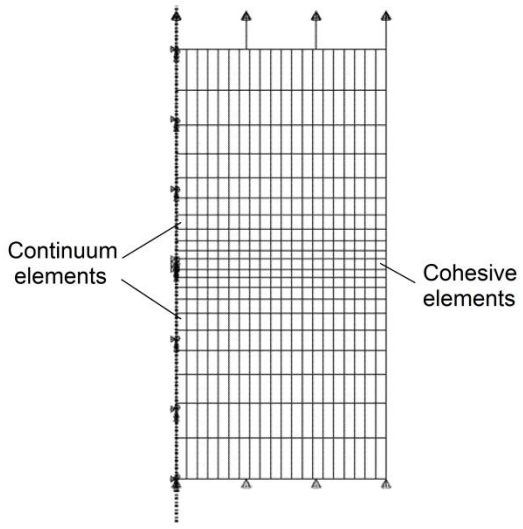

Figure 5-6- Axisymmetric FE model of the rod under uniaxial loading

Using the Python script, the joint traction and separation are taken from output database of the FE analysis to calculate the damage evolution in each cycle. Accumulating the damage variable, the stiffness of the cohesive elements are

degraded accordingly and assigned to the model for analysis of the next cycle. Figure 5-7 shows the flowchart of the Python script developed for damage analysis for each cycle (*i*).

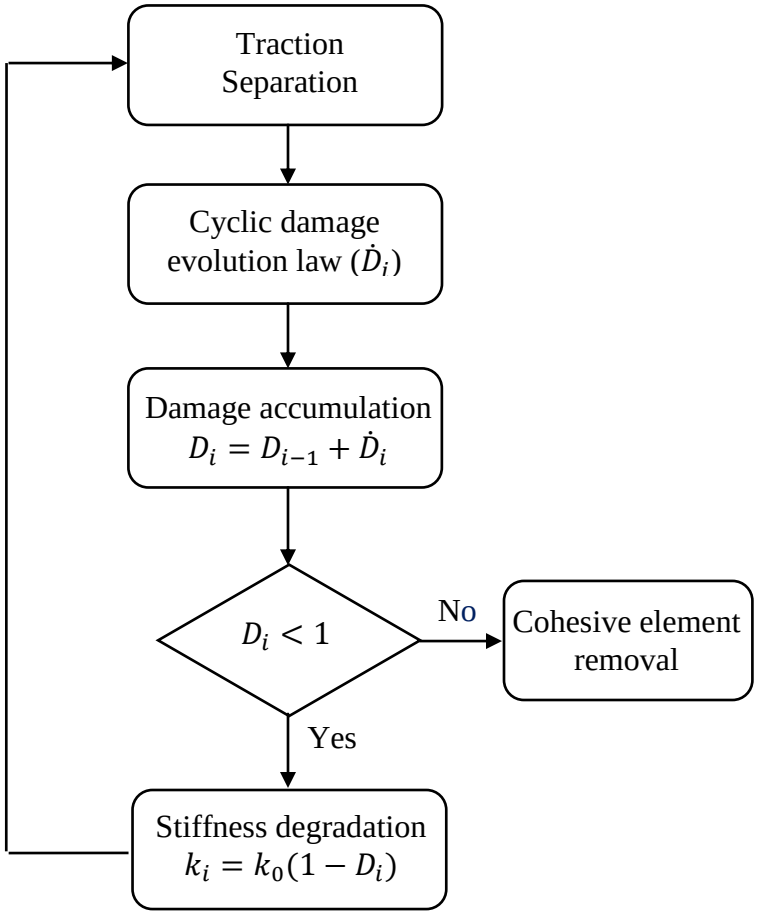

Figure 5-7- Flowchart of the cyclic damage analysis

The damage variable obtained from the FEM and analytical solution are plotted and compared in Figure 5-8. It is observed that the damage evolves rapidly at the beginning and propagates with a lower rate during the last cycles until it reaches the critical value of 1. The cyclic traction-separation curves obtained from the FEM and analytical solution are plotted in Figure 5-9. The figure shows the gradual degradation of the cohesive stiffness over the number of cycles. The good agreement between the results of the FEM and analytical solution validates the accuracy of the Python script developed for the cyclic FE analysis. This script will be used for modeling FCG in the next section.

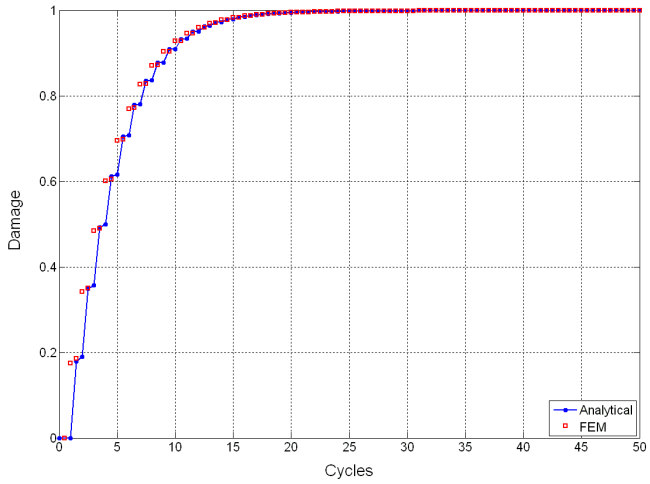

Figure 5-8- Damage evolution over the number of cycles from the FEM and analytical solution

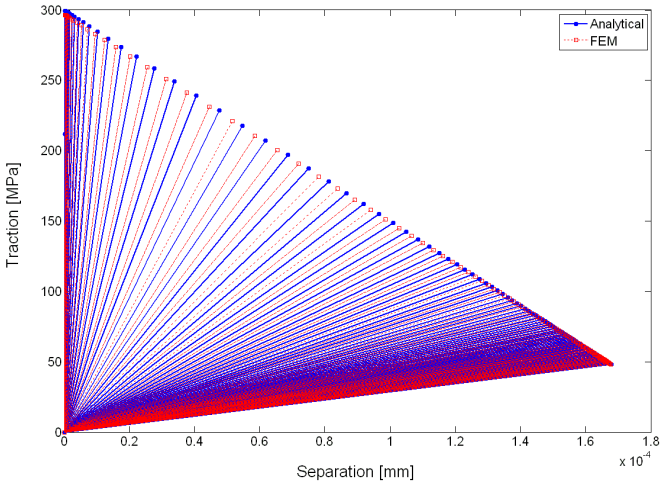

Figure 5-9- Cyclic traction-separation curves from the FEM and analytical solution

5.2.3 Calibration of the cyclic damage evolution law and modeling FCG

In this section fatigue crack growth in the brazed specimens is modeled using the Python script developed for the cyclic damage analysis in ABAQUS 6.7. Load drop percentage is considered as an indication of fatigue crack growth in the analysis. The initial crack length at the beginning of load drop is estimated by FEM. Then, cycle by cycle FE analysis is performed to account for damage evolution and cohesive element stiffness degradation. Loss of load bearing capacity in fully damaged cohesive elements simulates fatigue crack propagation.

- **Estimation of the initial fatigue crack length**

In order to estimate the fatigue crack length at initiation of load drop, the fatigue specimen with different crack lengths, a, is modeled in ABAQUS, Figure 5-10. One row of the cohesive elements (COH2D4) is placed along the joint region. The surrounding base metal regions are meshed by 4-node quadrilateral bilinear elements (CPS4R) in the plane stress condition [4]. The same material properties are defined for the base and filler metal regions as provided in Chapter 4.

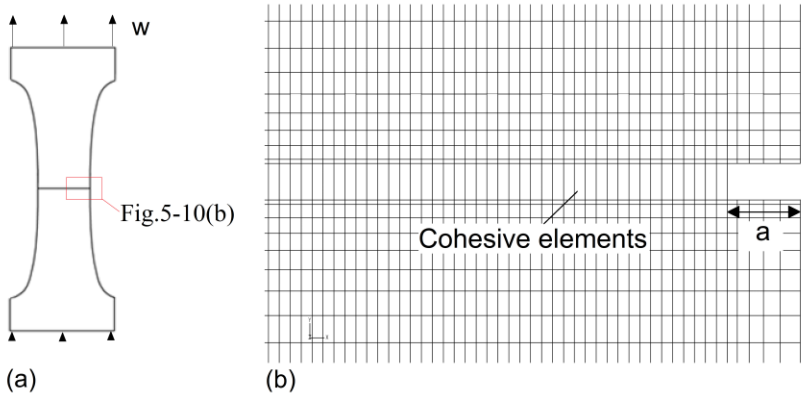

Figure 5-10- FE model of the fatigue specimen with an initial crack

One end of the specimen is fixed and axial displacement is applied to the other end of the model. Applying the same amount of axial displacement to the FE models with different crack lengths, the corresponding axial load levels are obtained. The load drop percentage is calculated respect to the load level in an intact model and plotted with respect to the crack length, as shown in Figure 5-11. This figure

shows that the load drop starts at the crack length of 0.1 mm. Hence, for the purpose of fatigue crack growth simulation an initial crack with the length of 0.1 mm is created in the model.

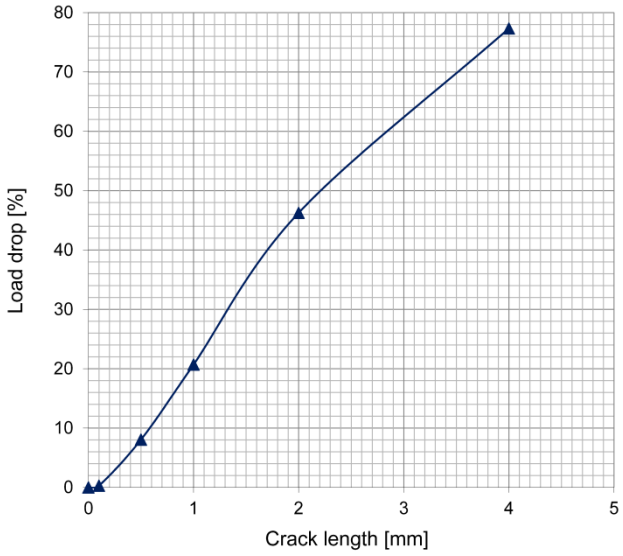

Figure 5-11- Load drop percentage versus the crack length created in the FE model

- **Damage law parameter determination and modeling of fatigue crack growth**

As described in the previous section, the cyclic damage evolution law was implemented into the cohesive element constitutive model using the developed Python script. Fatigue crack growth is simulated by successive degradation of the cohesive elements in the FE model. The 10-mm gage section of the fatigue specimen

with the initial crack length of 0.1 mm is modeled, as shown in Figure 5-12. The axial deformation which is experimentally measured by the extensometer is applied as the boundary condition of the model.

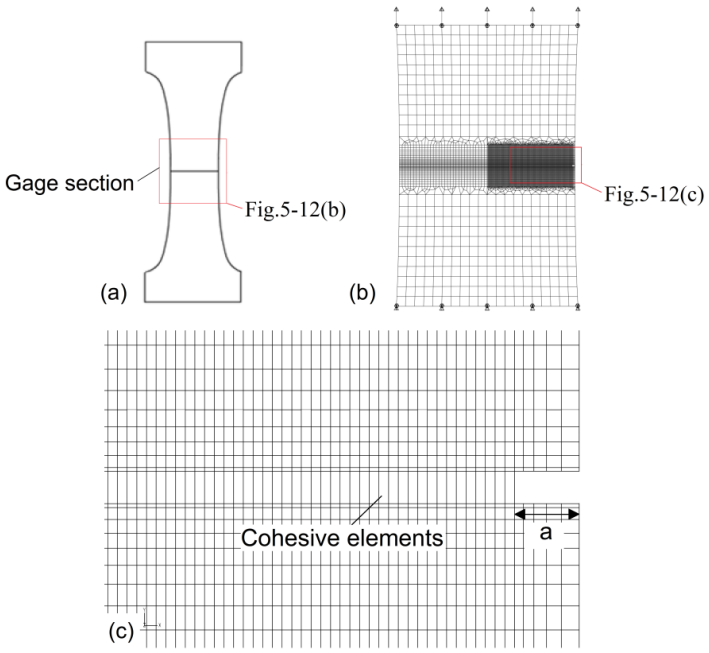

Figure 5-12- FE model of the fatigue specimen with an initial crack

The cohesive element size in the FE model is selected based on the criterion proposed by McClung and Sehitoglu [104]. According to this criterion, at least 10 elements have to be included in the crack tip plastic zone to have accurate results. Using McClung's criterion on the fracture process zone (FPZ), the length of the cohesive elements, $L_{e,CZM}$, is selected such that:

$$L_{e,CZM} \leq 0.1 L_{FPZ} \tag{5-8}$$

where L_{FPZ} is the length of the fracture process zone [54].

The length of the FPZ can be estimated based on Irwin's theory for plastic zone size. In the plane stress condition, this estimation is made by Eq. (5-9):

$$L_{FPZ} = \frac{1}{\pi}\left(\frac{K_I}{T_0}\right)^2 \tag{5-9}$$

$$K_I = 1.12\sigma_\infty\sqrt{\pi a} \tag{5-10}$$

where σ_∞ is the far field axial stress and a is the crack length [54,95].

In order to obtain the maximum allowable length of the cohesive elements, a minimum value of the stress intensity factor, which corresponds to the initial crack length of 0.1 mm and the strain amplitude of 0.10%, is calculated in Table 5-3. The value of the CZM fatigue endurance limit, T_0, is taken equal to $T_0 = 0.25\sigma_{max,0}$ [37]. According to this table, the length of the FPZ and the maximum size of the cohesive elements are obtained equal to 0.3920 mm and 0.0392 mm, respectively. Therefore, the selected length of 0.015 mm for the cohesive elements in the FE model satisfies McClung's criterion.

Table 5-3 Calculation of the maximum size of the cohesive elements

$\varepsilon_{Apm.}$[%]	σ_∞ $[MPa]$	a $[mm]$	$K_I[Mpa\sqrt{m}]$	T_0 $[MPa]$	L_{FPZ} $[mm]$	$L_{e,CZM}$ $[mm]$
0.10	198	0.1000	3.5095	100	0.3920	0.0392

The parameter m, which controls the damage rate, affects the number of cohesive elements in the FPZ. Thus, this parameter is calibrated such that the length of the FPZ obtained from the FEM matches that of the analytical solution. According to Roe and Siegmund's damage law the exponent of the term $\langle \frac{T}{1-D_c} - T_0 \rangle$, i.e., the value of the parameter n in Eq. (5-1), is set equal to 1 [37]. Using the parameters listed in Table 5-4, cycle by cycle FE analysis is performed for the strain amplitude of 0.15%. Figure 5-13 shows the far field stress and traction distribution obtained for the crack length of 0.1 mm. As described in Chapter 2, the length of the FPZ is taken form the material crack tip to the mathematical crack tip. The numerical and analytical lengths of the FPZ for different stages of the crack propagation are plotted in Figure 5-14. The results show that using the value of 1.75 for the parameter m provides numerical results that are in good agreement with the analytical solution.

Table 5-4 Parameters used in FCG analysis

k_0 [GPa/mm]	A [$\mathrm{MPa^{-1}.mm^{-1}}$]	n	$\sigma_{max,0}$ [MPa]	T_0 [MPa]
1640	0.05	1	400	100

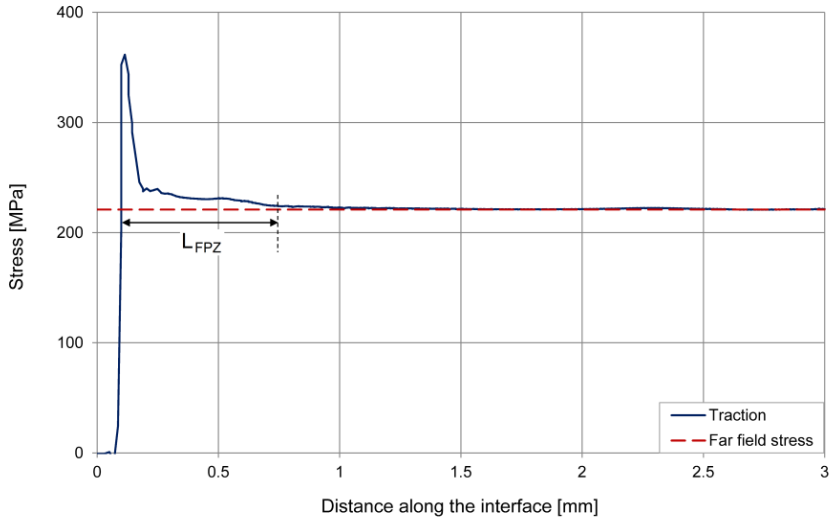

Figure 5-13- Traction and far field stress along the interface

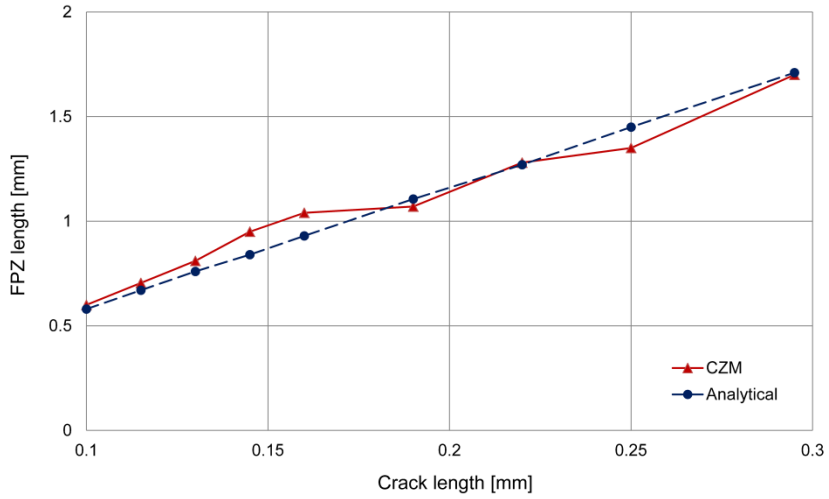

Figure 5-14- Analytical and numerical FPZ length with respect to the crack length for *m*=1.75

In order to calibrate the parameter *A* of the cyclic damage evolution law, the experimental rate of load drop percentage is plotted for the strain amplitudes of

0.12%, 0.15% and 0.20%, and compared with the FE simulation results, as shown in Figure 5-15. The value of the parameter A for each strain amplitude is obtained such that the FE results best fit the corresponding experimental data. The values of the parameter A obtained for different strain amplitudes are listed in Table 5-5.

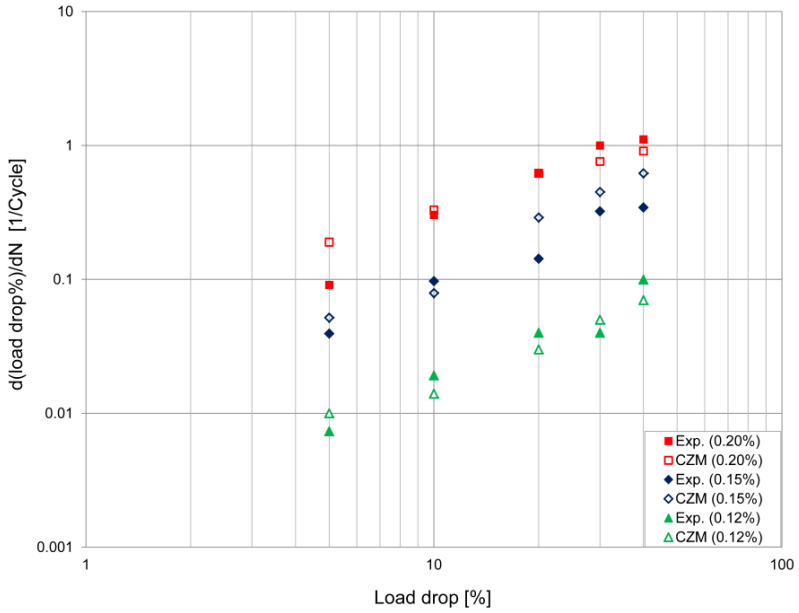

Figure 5-15- Experimental and numerical load drop rate for different strain amplitudes

Table 5-5 Values of the parameter A obtained for different strain amplitudes

$\varepsilon_{Apm.}$[%]	A[MPa^{-1}.mm^{-1}]
0.12	0.009
0.15	0.031
0.20	0.060

An average value for the parameter A is calculated based on the least squares method as follows:

$$R = \sum_{i=1}^{3} (A_i \varepsilon_i - \bar{A} \varepsilon_i)^2 \tag{5-11}$$

where the value of $\bar{A}$ is obtained such that to minimize the residual function of R, as bellow:

$$\frac{\partial R}{\partial \bar{A}} = 0 \tag{5-12}$$

$$\bar{A} = \frac{\sum_{i=1}^{3} A_i \varepsilon_i}{\sum_{i=1}^{3} \varepsilon_i} \tag{5-13}$$

Using the equation (5-13), the value of $\bar{A}$ is obtained equal to 0.037.

Using the obtained parameters, fatigue crack growth is simulated. Figure 5-16 shows the contours of the traction and stress perpendicular to the crack faces (S22) for the strain amplitude of 0.15% at the selected number of cycles of 2, 500, and 800.

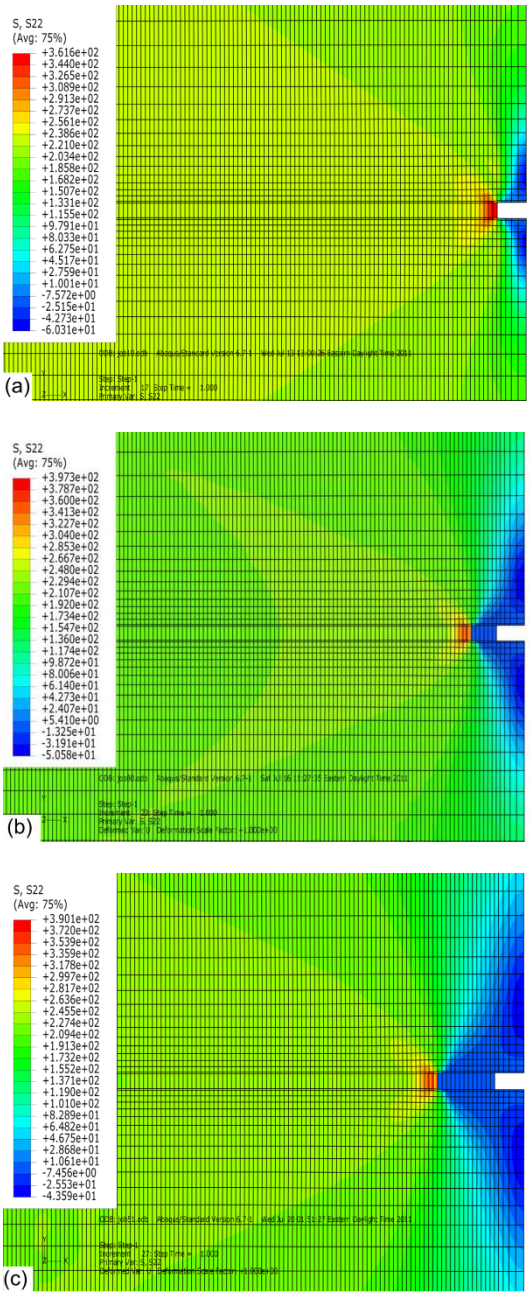

Figure 5-16- Contours of axial stress (S22) around the crack tip for $\varepsilon_{Apm.} = 0.15\%$ at (a) N=2 cycles, (b) N=500 cycles, (c) N=800 cycles

The traction distributions from the initial crack tip along the joint interface are shown in Figure 5-17. Furthermore, the corresponding distributions of the damage variable and the cohesive stiffness are plotted in Figure 5-18 and Figure 5-19, respectively. The results show that at the beginning of the cyclic loading, the damage has slightly evolved through the crack tip cohesive elements which results in the traction decrease. Increasing the number of cycles, the damage propagates through the crack tip cohesive elements and the cohesive stiffness decreases accordingly. Once the damage variable reaches the critical value of 1, the cohesive elements are fully degraded and totally lose their load bearing capacity which simulates crack propagation.

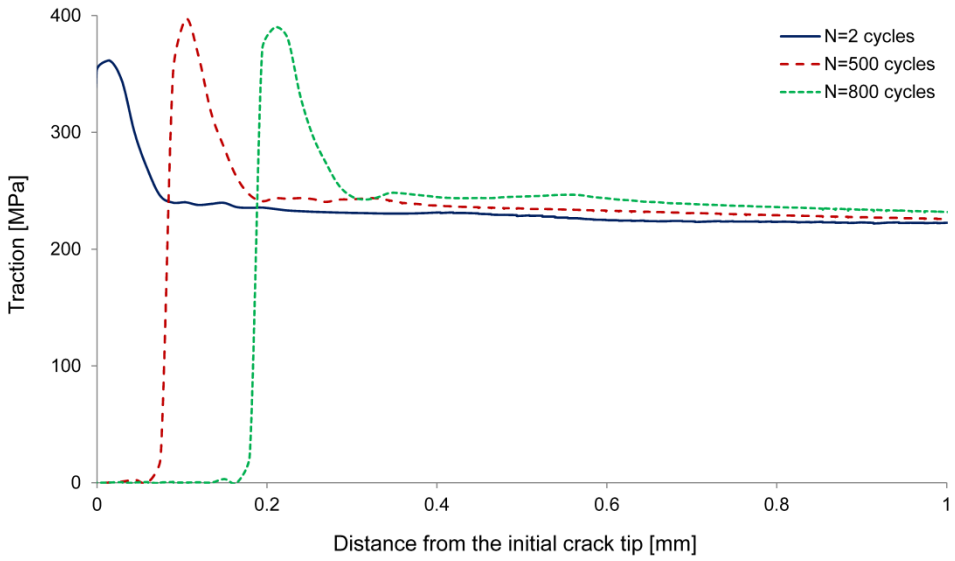

Figure 5-17- Traction distributions along the interface for $\varepsilon_{Apm.} = 0.15\%$ at different cycles

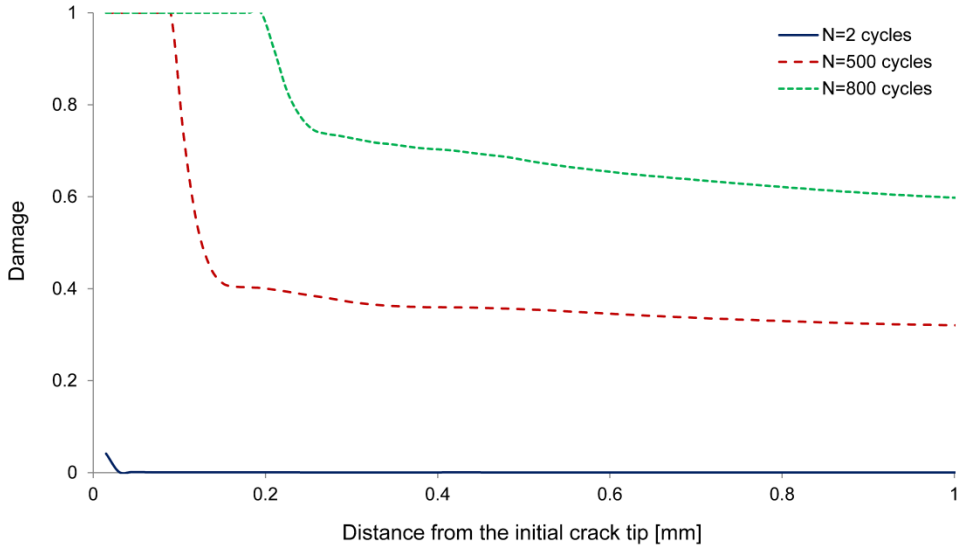

Figure 5-18- Damage distributions along the interface for $\varepsilon_{Apm.} = 0.15\%$ at different cycles

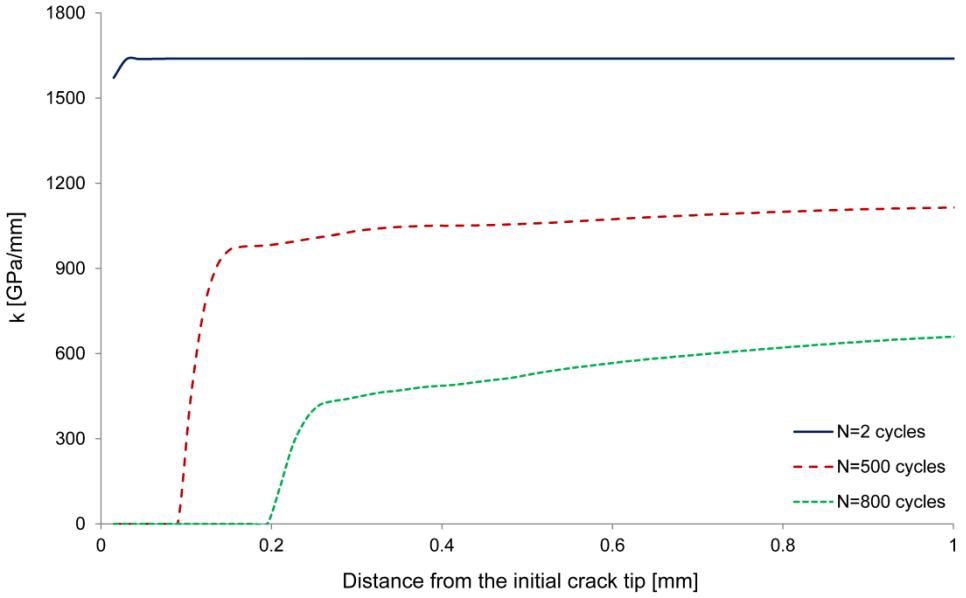

Figure 5-19- Cohesive stiffness distributions along the interface for $\varepsilon_{Apm.} = 0.15\%$ at different cycles

Figure 5-20 shows the experimental strain-FCG life curve in comparison to the results obtained from the characterized irreversible CZM. The predicted results are in good agreement with the experimental ones, which shows the applicability of the CZM to fatigue analysis of brazed joints.

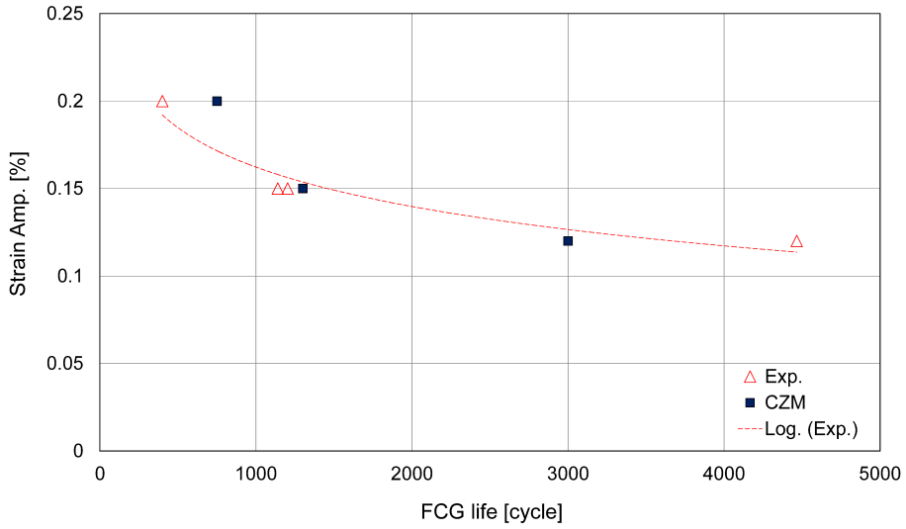

Figure 5-20- Experimental strain-FCG life curve in compared to the CZM results

5.3 Summary

In this chapter, fatigue crack growth in brazed joints was modeled by an irreversible CZM. Fully reversed strain controlled fatigue tests were performed on the brazed specimens. A damage evolution law was introduced and implemented into the constitutive equation of the cohesive elements to irreversibly degrade the

cohesive zone stiffness over the number of cycles. The following conclusions are drawn from this chapter:

1. Fatigue failure behavior of the brazed joints was characterized by performing fully reversed strain controlled cyclic tests. A fatigue crack was considered to be initiated when the softening rate of the load-cycle curve accelerates. The number of cycles to failure at 50% load drop was taken as the total fatigue life. The strain-life curves in terms of fatigue crack growth and total lives were obtained.

2. Developing a Python script for ABAQUS 6.7, a cyclic damage evolution law was coupled to the cohesive zone constitutive model to account for the joint stiffness degradation. The accuracy of the cyclic damage analysis was validated by comparing results of the FE modeling of a simple uniaxial problem with that of the corresponding analytical solution.

3. In order to have accurate results in FCG analysis, a proper size for the cohesive elements was selected based on McClung's criterion on the fracture process zone.

4. The damage evolution law parameters were calibrated based on Irwin's analytical solution on the FPZ and the experimental fatigue crack growth

data. The parameter m, which controls the damage rate, was calibrated such that the length of the FPZ obtained from the FEM matches that of the analytical solution. The value of the parameter A for each strain amplitude was calibrated such that the rate of load drop percentage obtained from the FE simulations best fits the corresponding experimental data. An average value for the parameter A was calculated based on the least square method. Using the characterized irreversible CZM, the fatigue crack growth for different strain amplitudes was simulated. The agreement between the predicted results and the experimental data shows the applicability of the CZM to FCG life prediction of brazed joints.

Chapter 6
Concluding Remarks and Future Works

6.1 Summary and Conclusions

In this research, the mechanical reliability of low carbon steel brazed joints with copper filler metal has been investigated. The methodology for fracture analysis of brazed joints under quasi-static loading using the CZM has been presented. This method has been successfully applied to low carbon steel brazed joints with copper

filler metal. Furthermore, a cyclic damage evolution law has been introduced and coupled to the CZM to irreversibly account for the joint stiffness degradation over the number of cycles and estimate the fatigue crack growth life of brazed joints.

A summary of the current research contributions to the failure analysis of brazed joints is given as follows:

1. Mechanical and microstructural characterization of brazed joints

The strength of the brazed joints was experimentally evaluated, and successfully estimated by the FEM. The effect of base metal yield limit on the joint tensile strength was investigated. It was found that a higher yield limit of the base metal increases the joint tensile strength. The shear strength of the brazed joints was measured from the torsion test performed on thin-walled tubular specimens. The biaxial strength and deformation behavior of the joints were also evaluated by tension-torsion tests for different extension to twist angle ratios. A mixed mode power law failure criterion was best-fitted to the experimental results. Applying the experimentally measured deformations of the tensile and torsion specimens into the FE models, the joint strengths were estimated well. Furthermore, the numerical results obtained from the FE simulation of the biaxial tension-torsion tests were in good agreement with the power law failure criterion fitted to the experimental data.

The fracture toughness of the brazed joints was experimentally evaluated for the SENB and SENT specimens. Fracture toughness values and the corresponding crack resistance curves for the two different tested specimens showed dependency on the geometry and loading configuration. A higher geometrical crack tip constraint effect in the SENB specimens significantly decreases the joint toughness. However, the growing crack tip plastic zone of the SENT specimens leads to a more ductile behavior which was observed from its corresponding resistance curve. Consequently, using the fracture toughness obtained from a SENB specimen leads to an excessive conservatism in engineering designs.

The microstructure of the brazed joints was studied and different failure mechanisms and their corresponding sources were identified. The joint microstructure and element composition of the brazed joints were examined by SEM-BEI technique and the chemical EDS analysis, respectively. The MnS and Fe-rich dendrites identified in the brazed filler metal region serve as the damage initiation locations in the mechanical testing. SEM-SEI images showed that failure happened at the joint filler metal region. The EDS analysis on the joint fracture surfaces revealed that the MnS-rich dendrites are the sites of dendritic failure, while the finer Fe-rich dendrites and microvoids cause the dimple rupture in the tensile specimens. The SEM image of the torsion specimen showed the ductile dimple rupture mechanism which was initiated at the dendrites and microvoids.

2. Development of a methodology for fracture analysis of brazed joints using the CZM

The bilinear CZM, as a two-parameter fracture analysis tool, was successfully employed to predict mode-I fracture and simulate ductile tearing process in the brazed joints. Using the CZM, the energy needed for material debonding is decoupled from the large scale plastic work dissipated around the crack tip. Hence, the characterized CZM is capable of nonlinear fracture analysis of the steel/Cu/steel brazed joints independent of geometry and loading configurations.

In the present research, the CZM parameters of the cohesive strength and the cohesive energy were characterized from the four-point bend fracture test results accompanied with the corresponding FE simulation. The cohesive energy was directly obtained from the fracture test performed on the pre-cracked SENB specimens. Excluding the base metal plastic work dissipated around the crack tip, the elastic component of the critical energy release rate, i.e., the energy needed for material separation per unit area of the crack advance, is the joint cohesive energy in the ductile tearing process. In the case that the base material remains elastic or the crack tip plastic zone is in the range of small scale yielding, the entire critical energy release rate can be considered as the cohesive energy of a brazed joint.

The cohesive strength of steel/Cu/steel brazed joints was determined such that the FE simulation results best fit to the experimental load-CMOD curve obtained from the fracture test. The simulation results in the plane strain condition noticeably underestimated the crack tip plastic deformation; rather, the results obtained in the plane stress condition agreed well with the nature of this problem.

To validate the characterized CZM, the tensile test performed on the SENT specimens was simulated. The obtained load-CMOD curve from the FE model was in good agreement with the corresponding experimental results. The effect of the crack tip stress triaxiality on the plastic zone shape and size was captured well by the model. The low crack tip triaxiality factor in the SENT specimens resulted in a more developed plastic zone than that of the SENB specimens. Moreover, for both types of the specimens, the critical and maximum load levels were predicted well by the CZM. The good agreement between the FE simulation results and the experimental data shows the uniqueness of the obtained CZM parameters. This indicates that once the CZM parameters are determined for a brazed joint, the CZM is capable of predicting the joint fracture independent of geometry and loading configurations.

3. Extension of the CZM approach to fatigue crack growth analysis of brazed joints

A cyclic damage evolution law was introduced and coupled to the CZM to irreversibly account for the joint stiffness degradation over the number of cycles. Fully reversed strain-controlled fatigue tests with different strain amplitudes were performed on the brazed specimens. A fatigue crack was considered to be initiated when the softening rate of the load-cycle curve accelerates. The number of cycles to failure at 50% load drop was taken as the total fatigue life. In the cyclic FE analysis using the irreversible CZM, the cyclic damage evolves during loading when the tractions are positive, and remains constant during unloading. Assuming the small scale yielding condition in the cyclic FE analysis, the effect of the base metal residual stresses on the crack tip tractions is neglected during unloading. The damage law parameters, which affect the rate of damage evolution in the cohesive zone FE model, were calibrated based on analytical solutions and the experimental fatigue crack growth data. The characterized irreversible CZM showed applicability to FCG life prediction of brazed joints.

6.2 Recommendations for future work

The following recommendations are suggested for the future work based on the present study:

- Effect of the brazing conditions such as hold time, temperature and cooling rate on the joint strength and toughness need to be studied. Volume fraction of micro voids, MnS and Fe-rich dendrites formed in the brazed joint should be correlated to the joint strength and ductility.

- In this study failure of the brazed joints with a constant joint clearance was investigated. Effect of the joint clearance on the joint strength and fracture can be studied experimentally and numerically. The CZM approach can be applied to failure analysis of brazed joints with different clearances. Modeling the joint interlayer thickness by the continuum elements and placing a single row of the zero-thickness cohesive elements at the middle of the interlayer, the constraint effect of the base metal on the crack tip plastic deformations and the cohesive tractions is taken into account. Hence, a generalized CZM can be characterized for fracture prediction independent of the joint clearance.

- In the current work, mode I failure of the brazed joints was studied using the CZM. Since the brazed joints can experience complicated loading conditions in an assembly, the corresponding failure analysis should be considered. The CZM approach can be extended to failure studies of brazed joints in mode II as well as the mixed mode of loading to predict the joint failure in a brazed assembly.

- The characterized CZM can be applied to failure analysis of the laminated injection mold bonded by brazed joints.

Appendix A.
Construction of the Cohesive Zone Constitutive Model

The cohesive zone constitutive model is developed in the continuum damage mechanics (CDM) framework. By introducing a single scalar damage parameter into the traction-separation law, degradation of the interfacial stiffness under applied loading is taken into account. A brief introduction to the CDM is provided first; then the CZM constitutive equations in monotonic and cyclic loading conditions are derived.

- **Continuum Damage Mechanics (CDM)**

In the continuum mechanics quantities are defined at a mathematical point. From the physical point of view, a Representative Volume Element (RVE) must be defined at a point such that it is small enough to account for high gradients but large enough to represent an average of micro-processes. Such a RVE is capable of describing meso-mechanisms in the meso-scale level. In order to formulate damage evolution in the continuum mechanics, a meso-scale volume element must represent the effect of micro-defects on failure mechanisms [105]. Figure A-1 shows a RVE at point P in a damaged body.

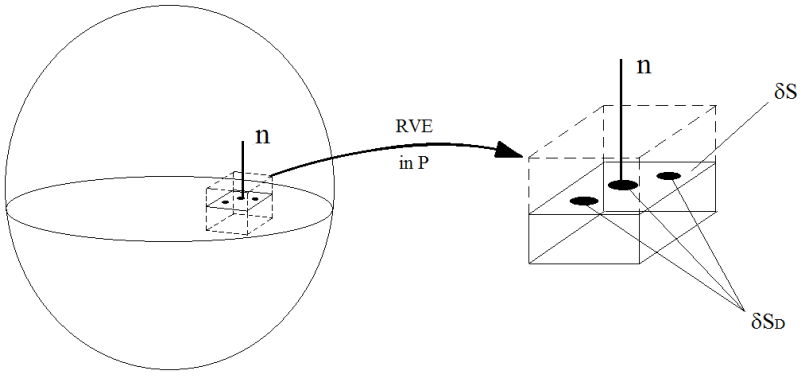

Figure A-1- A RVE in a damaged body

The damage variable at point P and plane n is defined as follows:

$$D_{(P,n)} = \frac{\delta S_D}{\delta S} \tag{A-1}$$

where S and S_D represent the total cross section and the damaged area, respectively [105].

In the case of one-directional damage or assumption of isotropy, shown in Figure A-2, equation (A-1) can be simplified as follows:

$$D = \frac{S_D}{S} \tag{A-2}$$

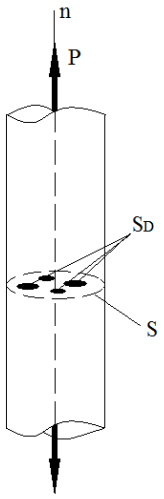

Figure A-2- Uniaxial damaged element

The applied uniaxial force, P, induces the uniaxial stress field in the RVE, σ, as follows:

$$\sigma = \frac{P}{S} \tag{A-3}$$

Considering the damaged area, S_D, the effective stress, $\tilde{\sigma}$, is defined as:

$$\tilde{\sigma} = \frac{P}{S - S_D} \tag{A-4}$$

Replacing equation (A-2) into equation (A-4), the effective stress in terms of stress field in an undamaged body is obtained as follows:

$$\tilde{\sigma} = \frac{P}{S(1 - \frac{S_D}{S})} \rightarrow \tilde{\sigma} = \frac{\sigma}{1 - D} \tag{A-5}$$

Furthermore, an effective elastic modulus, $\tilde{E}$, can be defined as follows:

$$\varepsilon_e = \frac{\tilde{\sigma}}{E} = \frac{\sigma}{E(1 - D)} \tag{A-6}$$

$$\tilde{E} = E(1 - D) \tag{A-7}$$

In other words, evolution of damage can be explained as gradual degradation of the elastic modulus, as shown in Figure A-3, [105].

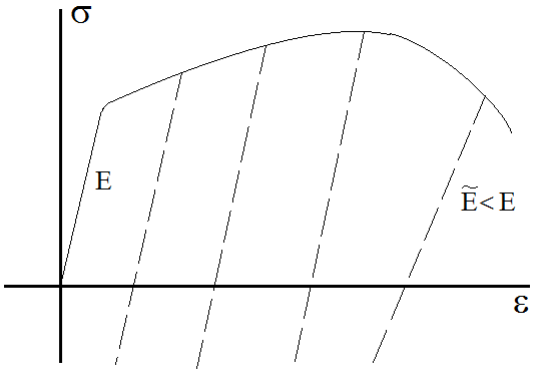

Figure A-3- Elastic modulus drop due to damage progress

In order to extend the concept of damage evolution to a three-dimensional stress state, an energy potential, as a function of state variables, is required to derive the state laws. The Helmholtz free energy function as a continuous scalar function, Ψ, is defined as follows:

$$\Psi = \Psi(\theta, \varepsilon, \varepsilon^e, \varepsilon^p, r, \alpha, D) \tag{A-8}$$

This potential function is concave with temperature, θ, and convex with the other state variables. Using the second principle of thermodynamics in the form of Clausius-Duhem inequality the state laws are obtained as follows [105]:

$$\sigma = \rho \frac{\partial \Psi}{\partial \varepsilon^e}$$
$$\sigma = \rho \frac{\partial \Psi}{\partial \varepsilon} = -\rho \frac{\partial \Psi}{\partial \varepsilon^p} \tag{A-9}$$

Damage driving force, $\bar{Y}$, as an associated variable for the damage parameter, can be derived from the free energy potential function as below [105]:

$$\bar{Y} = \rho \frac{\partial \Psi}{\partial D} \tag{A-10}$$

Using the definitions of the state potential and the associated variables, the CZM as a damage-based constitutive model is derived in the following.

- **Formulation of the cohesive zone constitutive model**

In order to derive a CDM-based interfacial constitutive model, an interface layer with a negligible thickness between two surrounding bulk materials is assumed, as shown in Figure A-4.

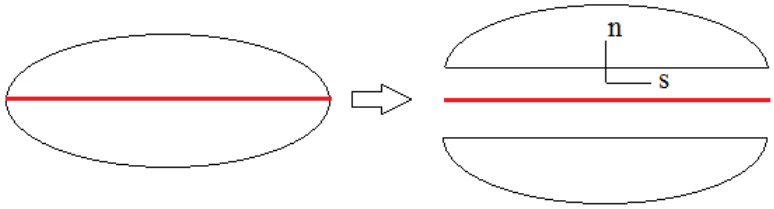

Figure A-4- Schematic of an interface

The cohesive model for the interfacial layer is described in terms of displacement jump vector, $[\![U]\!] = U^+ - U^-$, and the corresponding traction vector, T, as a measure of interfacial stress. The stored energy function at the interface is defined as:

$$\psi([\![U]\!], D) = \frac{1}{2}(1-D)k^+\langle[\![U]\!]\rangle_+^2 + \frac{1}{2}k^-\langle[\![U]\!]\rangle_-^2 \tag{A-11}$$

where k^+ and k^- are the initial interface stiffness in tension and compression, respectively. The function $\langle x\rangle_\pm$ is defined as follows:

$$\langle x\rangle_\pm = \frac{1}{2}(x \pm |x|) \tag{A-12}$$

Using the thermodynamics rules mentioned earlier, the interfacial traction,T, and strain energy release rate, Y, can be obtained as follow:

$$T = \frac{\partial \psi}{\partial [\![U]\!]} \tag{A-13}$$

$$Y = -\frac{\partial \psi}{\partial D} = \frac{1}{2} k^{+} \langle [\![U]\!] \rangle_{+}^{2} \tag{A-14}$$

Introducing the critical damage driving force, Y^{*}, the failure criterion can be defined as:

$$\Phi = Y - Y^{*} \leq 0 \tag{A-15}$$

According to the energy-based failure criterion, energy dissipated during the decohesion process is equal to the fracture energy,G_c, as follows [79]:

$$\int_{0}^{+\infty} Y \dot{D}\, dt = G_c \tag{A-16}$$

Several different models have been proposed in the literature to describe the relation between traction and separation at the cohesive zone. The bilinear, polynomial, and exponential forms are among the most widely used models which are described in the following.

A. Bilinear model

The bilinear traction-separation model, Figure A-5, is the most widely used form of the CZM which is described as:

$$Y^* = \begin{cases} G_o & D = 0 \\ F_A(D) = \dfrac{Y_f^2 G_o}{\left[G_o D + Y_f(1-D)\right]^2} & 0 < D < 1 \\ max\, Y(\tau)\,, \tau \in [0,t] & D = 1 \end{cases} \quad \text{(A-17)}$$

where $G_o$is the elastic energy at the damage onset, and Y_f is equal to the fracture energy, G_c.

Defining a regularization parameter, $\eta = 1 - \frac{G_o}{G_c}$, the damage function can be rewritten as [79]:

$$F_A(D) = \frac{(1-\eta)G_c}{(1-\eta D)^2} \quad \text{(A-18)}$$

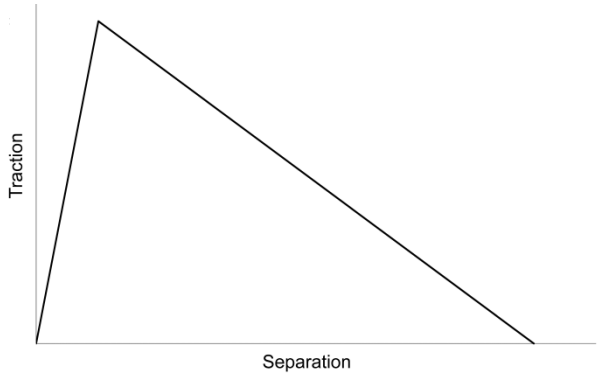

Figure A-5- Bilinear traction-separation model

B. Polynomial model

The polynomial traction-separation model, Figure A-6, is described as follows:

$$Y^* = \begin{cases} G_o & D = 0 \\ F_B(D) = G_o - \left(Y_f - G_o\right) D^{\frac{1}{N}} & 0 < D < 1, \ N > 0 \\ max\, Y(\tau)\,, \tau \in [0, T] & D = 1 \end{cases} \quad \text{(A-19)}$$

Using the energy balance of equation (A-16)(A-14), Y_f is obtained and substituted into equation (A-19) which yields:

$$F_B(D) = (1 - \eta) G_c + \left[\frac{N+1}{N} \eta G_c\right] D^{1/N} \quad \text{(A-20)}$$

where both η and N are the regularization parameters [79].

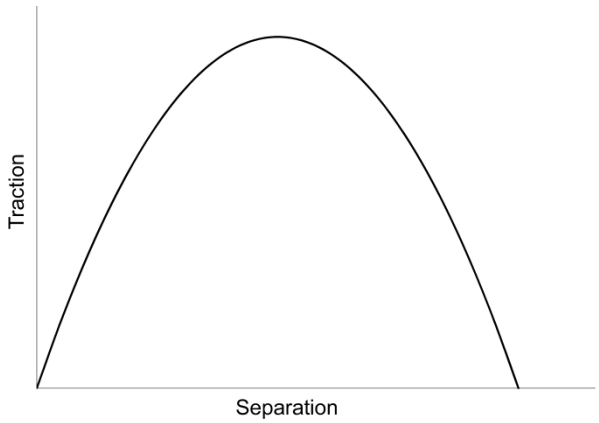

Figure A-6- Polynomial traction-separation model

C. Exponential model

The exponential traction-separation model, Figure A-7, is defined as follows:

$$Y^* = \begin{cases} G_o & D = 0 \\ F_C(D) = G_o - \left(Y_f - G_o\right)[-log(1-D)]^N & 0 < D < 1, N > 0 \\ max\, Y(\tau)\,, \tau \in [0,T] & D = 1 \end{cases} \quad \text{(A-21)}$$

Using the energy balance of equation (A-16), Y_f is obtained. Substitution of Y_f into equation (A-19) leads to equation (A-22) [79]:

$$F_C(D) = (1-\eta)G_c + \frac{1}{\Gamma(N+1)}\eta G_c[-log(1-D)]^N \quad \text{(A-22)}$$

where the Γ function is defined as: $\Gamma(N+1) = \int_0^{+\infty} x^N\, e^{-x} dx = N.\Gamma(N)$

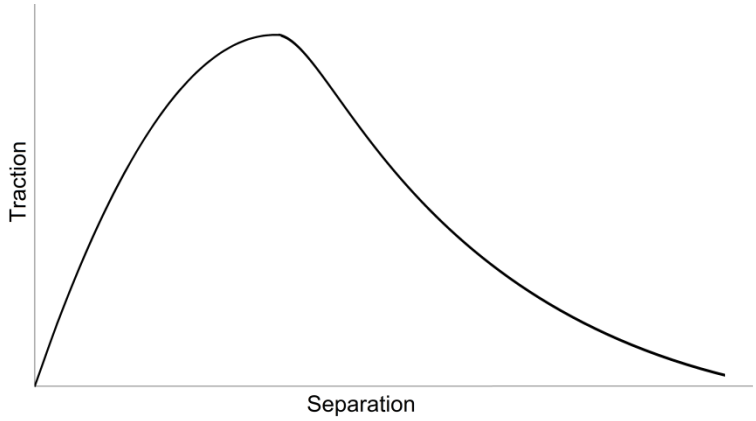

Figure A-7- Exponential traction-separation model

- **Mixed mode loading**

To derive equations correspond to the mixed mode loading cases, the energy function can be re-written as:

$$\psi([\![U]\!], D) = \frac{1}{2}(1-D)[k_n^+\langle[\![U_n]\!]\rangle_+^2 + k_s[\![U_s]\!]^2] + \frac{1}{2}k_n^-\langle[\![U_n]\!]\rangle_-^2 \quad \text{(A-23)}$$

where **n** and **s** are unit vectors in the normal and shear directions, respectively:

$$[\![U_n]\!] = [\![U]\!].\boldsymbol{n}$$

$$[\![U_s]\!] = [\![U]\!].\boldsymbol{s}$$

According to equations (A-13) and (A-14), the traction and damage driving force can be obtained as follow:

$$T = \frac{\partial \psi}{\partial [\![U]\!]} = (1-D)[k_n^+\langle[\![U_n]\!]\rangle_+ \boldsymbol{n} + k_s[\![U_s]\!]\boldsymbol{s}] + k_n^-\langle[\![U_n]\!]\rangle_- \boldsymbol{n} \quad \text{(A-24)}$$

$$Y_m = -\frac{\partial \psi}{\partial D} = \frac{1}{2}k_n^+\langle[\![U_n]\!]\rangle_+^2 + \frac{1}{2}k_s[\![U_s]\!]^2 \quad \text{(A-25)}$$

where subscript m indicates mixed mode variables in the corresponding equations.

Defining loading angle $\varphi = arctan(\frac{[\![U_s]\!]}{\langle[\![U_n]\!]\rangle_+})$, the mixed mode parameter, β, is defined as:

$$\beta = \alpha\, tan(\varphi) \quad \text{(A-26)}$$

where α is related to the ratio of the shear to normal stiffness of the interface as follows:

$$\alpha = \sqrt{\frac{k_s}{k_n^+}} \tag{A-27}$$

Contributions of the pure mode I and II into the mixed mode energy release rate can be expressed as:

$$Y_I = \frac{1}{1+\beta^2} Y_m \,,\; Y_{II} = \frac{\beta^2}{1+\beta^2} Y_m \tag{A-28}$$

Defining the equivalent traction,T_δ, the traction components in terms of the loading angle are written as follow:

$$T_\delta = \left(T_n^2 + \frac{1}{\boldsymbol{\alpha}^2} T_s^2 \right)^{1/2} \tag{A-29}$$

$$T_n = \frac{cos(\varphi)}{cos^2(\varphi) + \boldsymbol{\alpha}^2 sin^2(\varphi)} T_\delta \tag{A-30}$$

$$T_s = \frac{\boldsymbol{\alpha}^2 sin(\varphi)}{cos^2(\varphi) + \boldsymbol{\alpha}^2 sin^2(\varphi)} T_\delta \tag{A-31}$$

Damage initiation criterion in the mixed mode loading case is expressed as:

$$\left(\frac{Y_I}{G_{oI}} \right)^{\alpha_1} + \left(\frac{Y_{II}}{G_{oII}} \right)^{\alpha_2} - 1 = 0 \tag{A-32}$$

where G_{oI} and G_{oII} are the pure mode I and II damage initiation thresholds, and the parameters α_1 and α_2 are determined experimentally.

The corresponding value of damage driving force at the onset of damage initiation is defined as:

$$Y_{mo} = exp\left[-\frac{log(c_I + c_{II})}{\alpha_1}\right] = \frac{(1+\beta^2)G_{oI}G_{oII}}{[(G_{oII})^{\alpha_1} + (\beta^2 G_{oI})^{\alpha_1}]^{1/\alpha_1}} \tag{A-33}$$

where:

$$c_I(\beta) = \left[\frac{1}{(1+\beta^2)G_{oI})}\right]^{\alpha_1};\ c_{II}(\beta) = \left[\frac{\beta^2}{(1+\beta^2)G_{oII})}\right]^{\alpha_2} \tag{A-34}$$

The failure criterion which describes damage propagation is defined in an elliptical from as:

$$\left(\frac{G_I}{G_{oI}}\right)^{\beta_1} + \left(\frac{G_{II}}{G_{oII}}\right)^{\beta_2} - 1 = 0 \tag{A-35}$$

where:

$$G_i = \int_0^{+\infty} Y_i \dot{D}\, dt, \quad i = I, II \tag{A-36}$$

Total energy release rate, G_T, is the summation of energy release rates for each individual mode, i.e.: $G_T = G_I + G_{II}$

For the case that $\beta_1 = \beta_2$, the critical value of the total energy release rate is:

$$G_{Tc} = \frac{(1+\boldsymbol{\beta}^2)G_{cI}G_{cII}}{[(G_{cII})^{\beta_1} + (\boldsymbol{\beta}^2 G_{cI})^{\beta_1}]^{1/\beta_1}} \tag{A-37}$$

where G_{Tc} is calculated as the total work of separation:

$$G_{Tc} = \int_0^{+\infty} Y_m^* \dot{D}\, dt \tag{A-38}$$

The damage function for the bilinear model in the range of $0 < D < 1$ is obtained by:

$$F_{mA}(D) = \frac{Y_{mf}^2 Y_{mo}}{\left[Y_{mo}D + Y_{mf}(1-D)\right]^2} \tag{A-39}$$

The damage function for the polynomial and exponential models are also obtained by equations (A-39) and (A-40), respectively:

$$F_{mB}(D) = Y_{mo} + \left(Y_{mf} - Y_{mo}\right)D^{1/N} \tag{A-40}$$

$$F_{mC}(D) = Y_{mo} + \left(Y_{mf} - Y_{mo}\right)[-log(1-D)]^N \tag{A-41}$$

Characteristic values of the mixed mode energy release rates in the above equations are as follow [79]:

$$Y_{mfA} = G_{Tc} \tag{A-42}$$

$$Y_{mfB} = \frac{1}{N}[(N+1)G_{Tc} - Y_{mo}] \tag{A-43}$$

$$Y_{mfC} = Y_{mo} + \frac{1}{\Gamma(N+1)}[G_{Tc} - Y_{mo}] \tag{A-44}$$

- **Cyclic damage modeling using CZM**

In order to model damage evolution under cyclic loading, a cyclic damage variable,D_c, is introduced into the stored energy function as follows [54]:

$$\psi(\llbracket U \rrbracket, D_c) = \frac{1}{2}(1-D_c)[k_n{}^{+}\langle \llbracket U_n \rrbracket \rangle_{+}^{2} + k_s \llbracket U_s \rrbracket^2] + \frac{1}{2}k_n{}^{-}\langle \llbracket U_n \rrbracket \rangle_{-}^{2} \tag{A-45}$$

The traction components are obtained as:

$$T_n = \frac{\partial \psi}{\partial \llbracket U_n \rrbracket} = (1-D_c)k_n^{+}\langle \llbracket U_n \rrbracket \rangle_{+} + k_n^{-}\langle \llbracket U_n \rrbracket \rangle_{-} \tag{A-46}$$

$$T_s = \frac{\partial \psi}{\partial \llbracket U_s \rrbracket} = (1-D_c)k_s \llbracket U_s \rrbracket \tag{A-47}$$

The corresponding damage driving force is derived as:

$$Y_m = -\frac{\partial \psi}{\partial D_c} = \frac{1}{2}k_n^{+}\langle \llbracket U_n \rrbracket \rangle_{+}^{2} + \frac{1}{2}k_s \llbracket U_s \rrbracket^2 \tag{A-48}$$

A cyclic damage evolution law is further required and specified by $\dot{D}_c = \dot{D}_c(D_c, Y_m, \|\dot{U}\|)$ as follows:

$$\dot{D}_c = A(1 - D_c)^m \langle \sqrt{Y_m} - \sqrt{Y_{m0}} \rangle^n \|\dot{U}\| \tag{A-49}$$

$$\|U\| = \left[\left(\frac{[\![U_n]\!]}{\delta_c} \right)^2 + \boldsymbol{\alpha}^2 \left(\frac{[\![U_s]\!]}{\delta_c} \right)^2 \right]^{1/2} \tag{A-50}$$

where A, m and n are parameters which control the rate of damage evolution. The damage propagates only if $Y_m \geq Y_{m0}$ and $\dot{Y_m} \geq 0$,[54].

Using equations (A-47) and (A-48), the damage evolution law can be rewritten as:

$$\dot{D}_c = A^*(1 - D_c)^m \langle \frac{\|T\|}{1 - D_c} - T_0 \rangle^n \|\dot{U}\| \tag{A-51}$$

where $A^* = A(\frac{\delta_c}{2k_n})^{n/2}$, $\|T\| = \sqrt{\langle T_n \rangle^2 + \frac{1}{\alpha} {T_s}^2}$, and T_0 is a traction threshold or fatigue endurance limit under which the cyclic damage variable does not evolve [54].

References

[1] Messler R.W., “Joining of Materials and Structures,” Elsevier, USA, 2004.

[2] Ahari H., “Optimization of laminated dies manufacturing,” Ph.D. Thesis, University of Waterloo, 2011, Canada.

[3] Gan Y.X., Aglan H.A., Steward R.V., Chin B.A., Grossbeck M.L., “Microstructure-fracture toughness relationship of vanadium alloy/stainless steel brazed joints,” Journal of Nuclear Materials 299, 2001, pp. 157–164.

[4] ABAQUS/CAE, Version 6.7-1, Dassault Systemes, 2007.

[5] Schwartz M., “Brazing,” ASM International, USA, 2003.

[6] Chen S., Chin B.A., “Low activation braze joint of dispersion-strengthened copper,” Journal of Nuclear Materials 225, 1995, pp. 132–136.

[7] Nayeb-Hashemi H., Lockwood M., “The effect of processing variables on the microstructures and properties of aluminum brazed joints,” Journal of Materials Science 37, 2002, pp. 3705–3713.

[8] Nishi H., Kikuchi K., “Influence of Brazing Conditions on the Strength of Brazed Joints of Alumina Dispersion-Strengthened Copper to 316 Stainless Steel,” Journal of Nuclear Materials 258-263, 1998, pp. 281–288.

[9] Nowacki J., Kawiak M., “Deformability of WC–Co sinters and 17-4 PH steel brazed joints,” Journal of Materials Processing Technology 157–158, 2004, pp. 584–589.

[10] Dixon D. G., “Ceramic matrix composite-metal brazed joints,” Journal of Materials Science 30, 1995, pp. 1539–1544.

[11] Michler T., Naumann J., Leistner W., “Evaluation of braze materials used for automotive liquid hydrogen tanks with special respect to hydrogen embrittlement and low temperature toughness,” Mat.-wiss. u. Werkstofftech.38, No. 1, 2007, pp. 43–50.

[12] Ghovanlou M. K., Jahed H., Khajepour A., “Mechanical reliability characterization of low carbon steel brazed joints with copper filler metal,” Journal of Materials Science and Engineering A 528, Issue 15–20, 2011, pp. 6146–6156.

[13] Leinenbach C., Schindler H.J., Baser T.A., Rüttimann N., Wegener K., “Quasistatic fracture behaviour and defect assessment of brazed soft

martensitic stainless steel joints," Engineering Failure Analysis 17, Issue 3, 2010, pp. 672–682.

[14] Zhang J., Jin L.Y., "Numerical simulation of residual stress in brazing joint between cemented carbide and steel," Journal of Materials Science and Technology 21, No. 12, 2005, pp. 1455–1459.

[15] Nied H. A., Schlanskier C.A., "The Thermostructural Analysis of Electric Contacts Using a Finite Element Model," IEEE Transactions on Components, Hybrid, and Manufacturing Technology 7, N. 1, 1984, pp. 112–124.

[16] Vaidyaa R.U., Rangaswamya P., Bourkea M.A.M., Butta D.P., "Measurement of bulk residual stresses in molybdenum disilicide/stainless steel joints using neutron scattering," Acta Materialia 46, Issue 6, 23, 1998, pp. 2047–2061.

[17] Travessa D. N., Ferrante M., Ouden G., "Finite element method simulation of residual stresses in Al2O3–AISI 304 steel joints," Materials Science and Technology 16, 2000, pp. 687–691.

[18] Zhang J. X., Chandel R. S., Chen Y. Z., Seow H. P., "Effect of residual stress on the strength of an alumina–steel joint by partial transient liquid phase

(PTLP) brazing," Journal of Materials Processing Technology 122, Issues 2-3, 2002, pp. 220–225.

[19] Jiang W., Gong J., Tu S., Fan Q., "A comparison of brazed residual stress in plate fin structure made of different stainless steel," Materials & Design 30, Issue 1, 2009, pp. 23–27.

[20] Saxton, H.J., West A.J., Barrett C.R., "Deformation and Failure of Brazed Joints- Macroscopic considerations," Metallurgical Transactions 2, 1971, pp. 999–1007.

[21] Flom Y., Wang L., "Flaw Tolerance in Lap Shear Brazed Joints - Part 1," Journal of Welding Research, 2004, pp. 32–38S.

[22] Lee Y. L., Wehner T. J., Lu M. W., Morrissett T. W., Pakalnins E., "Ultimate Strength of Resistance Spot-welds Subjected to Combined Tension and Shear," Journal of Testing and Evaluation 26, 1998, pp. 213–219.

[23] Wung P., Walsh T., Ourchane A., Stewart W., Jie M., "Failure of Spot Welds under In-Plane Static Loading," Experimental Mechanics 41, 2001. pp. 100–106.

[24] Moorhead A. J., Becher P. F., "Adaptation of the DCB test for determining fracture toughness of brazed joints in ceramic materials," Journal of Materials Science 22, 1987, pp. 3297–3303.

[25] Fu L., Miyasita Y., Mutoh Y., "Fracture Toughness of Si3N4/S45C Joint with an Interface Crack," Journal of Materials Online 1, 2005.

[26] Kobayashi H., Arai Y., Nakamura H., Sato T., "Strength Evaluation of Ceramic-Metal Joints," Journal of Materials Science and Engineering A 143, 1991, pp. 91–102.

[27] Philips N.R., He M.Y., Evans A.G., "A wedge fracture toughness test for intermediate toughness materials: Application to brazed joints," Acta Materialia 56, 2008, pp. 4593–4600.

[28] Nyhus B., Polanco M.L., Orjasater O., "SENT Specimens an Alternative to SENB Specimens for Fracture Mechanics Testing of Pipelines," Proceedings of 22nd International Conference on Offshore Mechanics and Arctic Engineering, Cancun, Mexico, 2003.

[29] Yu Y. H., Lai M. O., "Effects of gap filler and brazing temperature on fracture and fatigue of wide-gap brazed joints," Journal of Materials Science 30, 1995, pp. 2101–2107.

[30] Gao F. and Qiana Y., "Micromechanical properties of heterogeneous aluminum-silicon brazed joint," Materials Letters 58, 2004, pp. 2861–2866.

[31] Solomon H. D., "A statistical analysis of brazed joint fatigue behaviour," Welding Research Supplement, 2001, pp. 148–156.

[32] Gan Y. X., Aglan H. A., Steward R. V., Chin B. A., "Fatigue failure mechanisms of vanadium alloy/stainless steel brazed joints," Journal of Materials Science Letters 20, 2001, pp. 1909–1911.

[33] Mukhopadhyay N.K., Ghsh Chowdhury S., Das G., "An investigation of the failure of low pressure stream turbine blades," Engineering Failure Analysis 5, No. 3, 1998, pp. 181–193.

[34] Waddell J.N., Ichim I., Lee H., and Fangtao L., "Fatigue failures of bar-attachment brazed joints for implant-supported over dentures," Engineering Fracture Mechanics 74, 2007, pp. 1148–1159.

[35] Brossa M., Franconi E., Guerreschi U., Pierazzi L., Poggi P., Rustia V., "Pre- and post-irradiation properties of brazed joints of AISI 316L stainless steel," Journal of Nuclear Materials 212–215, 1994, pp. 1574–1578.

[36] Leinenbach C., Schindler H.J., Baser T.A., Rüttimann N., Wegener K., "Fracture behaviour and defect assessment of brazed steel joints," 17th European conference on fracture, Brno, Czech Republic, 2008, pp. 2121–2128.

[37] Roe K.L., Siegmund T., "An irreversible cohesive zone model for interface fatigue crack growth simulation," Engineering Fracture Mechanics 70, 2003, pp. 209–232.

[38] Solomon H. D., "Fatigue of 60/40 solder," IEEE Transactions on Components, Hybrids, and Manufactured Technology CHMT-9, 1986, pp. 91–104.

[39] Solomon H. D., "Energy approach to the fatigue of 60/40 solder: Part I-Influence of temperature and cycle frequency," Journal of Electronic Packaging 117, 1995, pp. 130–135.

[40] Solomon H. D., "Energy approach to the fatigue of 60/40 solder: Part II-Influence of hold time and asymmetric loading," Journal of Electronic Packaging 118, 1996, pp. 67–70.

[41] Solomon H. D., "Predictions of solder joint fatigue life," IEEE, Electronic Components and Technology Conference Proceedings. 40th, 1990.

[42] Zhang X., Ricky Lee S.W., Pao Y.H, "A damage evolution model for thermal fatigue analysis of solder joints," Journal of Electronic Packaging 122, 2000, pp. 200–206.

[43] Zhao X. J., Zhang G. Q., Caers J. F. J. M., "Solders fatigue prediction using interfacial boundary volume criterion," Journal of Electronic Packaging 125, 2003, pp. 582–588.

[44] Kim D.G., Kim J.W., Jung S.B., "Evaluation of solder joint reliability in flip chip package under thermal shock test," Proceedings of The International Conference on Materials for Advanced Technologies (ICMAT), 2005.

[45] Lau K.J., Tang C.Y., Tse P.C., "Microscopic experimental investigation on shear failure of solder joints," International Journal of Fracture 130, 2004, pp. 617–634.

[46] Solomon H.D., "Low cycle fatigue of surface mounted chip carrier/printed wiring board joints," IEEE, Electronic Component Conference Proceedings. 39th, 1989.

[47] Shim D.J., Spearing S.M., Yang Q., "Crack initiation and growth in solder joints under cyclic shear deformation using piezomechanical actuation," Journal of Engineering Materials and Technology 129, 2007, pp. 19–28.

[48] Yang Q.D., Shim D.J., Spearing S.M., “A cohesive zone model for low cycle fatigue life prediction of solder joints,” Microelectronic Engineering 75, 2004, pp. 85–95.

[49] Abdul-Baqi A., Schreurs P.J.G., Geers M.G.D., “Fatigue damage modeling in solder interconnects using a cohesive zone approach,” International Journal of Solids and Structures 42, 2005, pp. 927–942.

[50] Chaboche J.L., Feyel F., Monerie Y., Interface debonding models: a viscous regularization with a limited rate dependency, International Journal of Solids and Structures 38, 2001, pp. 3127–3160.

[51] Dugdale, D. S., ‘‘Yielding of Steel Sheets Containing Slits,’’ Journal of The Mechanics and Physics of Solids 8, 1960, pp. 100–104.

[52] Barenblatt, G. I., ‘‘Mathematical Theory of Equilibrium Cracks,’’ Advances in Applied Mechanics, Academic Press, New York, 1962, pp. 55–125.

[53] Shet C., Chandra N., “Analysis of Energy Balance When Using Cohesive Zone Model to Simulate Fracture Processes,” Transactions of the ASME 124, 2002, pp. 440–450.

[54] Bouvard J.L., Chaboche J.L., Feyel F., Gallerneau F., "A cohesive zone model for fatigue and creep–fatigue crack growth in single crystal super alloys," International Journal of Fatigue 31, 2009, pp. 868–879.

[55] Needleman, A., "A continuum model for void nucleation by inclusion debonding," Journal of Applied Mechanics 54, 1987, pp. 525–531.

[56] Högberg J. L., "Mixed mode cohesive law," International Journal of Fracture 141, 2006, pp. 549–559.

[57] Needleman A., "An analysis of decohesion along an imperfect interface," International Journal of Fracture 42, 1990, pp. 21–40.

[58] Tvergaard, V., Hutchinson, J. W., "The relation between crack growth resistance and fracture process parameters in elastic-plastic solids," Journal of Mechanics and Physics of Solids 40, 1992, pp. 1377–1397.

[59] Schwalbe, K. H., Cornec, A., "Modeling crack growth using local process zones," Technical report, GKSS Research Centre, Geesthacht, 1994.

[60] Chandra N., "Evaluation of interfacial fracture toughness using cohesive zone model," Journal of Composites 33, Part A, 2002, pp. 1433–1447.

[61] Fan C., Ben Jar P.Y., Cheng J.J.R., “Cohesive zone with continuum damage properties for simulation of delamination development in fiber composites and failure of adhesive joints,” Engineering Fracture Mechanics 75, 2008, pp.3866–3880.

[62] de Moura M.F.S.F., Chousal J.A.G., “Cohesive and continuum damage models applied to fracture characterization of bonded joints,” International Journal of Mechanical Sciences 48, 2006, pp. 493–503.

[63] Mi Y., Crisfield M.A., Davies G.A.O., “Progressive delamination using interface elements,” Journal of composite materials 32, No. 14, 1998, pp. 1246–1272.

[64] Tvergaard V., Hutchinson J.W., “On the toughness of ductile adhesive joints,” Journal of Mechanics and Physics of Solids 44, 1996, pp. 789–800.

[65] Tvergaard V., Hutchinson J.W., “Toughness of an interface along a thin ductile layer joining elastic solids,” Philosophical Magazine A70, 1994, pp. 641–656.

[66] Yang Q.D., Thouless M.D., Ward S.M., “Elastic-plastic mode II of adhesive joints,” International Journal of Solids and Structures 38, 2001, pp. 3251–3262.

[67] Zou Z., Reid S.R., Li S., “A continuum damage model for delaminations in laminated composites,” Journal of the Mechanics and Physics of Solids 51, 2003, pp. 333–356.

[68] Yang Q., Cox B., “Cohesive models for damage evolution in laminated composites,” International Journal of Fracture 133, 2005, pp. 107–137.

[69] Meo M., Thieulot E., “Delamination modeling in a double cantilever beam,” Composite Structures 71, 2005, pp. 429–434.

[70] Xie D., Salvi A. G., Sun C., Waas A. M., “Discrete Cohesive Zone Model to Simulate Static Fracture in 2D Triaxially Braided Carbon Fiber Composites,” Journal of Composite Materials 40, No. 22, 2006, pp. 2025–2046.

[71] Blackman B.R.K., Hadavinia H., Kinloch A.J., Williams J.G., “The use of a cohesive zone model to study the fracture of fiber composites and adhesively-bonded joints,” International Journal of Fracture 119, 2003, pp. 25–46.

[72] Han T.S., Ural A., Chen C.S., Zehnder A.T., Ingraffea A.R., Billington S.L., “Delamination buckling and propagation analysis of honeycomb panels using a cohesive element approach,” International Journal of Fracture 115, 2002, pp. 101–123.

[73] van den Bosch M.J., Schreurs P.J.G., Geers M.G.D., "A cohesive zone model with a large displacement formulation accounting for interfacial fibrillation," European Journal of Mechanics A/Solids 26, 2007, pp. 1–19.

[74] Mohammed I., Liechti K.M., "Cohesive zone modeling of crack nucleation at bimaterial corners," Journal of the Mechanics and Physics of Solids 48, 2000, pp. 735-764.

[75] Liljedahl C. D. M., Crocombe A. D., Wahab M. A., Ashcroft I. A., "Damage modeling of adhesively bonded joints," International Journal of Fracture 141, 2006, pp. 147–161.

[76] Xie D., Waas A.M., "Discrete cohesive zone model for mixed-mode fracture using finite element analysis," Engineering Fracture Mechanics 73, 2006, pp. 1783–1796.

[77] Salomonsson K., Andersson T., "Modeling and parameter calibration of an adhesive layer at the meso level," Mechanics of Materials 40, 2008, pp. 48–65.

[78] Alfano M., Furgiuele F., Leonardi A., Maletta C., Paulino G.H., "Mode I fracture of adhesive joints using tailored cohesive zone models," International Journal of Fracture 157, 2009, pp. 193–204.

[79] Valoroso N., Champaney L., “A damage-mechanics-based approach for modeling decohesion in adhesively bonded assemblies,” Engineering Fracture Mechanics 73, 2006, pp. 2774–2801.

[80] Yang B., Mall S., Ravi-Chander K., “A cohesive zone model for fatigue crack growth in quasibrittle materials,” International Journal of Solids and Structures 38, 2001, pp. 3927–3944.

[81] de-Andres A., Perez J. L., Ortiz M., “Elastoplastic finite element analysis of three-dimensional fatigue crack growth in aluminum shafts subjected to axial loading,” International Journal of Solids and Structures 36, 1999, pp. 2231–2258.

[82] Nguyen O., Repetto E.A., Ortiz M., Radovitzky R.A., “A cohesive model of fatigue crack growth,” International Journal of Fracture 110, 2001, pp. 351–369.

[83] Wang B., Siegmund T., “A numerical analysis of constraint effects in fatigue crack growth by use of an irreversible cohesive zone model,” International Journal of Fracture 132, 2005, pp. 175–196.

[84] Khoramishad H., Crocombe A.D., Katnam K.B., Ashcroft I.A., "Predicting fatigue damage in adhesively bonded joints using a cohesive zone model," International Journal of Fatigue 32, 2010, pp. 1146–1158.

[85] Chandra N., Li H., Shet C., Ghonem H., International Journal of Solids and Structure 39, 2002, pp. 2827–2855.

[86] Que N.S., Tin–Loi F., "Numerical evaluation of cohesive fracture parameters from a wedge splitting test," Engineering Fracture Mechanics 69, 2002, pp. 1269–1286.

[87] Sørensen B. F., Jacobsen T. K., "Determination of cohesive laws by the J-integral approach," Engineering Fracture Mechanics 70, 2003, pp. 1841–1858.

[88] Chen C. R., Kolednik O., Scheider I., Siegmund T., "On the determination of the cohesive zone parameters for the modeling of micro-ductile crack growth in thick specimens," International Journal of Fracture 120, 2003, pp. 517–536.

[89] Standard Specification for Carbon Structural Steel, Designation: A36/A36M-08, ASTM International, 2008.

[90] Standard Practice for Strain-Controlled Axial-Torsional Fatigue Testing with Thin-Walled Tubular Specimens, Designation: E2207–08, ASTM International, 2008.

[91] Chang C.T., Shiue R.K., "Infrared brazing Ti–6Al–4V and Mo using the Ti–15Cu–15Ni braze alloy," International Journal of Refractory Metals & Hard Materials 23, 2005, pp. 161–170.

[92] Bressan, J. D., Unfer, R. K., "Construction and Validation Tests of a Torsion Test Machine," Journal of Materials Processing Technology 179, 2006, pp. 23–29.

[93] Standard Test Method for Measurement of Fracture Toughness, Designation: E1820–08a, ASTM International, 2008.

[94] Spink G. M., Worthington P. J., Heald P. T., "The Effect of Notch Acuity on Fracture Toughness Testing," Materials Science and Engineering 11, 1973, pp. 113–117.

[95] Anderson T.L., "Fracture Mechanics: Fundamentals and Applications," 3rd edition, Taylor and Francis, USA, 2005.

[96] Judy R.W., Goode R.J., "Fracture Extension Resistance (R-Curve) Characteristics for Three High Strength Steel," Fracture Toughness Evaluation by R-Curve Methods, ASTM, STP 527, 1973, pp. 48–61.

[97] ASM Handbook, Fractography, V. 12, 2010.

[98] Jiang L.M., Zhou Y.C., Liao Y.G., Sun C.Q., "A pressurized blister test model for the interface adhesion of dissimilar elastic–plastic materials," Materials Science and Engineering A 487, 2008, pp. 228–234.

[99] Thouless M. D., Adams J. L., Kafkalidis M. S., Ward S. M., Dickie R. A., Westerbeek G. L., "Determining the toughness of plastically deforming joints," Journal of Materials Science 33, 1998, pp. 189–197.

[100] Flores K. M., Dauskardt R. H., "Enhanced Toughness Due to Stable Crack Tip Damage Zones in Bulk Metallic Glass," Scripta Materialia 41, 1999, p. 937.

[101] Mirone G., "Role of stress triaxiality in elastoplastic characterization and ductile failure prediction," Engineering Fracture Mechanics 74, 2007, pp. 1203–1221.

[102] O'Dowd N.P., Shih C.F., "Family of Crack Tip Fields Characterized by a Triaxiality Parameter-I. Structure of Fields," Journal of the Mechanics and Physics of Solids 39, No.8, 1991, pp. 989–1015.

[103] Solomon H.D., Halford G.R., Kaisand L.R., Leis B. N., Low Cycle Fatigue, ASTM International, STP 942, 1988.

[104] McClung R.C., Sehitoglu H., "On the finite element analysis of fatigue crack closure-1. Basic modeling issues," Engineering Fracture Mechanics 33, No.2, 1989, pp. 237–252.

[105] Lemaitre, J., "A course on damage mechanics," 2nd edition, Springer, 1996.